Numerical studies of turbulent Rayleigh-Bénard magnetoconvection in rectangular enclosures

Dissertation

zur Erlangung des akademischen Grades

Doktoringenieur

(Dr.-Ing.)

vorgelegt der

Fakultät für Maschinenbau der

Technischen Universität Ilmenau

von Frau

M. Sc. Wenjun Liu

geboren am 30.10.1989 in Shandong, China

1. Gutachter: apl. Prof. Dr.-Ing. habil. Christian Karcher
2. Gutachter: Univ.-Prof. Dr. rer. nat. habil. Jörg Schumacher
3. Gutachter: apl. Prof. Dr.-Ing. Leo Bühler

Tag der Einreichung: 06.11.2018
Tag der wissenschaftlichen Aussprache: 27.02.2019

urn:nbn:de:gbv:ilm1-2019000011

Abstract

Three-dimensional turbulent magnetoconvection in liquid metal at a Prandtl number of $Pr = 0.025$ is studied in closed rectangular cells for strong external magnetic fields B_0 by means of direct numerical simulations which apply the quasistatic approximation. The main aim is to understand how the turbulent heat and momentum transfer is affected and how the convection structures are organized by the external magnetic fields. Two representative systems are investigated in this thesis: turbulent Rayleigh-Bénard convection in an external horizontal magnetic field and in an external vertical magnetic field.

For the system with an external horizontal magnetic field, turbulent Rayleigh-Bénard convection at a Rayleigh number of $Ra = 10^6$ in closed cells with two different geometries, that of a square box with an aspect ratio of $\Gamma = 4 : 4 : 1$ and a long rectangular box with $\Gamma = 1 : 4 : 1$ are studied. Different convection pattern regimes that are related to the aspect ratio and the strength of the magnetic field, which is quantified by the Hartmann number Ha, are identified. The most remarkable convection pattern observed in the square box are reversals of the large-scale flow – a reorganization process of the roll-like structure that fill the whole cell constrained by a moderate magnetic field. The key regime of the flow reversals is the interaction of between the aligned convection rolls and global horizontal circulation caused by the skewed-varicose instability. This regime bears an interesting similarity to the large-scale intermittency in the channel flow with moderate spanwise magnetic field. The most interesting convection regime in the long rectangular box with $\Gamma = 1 : 4 : 1$ is the twisted roll structure which consists of two half-vessel-length rolls with different orientations during the transition period under a moderate magnetic field.

For the system with an external vertical magnetic field, turbulent Rayleigh-Bénard convection at a Rayleigh number of $Ra = 10^6$ in a closed cubic cell with an aspect ratio of $\Gamma = 1 : 1 : 1$ and at a higher Rayleigh number of $Ra = 10^7$ in a square box with an aspect ratio of $\Gamma = 4 : 4 : 1$ are mainly reported in this thesis. The most prominent results come from the latter configuration. By a Fourier analysis, the convection patterns are shown with a decreasing characteristic horizontal wavelength as Ha increases. The turbulent heat transfer, which is investigated in concentric square shells, is found to become increasingly distributed on flow modes that are attached to the side walls. Similar to rotating Rayleigh-Bénard convection, the sidewall modes continue to exist for Ha beyond the Chandrasekhar limit of linear stability. We report a detailed analysis of the complex two-layer structure of these wall modes, their extension into the cell interior, and a resulting sidewall boundary layer composition that is found to scale with the Shercliff layer thickness.

Zusammenfassung

Dreidimensionale turbulente Magnetokonvektion in Flüssigmetallen bei einer Prandtl-Zahl von $Pr = 0{,}025$ wird in geschlossenen rechteckigen Zellen für starke äußere Magnetfelder B_0 durch direkte numerische Simulationen untersucht, welche die quasistatische Näherung anwenden. Das Hauptziel ist es, zu verstehen wie der turbulente Wärme- und Impulstransport beeinflusst wird und wie die Konvektionsstrukturen durch die äußeren Magnetfelder umorganisiert werden. In dieser Arbeit werden zwei repräsentative Systeme untersucht, bei denen die turbulente Rayleigh-Bénard-Konvektion in einem äußeren horizontalen Magnetfeld bzw. in einem externen vertikalen Magnetfeld erfolgt.

Für das System mit einem horizontalen Magnetfeld wird Rayleigh-Bénard-Konvektion bei einer Rayleigh-Zahl von $Ra = 10^6$ in geschlossenen Zellen mit zwei unterschiedlichen Geometrien untersucht, d. h. eine Zelle mit quadratischer Grundfläche mit einem Seitenverhältnis von $\Gamma = 4:4:1$ und eine lange rechteckige Zelle mit $\Gamma = 1:4:1$. Unterschiedliche Konvektionsregimes werden identifiziert, welche vom Aspektverhältnis und der Stärke des Magnetfelds abhängen, das durch die Hartmann-Zahl Ha quantifiziert wird. Das bemerkenswerteste Konvektionsregime, das in der Box mit quadratischer Grundfläche beobachtet wird, ist die Umkehrung der Strömung – ein Reorganisationsprozess der rollenartigen Struktur, die durch ein gemäßigtes Magnetfeld eingeschränkt wird. Das Schlüssel zu den Strömungsumkehrungen liegt in der Wechselwirkung zwischen den ausgerichteten Konvektionswalzen und der globalen horizontalen Zirkulation, die durch die so genannte Skewed-Varicose-Instabilität verursacht wird. Das Regime zeigt eine interessante Ähnlichkeit mit der großskaligen Intermittenz in einer Kanalströmung mit einem moderaten äußeren Magnetfeld in Spannweitenrichtung. Das interessanteste Konvektionsregime in der langen rechteckigen Zelle ist die verdrillte Walzenstruktur, die aus zwei Walzen mit halber Behälterlänge mit unterschiedlichen Ausrichtungen während der Übergangsperiode besteht.

Für das System mit äußerem vertikalen Magnetfeld wird hauptsächlich turbulente Rayleigh-Bénard-Konvektion bei einer Rayleigh-Zahl von $Ra = 10^6$ in einer geschlossenen kubischen Zelle mit einem Aspektverhältnis von $\Gamma = 1:1:1$ und bei einer hohen Rayleigh-Zahl von $Ra = 10^7$ in einer Zelle mit einem Seitenverhältnis von $\Gamma = 4:4:1$ beschrieben. Durch eine Fourier-Analyse werden Konvektionsstrukturen mit abnehmender charakteristischer horizontaler Wellenlänge gefunden während Ha zunimmt. Der turbulente Wärmetransport, welcher in konzentrischen quadratischen Teilbereichen untersucht wird, verteilt sich zunehmend auf Strömungsstrukturen, die an den Seitenwänd anliegen. Ähnlich wie bei rotierender Rayleigh-Bénard-Konvektion bestehen die Seitenwandmoden für Ha oberhalb der Chandrasekhar-Grenze fort. Es

erfolgt, eine detaillierte Analyse der komplexen Zweischicht-Struktur dieser Seitenwandmoden, ihrer Ausdehnung in das Zellinnere und der daraus resultierenden Zusammensetzung der Seitenwandgrenzschicht, deren Skalierung mit der Shercliff-Schichtdicke erfolgen kann.

Contents

Chapter 1

Introduction

1.1 Background and motivation

We discuss the interaction between convection and magnetic field in well electrically conducting fluids. The main aim is to advance our understanding of heat and momentum transfer in such flows, which are referred to as *magnetoconvection*, equivalent with *magneto convection* and *magnetic convection*.

Magnetoconvection is of interest in numerous astro- and geophysical problems [Rüdiger *et al.*, 2013; Weiss & Proctor, 2014], such as the formation of sunspots (see figure 1.1), solar granulation and magnetic field generation of planets like the Earth. Less spectacular, but not less important, are the occurrences of magnetoconvection in numerous technological applications [Davidson, 2016] ranging from metallurgy and materials processing, where the control of the convective flow by a magnetic field may improve the quality of the produced material, via liquid metal battery with its performance influenced by magnetoconvective instabilities, to liquid metal blanket design in nuclear fusion technology (see figure 1.2), where the liquid metal within the blanket is exposed to strong temperature gradients as well as strong magnetic fields. Therefore, the knowledge of turbulent magnetoconvection in a strong magnetic field becomes fundamental to the design of these cooling and breeding devices.

Particularly, in most technological applications, the working fluids are liquid molten metals with very small magnetic Prandtl number P_m , which is a ratio of the viscous and magnetic diffusion, of the order 10^{-5}. The magnetic Reynolds number R_m, which is a measure of the relative magnitude of advection to diffusion of the magnetic field in the flow, thus remains small, i.e., of the order 10^{-2} to 10^{-4}. In these cases, the induced secondary magnetic field is negligible, and therefore, the *quasistatic* regime of magnetohydrodynamics [Davidson, 2016; Knaepen & Moreau, 2008] is applicable for a simplification of the full set of magnetoconvection equations.

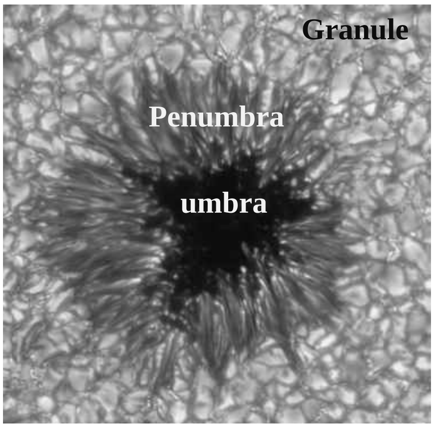

Figure 1.1: High-resolution G-band image of a symmetrical sunspot, obtained with the Swedish Solar Telescope (SST) on La Palma. The magnetic field is vertical at the center of the spot but becomes increasingly inclined towards the periphery. In the central dark umbra there is a tesseral pattern of convection, with isolated bright dots, a few of which are visible. The penumbra has a filamentary structure, with roll-like patterns of convection. The small-scale cellular pattern surrounding the spot is the photospheric granulation. Hot plasma rises in the center of a granule and cooler fluid sinks around its periphery. The bright points nestling between granules indicate the presence of small-scale magnetic fields. (Courtesy of L. H. M. Rouppe van der Voort and the Royal Swedish Academy of Sciences.)

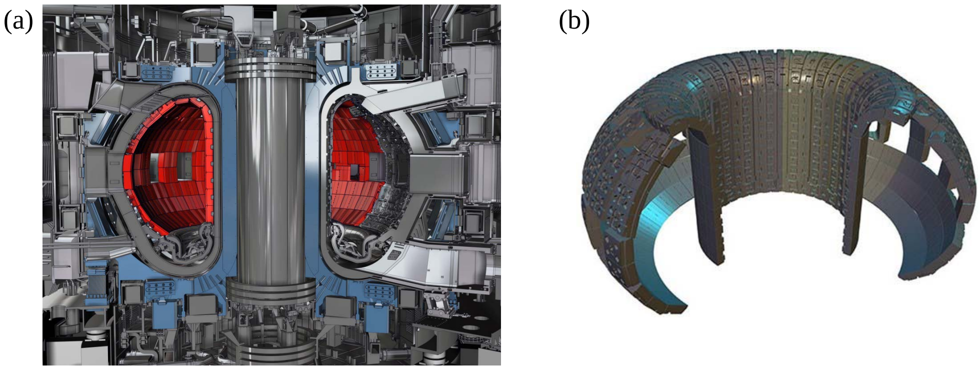

Figure 1.2: (a) Principle structure of the Tokamak nuclear fusion reactor in ITER (www.iter.org). (b) Principle scheme of a cooling and breeding blanket corresponding to the red region in panel (a). The blanket is positioned between the plasma and the magnetic coils and has three main functions: (i) shielding or protecting the surroundings from the huge thermal load and neutrons generated in the reaction zone, (ii) converting the energy of the neutrons into heat and transporting the heat into an external power generation cycle, and (iii) applying the reaction between the neutrons and lithium in the blankets to breed tritium fuel.

This work is dedicated to the magnetoconvection in those industrial applications with negligible magnetic Reynolds number $R_m \ll 1$. Although extensive experimental and numerical studies have been performed to analyze convection in liquid metal in presence of an external magnetic field, only a few are available in the case of strong magnetic field. And because of the limited observation capabilities in liquid metals and difficulties of reproducing relevant flow parameters, it is challenging to study the problem in experiments alone. Furthermore, the instabilities cannot be predicted by applied approximate models of flows in strong magnetic fields. This sets the motivation for the present work.

We conduct highly accurate three-dimensional direct numerical simulations to investigate magnetoconvection and focus on the case of strong magnetic fields. The most relevant applications are, therefore, the design of liquid metal blankets of fusion reactor and strong magnetic field controlled solidification. Rather than focus on specific applications, however, the present work will study the fundamental physics by employing an idealized system of Rayleigh-Bénard magnetoconvection. A detailed introduction and motivation will follow next.

1.2 Research objectives and review of selected research

Rayleigh-Bénard magnetoconvection, i.e. Rayleigh-Bénard convection under the effect of magnetic fields have been frequently invoked to study the primary physics of magnetoconvection because of its analytic and experimental accessibility (see, e.g., [Aurnou & Olson, 2001; Burr & Müller, 2001, 2002; Busse, 2008; Busse & Clever, 1982, 1983, 1989; Chandrasekhar, 1952, 1961; Cioni *et al.*, 2000; Clever & Busse, 1989; Fauve *et al.*, 1981, 1984*a*,*b*; Houchens *et al.*, 2002; Nakagawa, 1955, 1957; Tasaka *et al.*, 2016; Vogt *et al.*, 2018; Yanagisawa *et al.*, 2013, 2011, 2010*a*; Zürner *et al.*, 2016]).

The system itself is deceptively simple – an electrically conducting fluid confined in a horizontal layer heated from below, cooled from above, and subject to a magnetic field. The interplay of the occurring buoyancy and Lorentz forces inside, however, has yielded highly complex flows with very distinct flow structures and transport regimes of heat and momentum depending on the input parameters (which will be thoroughly defined in Chapter 2): the Prandtl number Pr, a ratio of the viscous diffusion coefficient (also known as kinematic viscosity) and the thermal diffusion coefficient, the Rayleigh number Ra, which is a measure of the buoyancy force and the Hartmann number Ha, a measure of the magnetic field, as well as the direction of the magnetic field in addition with aspect ratio Γ when a closed geometry is considered.

In this work we focus on two representative objectives: Rayleigh-Bénard convection under effects of a horizontal magnetic field and Rayleigh-Bénard convection under effects of a vertical magnetic field (see figure 1.3). A detailed review of former researches especially those are most related to this work will follow next.

We start with the effect of a horizontal magnetic field on Rayleigh-Bénard con-

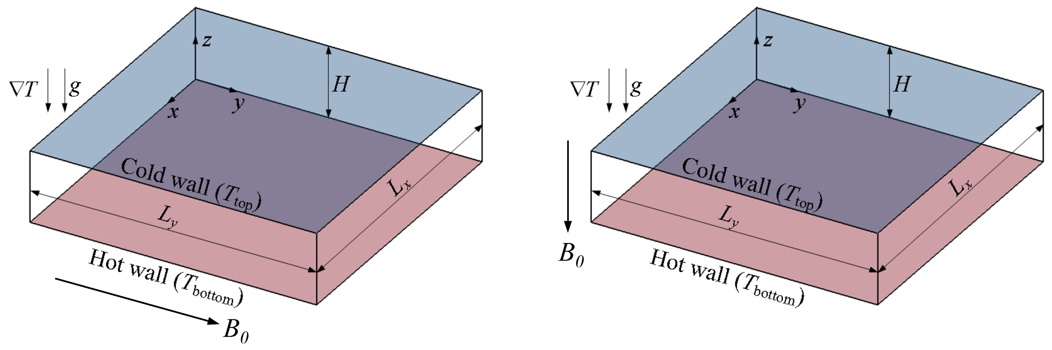

Figure 1.3: Configurations which are considered in this thesis. Left: Rayleigh-Bénard convection under effects of a horizontal magnetic field. Right: Rayleigh-Bénard convection under effects of a vertical magnetic field.

vection. Early works can be traced back to the theoretical studies in an infinitely extended horizontal layer heated from below by Chandrasekhar [1961] and by Busse & Clever [1983, 1989]. A purely horizontal magnetic field has no effect on the onset of convection [Chandrasekhar, 1961], but it delays the onset of oscillatory convection and therefore tends to increase the efficiency of convective heat transport [Busse & Clever, 1983, 1989]. In addition, the horizontal magnetic field tends to organize the convection pattern as a simpler structure in form of two-dimensional rolls aligned with the magnetic field, which has been demonstrated in numerous experiments (see, e.g., [Burr & Müller, 2002; Fauve *et al.*, 1981, 1984*a*,*b*; Tasaka *et al.*, 2016; Vogt *et al.*, 2018; Yanagisawa *et al.*, 2013, 2011, 2010*a*]). Moreover, Burr & Müller [2002] reported that in realistic cases with bounded fluid layers, the horizontal magnetic field also tends to increase the convection threshold because of the Hartmann braking at the side walls perpendicular to the magnetic field lines. The wave number of the two-dimensional rolls increases with increasing magnetic field strength. Particularly, with the development of ultrasonic velocity measurement, statistical spatio-temporal convection patterns in a liquid metal under horizontal magnetic fields have been studied experimentally and various flow regimes and regime transitions have been uncovered [Tasaka *et al.*, 2016; Vogt *et al.*, 2018; Yanagisawa *et al.*, 2013, 2011, 2010*a*]. One of the most interesting results are the flow reversals observed in a square vessel of aspect ratio 5 under an intermittent horizontal magnetic field, which is also the most interesting point of the present study on Rayleigh-Bénard convection under the effect of a horizontal magnetic field.

Now we move on to review the effect of a vertical magnetic field on Rayleigh-Bénard convection. Chandrasekhar [1952, 1961] first analyzed the linear problem and showed that a sufficiently strong vertical external magnetic field can suppress the onset of Rayleigh-Bénard convection. For example, for the case of free-slip boundaries at the top and bottom plates, the critical Rayleigh number Ra_c of the onset of magnetoconvection in a layer, that is heated from below and cooled from above, is given in analytical form by

$$Ra_\mathrm{c} = \frac{\pi^2 + a^2}{a^2}\left[(\pi^2 + a^2)^2 + \pi^2 Q\right] \longrightarrow \pi^2 Ha^2 \quad \text{for} \quad \frac{1}{\pi^2} Ha^2 \gg 1\,. \tag{1.1}$$

Here, $a = kH$ is the dimensionless horizontal normal mode wave number, H the height of the convection layer and Q the Chandrasekhar number, which is the square of Hartmann number Ha. The equation (1.1) is known as the *Chandrasekhar linear stability limit* of magnetoconvection and the relation holds also for no-slip boundary conditions at the top and bottom. Experiments involving a layer of mercury by Nakagawa [1955, 1957] yielded consistent results with the linear prediction. Busse & Clever [1982] discussed the oscillatory stability of convection roll in the presence of a vertical magnetic field theoretically and reported that the vertical magnetic field tends again to delay the onset of oscillatory convection and also tends to increase the efficiency of convective heat transport, since the onset of oscillations reduces the heat transport by convection [Clever & Busse, 1989]. The results were later confirmed in laboratory experiments [Aurnou & Olson, 2001; Burr & Müller, 2001; Cioni *et al.*, 2000] and further phenomena for highly supercritial conditions, which is most relevant for technical applications, were also reported. In particular, Burr & Müller [2001] investigated the local temporal dynamics of liquid metal Rayleigh-Bénard convection in a long rectangular box under a vertical magnetic field based on local temperature measurements. It is observed that the fluctuations in the temperature field get damped significantly by the vertical magnetic field and that the effect is selective with respect to frequency. Also, and the fluctuating part of the local temperature gradient confirms that the convective flow under the vertical magnetic field remains horizontally isotropic and no predominant orientation of time-dependent flow structures is established. Cioni *et al.* [2000] investigated the effect of a vertical magnetic field on turbulent Rayleigh-Bénard convection experimentally with the Rayleigh number Ra up to 3×10^9 and the Chandrasekhar number Q up to 4×10^6 and characterized two convective regimes influenced by vertical magnetic fields, namely regime I, $Nu \sim Ra/Q$ for large Q and regime II, $Nu \sim Ra^{0.43} Q^{-0.25}$ for higher Ra. Here, the Nusselt number Nu is a dimensionless measure of the turbulent heat transfer. The different regimes were supposed to be associated with the different convection pattern in the interior. However, due to the opaque nature of liquid metal, which are commonly used in magnetoconvection experiments, detailed experimental understanding of the interior convection pattern under effect of a vertical magnetic field is very few. This sets a first central motivation of the present study.

Furthermore, an equation similar to (1.1) can be derived for a Rayleigh-Bénard convection layer that rotates about the vertical axis with a constant angular velocity Ω_0 – an alternative way to suppress the onset of convection (With the dimensionless Taylor number given by $Ta = 4\Omega_0^2 H^4/\nu^2$, equation (1.1) for rotating convection follows by the substitution $(\pi^2 + a^2)Ha^2 = Ta$). It is well-known since the experiments in water or oil of Zhong *et al.* [1991], Ecke *et al.* [1992], Liu & Ecke [1999], and King *et al.* [2012] and the linear stability analyses of Goldstein *et al.* [1993, 1994] that the existence of sidewalls in closed and rotating cylindrical cells can destabilize convection. For recent direct numerical simulations of rotating liquid metal convection flows, we refer additionally to Horn & Schmid [2017]. In other words, convection is present for $Ra < Ra_\mathrm{c}$ in form of subcritical modes attached to the sidewalls which are denoted as *wall modes* in the following. This result together with the close analogy to rotating Rayleigh-Bénard convection sets a second central motivation for the present study on Rayleigh-Bénard convection under the effect of a vertical magnetic field.

We now move on to define the scope of the present thesis more precisely and formulate the questions that it intends to answer.

1.3 Scope of the thesis

The aim of the present work is to study turbulent Rayleigh-Bénard magnetoconvection via high-resolution direct numerical simulation (DNS) with an in-house FORTRAN code. As mentioned in the previous section, two main points are discussed in this thesis, turbulent Rayleigh-Bénard convection under effects of a horizontal magnetic field and turbulent Rayleigh-Bénard convection under effects of a vertical magnetic field. In both objectives, we will consider a configuration that is typical for laboratory experiments in the field, a closed rectangular cell filled with liquid gallium at a Prandtl number $Pr = 0.025$.

For the subject of turbulent Rayleigh-Bénard convection in presence of a horizontal magnetic field, the work aims to answer the following general questions:

1. How are the convection structures in a closed geometry organized by a horizontal magnetic field? And how is the turbulent heat and momentum transport affected?

2. Will flow reversals be observed in configurations with different aspect ratios? If so, how does the reversal regime compare to the former experiments by Yanagisawa *et al.* [2013] and Tasaka *et al.* [2016]. How do heat and momentum transfer, turbulent kinetic energy and dissipation rates evolve when the reversals proceed?

For the subject of turbulent Rayleigh-Bénard convection in presence of a vertical magnetic field, the work aims to answer the following general questions:

1. How is the turbulent heat and momentum transfer is affected and how are the structures reorganized when the vertical magnetic field strength is increased stepwise to values toward the Chandrasekhar linear stability limit (Eq. 1.1)?
2. Will the magnetoconvection survive when the vertical magnetic field strength increase beyond the Chandrasekhar linear threshold in a closed geometry? How is the structure organized and how does it compare to the subcritical wallmodes in rotating Rayleigh-Bénard convection?

The thesis is structured as follows. In the next chapter, we describe the theoretical foundations related to Rayleigh-Bénard magnetoconvection and introduce the physical models and the governing equations used in the study. The numerical procedure is presented in chapter 3. The basic scheme of the solver, the boundary condition treatment and the clustering schemes are introduced in detail. Studies of grid sensitivity and a verification of the numerical procedure are also presented. Chapter 4 is devoted to the investigation of turbulent Rayleigh-Bénard convection under effects of a horizontal magnetic field and the results of effects of a vertical magnetic field are included in chapter 5. Finally, in chapter 6, the conclusions arising out of the present work are summarized with a brief outlook towards future work.

Chapter 2

Theoretical foundations

2.1 Boussinesq equations

Rayleigh-Bénard convection is the simplest setting of a buoyancy driven flow, which considers a horizontal layer of fluid heated from below and cooled from above. When the temperature difference across the layers is large enough, the destabilizing buoyancy effects exceed the stabilizing effects of viscosity and natural convection occurs. The transition from the static, diffusive state to a state of natural convection, which is called Rayleigh-Bénard instability, was first theoretically analyzed by Rayleigh (1916), who was inspired by the experiments of Bénard (1900). Rayleigh-Bénard convection plays a crucial role in the development of stability theory in hydrodynamics, in pattern formation and in the study of spatial-temporal chaos and has been considered as a paradigm to understand basic properties of thermal convection in numerous natural and technological systems, such as, thermal convection in the atmosphere, in the oceans, in nuclear reactors, crystallization processes as well as in geo- and astrophysics, e.g., the generation of magnetic fields within the Earth's outer core. An detailed introduction and overview can be found in [Ahlers *et al.*, 2009; Chillà & Schumacher, 2012]. Here we mainly recall the governing equations of Rayleigh-Bénard convection. The basic equations of motion in convective turbulence take a full set of compressible flow equations containing the balances of mass, momentum and energy as well as a supplemented equation of state. They have been introduced in detail in the book of Chandrasekhar [1961]. However, in a wide range of applications, the exact equations can be simplified considerably based on the Boussinesq approximation (Boussinesq, 1903).

The main idea of the Boussinesq approximation is that the temperature variations about the reference state are small such that the density variations remain small as well. The buoyancy still drives the fluid motion. In these flows, the variations in density ρ

can be neglected and ρ can be treated constant which leads to the incompressibility approximation. This holds except for the volume force. One introduces a force density $\rho \boldsymbol{g}$, where $\boldsymbol{g}$ is the acceleration of gravity. In this buoyancy term, the density ρ depends linearly on the temperature perturbation and is given by

$$\rho = \rho_0[1 - \beta(T - T_0], \tag{2.1}$$

where ρ_0 is the density of fluid at reference temperature T_0, and β is the coefficient of volume expansion. For gases and liquids that people are mostly considered, the coefficient of volume expansion β is found in the range $10^{-3}/K$ to $10^{-4}/K$. Specifically, for liquid gallium that we are considered in this thesis, β is about $1.18 \times 10^{-4}/K$ [Hoather, 1936]. For a temperature variation of moderate amount, the variations in density $|\Delta\rho|/\rho_0 = |\rho - \rho_0|/\rho_0 = \beta|T - T_0|$ are much smaller than 1. Therefore, it can be ignored properly. But in the buoyancy term, $|\Delta\rho|\boldsymbol{g}$ is still of the same order of magnitude as the inertia, acceleration or viscous stresses of the fluid and therefore can not be ignored. In addition, the variations in the other coefficients, e.g., the dynamic viscosity μ, the specific heat at constant pressure c_p and the thermal conductivity k, which are consequent to variations in density of the amounts stated, must be of the same order and therefore can be ignored as well and be treated as constant everywhere.

In the frame of the Boussinesq approximation, the governing equations of Rayleigh-Bénard convection, which follow the conservation of mass, momentum and energy, can be written as

$$\boldsymbol{\nabla} \cdot \boldsymbol{u} = 0, \tag{2.2}$$

$$\frac{\partial \boldsymbol{u}}{\partial t} + (\boldsymbol{u} \cdot \nabla)\boldsymbol{u} = -\frac{\nabla p}{\rho_0} + \nu \nabla^2 \boldsymbol{u} + g\beta(T - T_0)\boldsymbol{e}_z, \tag{2.3}$$

$$\frac{\partial T}{\partial t} + (\boldsymbol{u} \cdot \nabla)T = \kappa \nabla^2 T. \tag{2.4}$$

Here, $\boldsymbol{u}$, p and T are, correspondingly, velocity field, pressure field and temperature field. $\nu = \mu/\rho_0$ is the kinetic viscosity and $\kappa = k/(c_p\rho_0)$ the thermal diffusivity of the fluid. $\boldsymbol{e}_z$ is the unit vector opposite to the direction of gravity. One should note that in the energy equation (2.4), the viscous dissipation is neglected.

Equations (2.2), (2.3) and (2.4) are the so-called Boussinesq equations and are generally used to describe the motion in Rayleigh-Bénard convection. Next, we move on to introduce the effect of magnetic fields, which takes us to the subject of magnetohydrodynamics.

2.2 Magnetohydrodynamics

Magnetohydrodynamics (MHD) denotes the study of the mutual interaction between magnetic fields and moving, electrically conducting fluids. The fundamentals of MHD have been discussed comprehensively in Shercliff [1965] or Davidson [2016]. In this section, we mainly recall the governing equations of MHD, introduce the quasi-static approximation related to this work and give a short review of the general features of the MHD effects.

2.2.1 The MHD equations

In general, the governing equations of MHD are a combination of the Navier-Stokes equations and a reduced form of Maxwell's equations of electromagnetism. We restrict the discussion to incompressible, viscous, electrically conducting (but not magnetic or dielectric) fluids. We start with the Maxwell's equations, which are written as:

$$\nabla \cdot \boldsymbol{E} = \frac{\rho_e}{\varepsilon_0} \qquad \text{(Gauss' law)}, \tag{2.5}$$

$$\nabla \cdot \boldsymbol{B} = 0 \qquad \text{(Solenoidal nature of } \boldsymbol{B}\text{)}, \tag{2.6}$$

$$\nabla \times \boldsymbol{E} = -\frac{\partial \boldsymbol{B}}{\partial t} \qquad \text{(Faraday's law in differential form)}, \tag{2.7}$$

$$\nabla \times \boldsymbol{B} = \mu_0 \left(\boldsymbol{J} + \varepsilon_0 \frac{\partial \boldsymbol{E}}{\partial t} \right) \qquad \text{(Ampère-Maxwell equation)}, \tag{2.8}$$

where $\boldsymbol{E}$ is the electric field, ρ_e the electrostatic charge density, $\boldsymbol{B}$ the magnetic field and $\boldsymbol{J}$ the electrical current density. ε_0 and μ_0 are the permittivity and permeability of vacuum. In addition we have

$$\boldsymbol{J} = \sigma(\boldsymbol{E} + \boldsymbol{u} \times \boldsymbol{B}) \qquad \text{(Ohm's Law)}, \tag{2.9}$$

$$\nabla \cdot \boldsymbol{J} = -\frac{\partial \rho_e}{\partial t} \qquad \text{(charge conservation)}, \tag{2.10}$$

$$\boldsymbol{F} = q(\boldsymbol{E} + \boldsymbol{u} \times \boldsymbol{B}) \qquad \text{(electrostatic force plus Lorentz force)}, \tag{2.11}$$

where σ is the electrical conductivity and q is the charge. The force law (2.11), when it is integrated over a unit volume conductor, becomes

$$\boldsymbol{F} = \rho_e \boldsymbol{E} + \boldsymbol{J} \times \boldsymbol{B} \qquad \text{(force law per unit volume)}. \tag{2.12}$$

In MHD, where good electrical conductors are considered, these equations can be simplified considerably. Firstly, the charge density ρ_e is infinitesimally small and it does not play any role. Therefore, we can simply drop Gauss's law (2.5). The charge conservation equation (2.10) can simplify to $\nabla \cdot \boldsymbol{J} = 0$ and the force law (2.12) can also simply to Lorentz force $\boldsymbol{F} = \boldsymbol{J} \times \boldsymbol{B}$. Secondly, the displacement currents are also negligible by comparison with the current density $\boldsymbol{J}$. Therefore, the second term on the right of (2.8) can be omitted. In summary, we get the reduced form of Maxwell's equations of electromagnetism:

$$\nabla \times \boldsymbol{B} = \mu_0 \boldsymbol{J} \qquad \text{(Ampère's law),} \tag{2.13}$$

$$\nabla \cdot \boldsymbol{J} = 0 \qquad \text{(charge conservation),} \tag{2.14}$$

$$\nabla \times \boldsymbol{E} = -\frac{\partial \boldsymbol{B}}{\partial t}, \qquad \text{(Faraday's law in differential form),} \tag{2.15}$$

$$\nabla \cdot \boldsymbol{B} = 0 \qquad \text{(Solenoidal nature of } \boldsymbol{B}\text{)} \tag{2.16}$$

in addition with

$$\boldsymbol{J} = \sigma(\boldsymbol{E} + \boldsymbol{u} \times \boldsymbol{B}), \qquad \text{(Ohm's Law),} \tag{2.17}$$

$$\boldsymbol{F} = \boldsymbol{J} \times \boldsymbol{B} \qquad \text{(Lorentz force per unit volume).} \tag{2.18}$$

Note that the Gauss's law is omitted, and the divergence of $\boldsymbol{E}$ is determined from equation (2.17).

To these, we must the Navier-Stokes equation in which $\boldsymbol{F} = \boldsymbol{J} \times \boldsymbol{B}$ appears as a body force per volume to get the governing equations of incompressible MHD.

2.2.2 The quasistatic approximation

If we combine the Ampère's law (2.13), the Faraday's law (2.15) and the Ohm's law (2.17), we obtain an expression relating $\boldsymbol{B}$ to $\boldsymbol{u}$:

$$\frac{\partial \boldsymbol{B}}{\partial t} = -\nabla \times \boldsymbol{E} = -\nabla \times \left(\frac{\boldsymbol{J}}{\sigma} - \boldsymbol{u} \times \boldsymbol{B}\right) = \nabla \times \left(\boldsymbol{u} \times \boldsymbol{B} - \frac{1}{\mu_0 \sigma} \nabla \times \boldsymbol{B}\right). \tag{2.19}$$

Noting that $\nabla \times \nabla \times \boldsymbol{B} = -\nabla^2 \boldsymbol{B}$ (since $\boldsymbol{B}$ is solenoidal), we obtain the temporal evolution equation for $\boldsymbol{B}$:

$$\frac{\partial \boldsymbol{B}}{\partial t} = \nabla \times (\boldsymbol{u} \times \boldsymbol{B}) + \eta \nabla^2 \boldsymbol{B}, \tag{2.20}$$

which is also called induction equation or advection-diffusion equation for $\boldsymbol{B}$. Here, $\eta = (\mu_0 \sigma)^{-1}$ is the magnetic diffusivity.

It is useful to transform the induction equation into a dimensionless form by introducing dimensionless quantities scaled by L, U and L/U, which are the characteristic length, velocity and time of the fluid flow. The scale of the magnetic field is $\boldsymbol{B_0}$, which is typical of the imposed magnetic field in absence of fluid flow. The dimensionless form of the induction equation then becomes

$$\frac{\partial \boldsymbol{B}}{\partial t} = \boldsymbol{\nabla} \times (\boldsymbol{u} \times \boldsymbol{B}) + \frac{1}{R_m} \boldsymbol{\nabla}^2 \boldsymbol{B}, \tag{2.21}$$

where $\boldsymbol{u}$, $\boldsymbol{B}$, $\boldsymbol{\nabla}$ and t are dimensionless variables and

$$R_m = UL/\eta = \mu_0 \sigma U L \tag{2.22}$$

is the magnetic Reynolds number, which represents the ratio of advection to diffusion in the magnetic field. The magnetic Reynolds number also related the magnetic Prandtl number

$$P_m = \nu/\eta \tag{2.23}$$

as $R_m = ReP_m$. Here, Re is the hydrodynamic Reynolds number $Re = UL/\nu$.

According to (2.21), if the magnetic Reynolds number $R_m \ll 1$, the magnetic induction field will be dominated by diffusion and as a consequence the influence of fluid motion on the magnetic field distribution is small and negligible. In the limiting case of $R_m \to 0$, it is possible to obtain a simplified governing model which is approximate to the first order and get rid of the induced magnetic field. This is commonly known as the low-R_m or the quasistatic approximation in MHD.

As we already discussed before in chapter 1, the approximation is valid in most technological applications. And it is actuality also the operating point of laboratory experiments, where $\eta \sim 1m^2/s$, $L \sim 0.1m$ and the internal friction keeps U to a level of around $0.01m/s - 1m/s$, which gives $R_m \sim 0.001 - 0.1$.

The simplifications which result for the full MHD governing equations in the limit of low-R_m are given briefly as follows. We consider the situation when a steady magnetic field $\boldsymbol{B_0}$ is imposed in the flow domain. The fact that the induced magnetic field is negligible means that the total magnetic field $\boldsymbol{B}$ remains $\boldsymbol{B}_0$ and does not vary with time. Then the Faraday's law (2.15) simplifies to $\boldsymbol{\nabla} \times \boldsymbol{E} = 0$, which means the electric field $\boldsymbol{E}$ is curl-free and can be expressed as the gradient of a scalar electrostatic potential V as $E = -\boldsymbol{\nabla} V$. The Ohm's law (2.17) therefore becomes

$$\boldsymbol{J} = \sigma(-\boldsymbol{\nabla} V + \boldsymbol{u} \times \boldsymbol{B}_0), \tag{2.24}$$

The Lorentz force per unit volume (2.18), which appears as body force in Navier-Stokes equation, becomes

$$\boldsymbol{F} = \boldsymbol{J} \times \boldsymbol{B}_0. \tag{2.25}$$

Moreover, since $\boldsymbol{\nabla} \cdot \boldsymbol{J} = 0$, the electrostatic potential V can be solved by the Poisson's equation

$$\boldsymbol{\nabla}^2 V = \boldsymbol{\nabla} \cdot (\boldsymbol{u} \times \boldsymbol{B}_0), \tag{2.26}$$

with some suitable boundary conditions, which are given later in the text.

2.2.3 MHD effects in low-R_m flow

Influence of an imposed magnetic field on a liquid metal flow have been studied extensively (see, e.g., [Boeck *et al.*, 2008; Branover, 1978; Bühler *et al.*, 2017; Davidson, 2016; Krasnov *et al.*, 2017, 2013, 2012; Molokov *et al.*, 2007; Moreau, 1990; Pothérat & Klein, 2017; Thess & Zikanov, 2007; Zikanov *et al.*, 2014*a*]). Although there is still a wealth of phenomena not fully understood, the main MHD effects in low-Re_m flow can be summarized as follows. Far from walls, the main effect is two-fold. First, the induction of electric currents produces Joule dissipation $\sigma^{-1}J^2$, which serves as an additional mechanism of conversion of kinetic energy of the flow into heat. As a result, an imposed magnetic field can delay the transition to turbulence in classical hydrodynamic system. Above the transition limit, intensity of turbulence decreases generally with the strength of the magnetic field. Secondly, the flow becomes anisotropic. It can be seen from the Joule dissipation of a Fourier velocity mode $\hat{\boldsymbol{u}}(\boldsymbol{k},t)$, which can be written as $\sigma B_0^2 \rho^{-1} \mid \hat{\boldsymbol{u}} \mid^2 cos^2\alpha$ [Alemany *et al.*, 1979; Zikanov & Thess, 1998], where α is the angle between the imposed magnetic field $\boldsymbol{B}_0$ and the wave number vector $\boldsymbol{k}$. This shows that the Joule dissipation increases from zero at $\boldsymbol{k} \perp \boldsymbol{B}_0$ to maximum $\boldsymbol{k} \parallel \boldsymbol{B}_0$. Therefore, the magnetic field tends to eliminate velocity gradients in the direction of the field lines and elongates flow structures in the same direction. If the magnetic field is sufficiently strong, the flow becomes axisymmetrically anisotropic or approaches a two-dimensional state with all variables uniform in the direction of magnetic field. Also, since the anisotropy inhibits the energy transfer to small scales, the quasi-2D flows tend to be dominated by large-scale structures. In the flow with walls, the MHD flow states and structures are additionally strongly affected by the global distribution of electric currents and the resulting balance between the Lorentz force, pressure gradient and viscous shear stress. A good illustration is the flow in a rectangular duct with transverse magnetic field, which combines the key effects: magnetic suppression, anisotropy and strong mean shear in the presence of walls. At a strong magnetic field, the flow develops a flat core and characteristic MHD boundary layers, namely, the Hartmann boundary layer at the walls perpendicular to the magnetic field, whose thickness δ_{Ha} scales as Ha^{-1} and the Shercliff boundary (side) layer at the walls parallel to the magnetic field, whose thickness δ_{Sh} scales as $Ha^{-1/2}$. The structures are additionally influenced by the electric conductivity of walls (see, e.g., [Krasnov *et al.*, 2017, 2012] for a discussion). Moreover, the fact that mean shear is nearly absent in the core, but strong within the boundary layers implies that these layers play a critical role in the laminar-turbulent transition in MHD tube-flows. Krasnov *et al.* [2013] have revealed that the transition to turbulence, in fact, first occurs near the sidewalls, while the Hartmann layers and the core flow remain laminar.

2.3 Magnetoconvection

2.3.1 Mathematical model

We consider a flow of liquid metal, which is incompressible, Newtonian, and electrically conducting, confined in a rectangular geometry with size of $L_x \times L_y \times H$, schematically shown in figure 1.3, with x, y as horizontal and z as vertical directions, respectively. The flow is driven by a vertical temperature gradient, which is created by setting the upper wall as a cold wall with a constant temperature T_{top}, and the bottom wall as a hot wall with a constant temperature $T_{\mathrm{bottom}} > T_{\mathrm{top}}$. The system is subjected to a uniform constant magnetic field $\boldsymbol{B}_0$.

After applying the Boussinesq approximation of convection and the quasistatic approximation of MHD, the system of governing equations can be written as

$$\boldsymbol{\nabla} \cdot \boldsymbol{u} = 0, \tag{2.27}$$

$$\frac{\partial \boldsymbol{u}}{\partial t} + (\boldsymbol{u} \cdot \nabla)\boldsymbol{u} = -\frac{\nabla p}{\rho_0} + \nu \nabla^2 \boldsymbol{u} + \frac{1}{\rho_0}(\boldsymbol{J} \times \boldsymbol{B}_0) + g\beta(T - T_0)\boldsymbol{e}_z, \tag{2.28}$$

$$\frac{\partial T}{\partial t} + (\boldsymbol{u} \cdot \nabla)T = \kappa \nabla^2 T, \tag{2.29}$$

$$\boldsymbol{J} = \sigma(-\boldsymbol{\nabla} V + \boldsymbol{u} \times \boldsymbol{B}_0), \tag{2.30}$$

$$\boldsymbol{\nabla}^2 V = \boldsymbol{\nabla} \cdot (\boldsymbol{u} \times \boldsymbol{B}_0). \tag{2.31}$$

Here, the internal energy sinks, such as Joule dissipation, viscous dissipation and other sinks due to nuclear radiation or chemical reaction are neglected in the energy equation (2.29). These internal energy sources or sinks remain small in comparison to the conduction of heat for ordinary liquids (such as water and liquid metal) in the Boussinesq regime.

To make the equations dimensionless, we use the height of the cell H, the free-fall velocity $U_\mathrm{f} = \sqrt{g\beta\Delta T H}$, the external magnetic field strength B_0, and the imposed temperature difference $\Delta T = T_\mathrm{bottom} - T_\mathrm{top}$ as typical scales for length, velocity, magnetic field and temperature respectively. The corresponding typical scales for time, pressure, electric potential and electric current density are respectively the free-fall time $T_f = H/U_f$, $\rho_0 U_f^2$, HU_fB_0 and $\sigma B_0 U_f$. The dimensionless governing equations are then given by:

$$\nabla \cdot \boldsymbol{u} = 0\,, \tag{2.32}$$

$$\frac{\partial \boldsymbol{u}}{\partial t} + (\boldsymbol{u}\cdot\nabla)\boldsymbol{u} = -\nabla p + \sqrt{\frac{Pr}{Ra}}\left[\nabla^2\boldsymbol{u} + Ha^2(\boldsymbol{j}\times\boldsymbol{e}_b)\right] + T\boldsymbol{e}_z\,, \tag{2.33}$$

$$\frac{\partial T}{\partial t} + (\boldsymbol{u}\cdot\nabla)T = \frac{1}{\sqrt{RaPr}}\nabla^2 T\,, \tag{2.34}$$

Here, $\boldsymbol{u}$, p and T are, correspondingly, non-dimensional velocity field, pressure field and temperature field. $\boldsymbol{e}_b$ is the unit vector in the direction of the imposed magnetic field $\boldsymbol{B}_0$. The non-dimensional electric current density $\boldsymbol{j}$ is given by

$$\boldsymbol{j} = -\nabla\phi + \boldsymbol{u}\times\boldsymbol{e}_b, \tag{2.35}$$

and satisfies the divergence-free constraint $\nabla\cdot\boldsymbol{j} = 0$. The non-dimentional electric potential ϕ is determined from the following Poisson equation

$$\nabla^2\phi = \nabla\cdot(\boldsymbol{u}\times\boldsymbol{e}_b). \tag{2.36}$$

The non-dimensional control parameters involved in the system are are the Prandtl number Pr, the Rayleigh number Ra, the Hartmann number Ha as well as the aspect ratio Γ, which are defined relatively as

$$Pr = \frac{\nu}{\kappa},\ \ Ra = \frac{g\beta\Delta T H^3}{\nu\kappa},\ \ Ha = B_0 H\sqrt{\frac{\sigma}{\rho\nu}},\ \ \Gamma = \frac{L_x}{H} : \frac{L_y}{H} : 1. \tag{2.37}$$

The Hartmann number Ha is additionally related to Chandrasekhar number Q as

$$Q = Ha^2 = \frac{B_0^2 H^2 \sigma}{\rho\nu}. \tag{2.38}$$

The boundary conditions at all walls are the no-slip condition for velocity

$$\boldsymbol{u}|_{\text{walls}} = 0, \tag{2.39}$$

and the perfect electric insulation for electric potential

$$\left.\frac{\partial \phi}{\partial n}\right|_{\text{walls}} = 0. \tag{2.40}$$

For the temperature, the top and bottom walls are set as isothermal with different constant temperature

$$T|_{z=-0.5} = 0.5,\ T|_{z=0.5} = -0.5, \tag{2.41}$$

and the side walls are adiabatic with

$$\left.\frac{\partial T}{\partial n}\right|_{\text{side walls}} = 0. \tag{2.42}$$

In response to the input parameters Γ, Pr, Ra and Ha, heat and momentum fluxes are established. The global heat transport is determined by the Nusselt number which is defined as

$$Nu = 1 + \sqrt{RaPr} < u_z T >_{\text{V,t}}. \tag{2.43}$$

The global momentum transport is expressed by Reynolds number, which is defined as

$$Re = u_{rms} Re_f = \sqrt{\frac{Ra}{Pr}} u_{rms}. \tag{2.44}$$

Here, $u_{rms} = \sqrt{< u_i^2 >_{\text{V,t}}}$ is the root mean square (r.m.s.) velocity. $< \cdot >_{\text{V,t}}$ stands for a combined volume and time average.

2.3.2 Boundary layers

Boundary layers in a classic system of Rayleigh-Bénard convection include the thermal boundary layer and velocity boundary layer. The mean thermal boundary layer thickness scales inversely with the Nusselt number Nu and is given by

$$\delta_T = \frac{H}{2Nu}. \tag{2.45}$$

The mean boundary layer thickness of the velocity field scales with the square root of the Reynolds number Re, and is given by

$$\delta_v = \frac{aH}{\sqrt{Re}}, \tag{2.46}$$

where a is a free parameter that is adjusted to the case of a Prandtl-Blasius-type boundary layer, which is normally set to $a = 1/4$ following Grossmann & Lohse [2001].

In magnetoconvection, two further boundary layer thickness what relevant for the MHD problem should be considered. These are the Hartmann layer thickness at walls perpendicular to the magnetic field which is scaling to the inverse of the Hartmann number Ha and is given by

$$\delta_{Ha} = \frac{a_1}{Ha}, \tag{2.47}$$

and the Shercliff boundary layer thickness at the walls parallel to the magnetic field which is scaling to the inverse of the square root of the Hartmann number Ha and is given by

$$\delta_{Sh} = \frac{a_2}{\sqrt{Ha}}, \tag{2.48}$$

Constants a_1 and a_2 are of order $\mathcal{O}(1)$ and geometry-dependent. For simplicity, we set $a_1 = a_2 = 1$ for the following.

2.3.3 Dimensionless dissipation rates

Here we would like to present the dimensionless dissipation rates that will be used in this thesis. If we take the dot product of dimensionless $\boldsymbol{u}$ with the dimensionless Navier-Stokes equation (2.33), we obtain an equation for kinetic energy as

$$\begin{aligned}\frac{\partial}{\partial t}\left(\frac{u^2}{2}\right) = & -\boldsymbol{\nabla}\cdot\left[\left(p+\frac{u^2}{2}\right)\boldsymbol{u}\right] + \nabla\cdot(u_i\tau_{ij}) - 2\sqrt{\frac{Pr}{Ra}}S_{ij}S_{ij} \\ & + Ha^2\sqrt{\frac{Pr}{Ra}}(\boldsymbol{j}\times\boldsymbol{e}_b)\cdot\boldsymbol{u} + u_z T,\end{aligned} \tag{2.49}$$

where, $S_{ij} = (\partial u_i/\partial x_j + \partial u_j/\partial x_i)/2$ is the strain-rate tensor and $\tau_{ij} = 2\sqrt{\frac{Pr}{Ra}}S_{ij}$ is the viscous stress. The working rate of the Lorentz force can be written as

$$Ha^2\sqrt{\frac{Pr}{Ra}}(\boldsymbol{j}\times\boldsymbol{e}_b)\cdot\boldsymbol{u} = -Ha^2\sqrt{\frac{Pr}{Ra}}(\boldsymbol{u}\times\boldsymbol{e}_b)\cdot\boldsymbol{j} = -Ha^2\sqrt{\frac{Pr}{Ra}}j^2 - \boldsymbol{\nabla}\cdot(\phi\boldsymbol{j}). \tag{2.50}$$

Gathering all the divergence terms together, the energy equation is rewritten as

$$\frac{\partial}{\partial t}\left(\frac{u^2}{2}\right) = \nabla\cdot(*) - 2\sqrt{\frac{Pr}{Ra}}S_{ij}S_{ij} - Ha^2\sqrt{\frac{Pr}{Ra}}j^2 + u_z T. \tag{2.51}$$

The divergence term vanishes when the equation is integrated over the entire volume and we obtain

$$\frac{d}{dt}\int \frac{u^2}{2} dV = -\int \varepsilon \, dV - \int \varepsilon_j \, dV + \int u_z T \, dV. \tag{2.52}$$

Here,

$$\varepsilon = 2\sqrt{\frac{Pr}{Ra}} S_{ij} S_{ij} \tag{2.53}$$

is known as viscous dissipation rate or kinetic energy dissipation rate, and

$$\varepsilon_j = Ha^2 \sqrt{\frac{Pr}{Ra}} j^2 \tag{2.54}$$

is known as Joule dissipation rate due to Ohmic heating.

The roles of the viscous dissipation rate ε, the Joule dissipation rate ε_j and $u_z T$ are clearly shown in equation (2.52) that ε and ε_j tend to cause a declination of kinetic energy, while $u_z T$ is the source of potential energy.

In a the system of magnetoconvection, we should also add the thermal dissipation rate which is defined as

$$\varepsilon_T(\boldsymbol{x}, t) = \frac{1}{\sqrt{Ra Pr}} (\boldsymbol{\nabla} T)^2 . \tag{2.55}$$

Chapter 3

Numerical procedure

3.1 Finite-difference solver

The dimensionless quasistatic magnetoconvection equations introduced in section 2.3.1 are solved by direct numerical simulations (DNS) with our in-house FORTRAN code. The solver is based on the projection-type finite difference scheme described as the scheme B in Krasnov *et al.* [2011] and later extended to flows with thermal convection [Zikanov *et al.*, 2013], which has demonstrated its capabilities in simulations of incompressible MHD flows at high Reynolds number, Hartmann number and Rayleigh number (see, e.g., [Krasnov *et al.*, 2013, 2012; Lv & Zikanov, 2014; Zhang & Zikanov, 2014; Zikanov *et al.*, 2014*b*]). The scheme is of the second order in space and time. The spatial discretization is performed on a structured collocated grid. Consistent approximation of differential operator is achieved via the use of velocity and current fluxes obtained by conservative interpolation to half-integer grid points, which renders the scheme perfectly conservative in regards of the mass, momentum, electric charge, and thermal energy while the conservation of kinetic energy is satisfied with a dissipative error of the third order. The time discretization for the momentum transport equations and the convective terms in the heat transport equation is explicit and based on the Adams-Bashfort/backward difference formula. The diffusive term in the heat transport equation is treated implicitly to avoid the time reduction due to the small value of Prandtl number Pr, which is typical for liquid metals. The entire procedure of advancing from the time layer n to $n+1$ includes solving the Poisson equation for electric potential

$$\boldsymbol{\nabla}^2 \phi^n = \boldsymbol{\nabla} \cdot (\boldsymbol{u}^n \times \boldsymbol{e}_b), \tag{3.1}$$

computing the electric current

$$\boldsymbol{j}^n = -\boldsymbol{\nabla} \phi^n + \boldsymbol{u}^n \times \boldsymbol{e}_b, \tag{3.2}$$

computing

$$\boldsymbol{F}^n = -(\boldsymbol{u}^n \cdot \nabla)\boldsymbol{u}^n - \boldsymbol{\nabla} p^n + \sqrt{\frac{Pr}{Ra}}\boldsymbol{\nabla}^2\boldsymbol{u}^n + \sqrt{\frac{Pr}{Ra}}Ha^2(\boldsymbol{j}^n \times \boldsymbol{e}_b) + T^n\boldsymbol{e}_z, \tag{3.3}$$

computing the intermediate velocity $\boldsymbol{u}^*$ for the next time layer using

$$\frac{3\boldsymbol{u}^* - 4\boldsymbol{u}^n + \boldsymbol{u}^{n-1}}{2\Delta t} = 2\boldsymbol{F}^n - \boldsymbol{F}^{n-1}, \tag{3.4}$$

solving the Poisson equation for pressure

$$\boldsymbol{\nabla}^2 p^{n+1} = \frac{3}{2\Delta t}\boldsymbol{\nabla} \cdot \boldsymbol{u}^*, \tag{3.5}$$

and adding the pressure correction to the velocity field to secure mass conservation

$$\boldsymbol{u}^{n+1} = \boldsymbol{u}^* - \frac{2\Delta t}{3}\boldsymbol{\nabla} p^{n+1}. \tag{3.6}$$

The boundary condition for pressure at solid walls are obtained by direct projection of (3.5) on the normal to the wall:

$$\frac{\partial p^{n+1}}{\partial n} = \frac{3}{2\Delta t}\boldsymbol{u}_n^*. \tag{3.7}$$

The temperature for the next time layer T^{n+1} is solved by the semi-implicit equation:

$$\frac{3T^{n+1} - 4T^n + T^{n-1}}{2\Delta t} = 2\boldsymbol{G}^n - \boldsymbol{G}^{n-1} + \frac{1}{\sqrt{RaPr}}\nabla^2 T^{n+1}, \tag{3.8}$$

where $\boldsymbol{G}^n = -\nabla \cdot (T^n\boldsymbol{u}^n)$, with the boundary condition (2.41) and (2.42).

The computational grid is orthogonal and can be clustered in the y, z directions to achieve better resolution of the thin MHD boundary layers, which becomes particularly important for MHD flows with strong magnetic fields (high Ha). A non-uniform grid is generated by applying coordinate transformation. The grid is stretching to the walls as a hyperbolic tangent distribution

$$y = \frac{L_y}{2}\frac{\tanh(\mathrm{A_y}\xi_\mathrm{y})}{\tanh(\mathrm{A_y})}, \quad z = \frac{H}{2}\frac{\tanh(\mathrm{A_z}\xi_\mathrm{z})}{\tanh(\mathrm{A_z})}. \tag{3.9}$$

Here, $-1 \leq \xi_y, \xi_z \leq 1$ is the uniformly distributed coordinate. A_y and A_z are the parameters that account for the strength of clustering.

The Poisson equation for pressure and electric potential, and elliptic equation for temperature are solved in Fourier space by applying the cosine transform in the x direction in our geometry. The cosine expansion is a natural choice since it automatically matches the imposed boundary conditions $\partial f/\partial x = 0$ for pressure, electric potential and temperature at $x = 0$ and $x = L_x$. The advantage of using the space of eigenfunctions is that full 3D Poisson problem $\Delta f = r$ is transformed into a series of 2D separable elliptic PDE problems $\Delta_{yz}\hat{f}_k - k^2\hat{f}/_k = \hat{r}_k$ for coefficients of the Fourier/Cosine expansion. Here $\hat{f}_k$ and $\hat{r}_k$ are the Fourier/ Cosine coefficients, Δ_{yz} is the 2D Laplace operation in (y,z)-cross section and k is the wavenumber in x direction. Each of these 2D problems is discretized by central differences of second order and solved by the cyclic reduction method, a part of the software package Fishpack. More details of the solver can be found in Krasnov *et al.* [2011] and Zikanov *et al.* [2014*b*].

For the effective use of the modern massive-parallel computers and clusters the solver is parallelized with MPI (distributed memory) and Open MP (shared memory) interfaces. This hybrid approach allows performing simulations at very large computational resolution (of the order of 10^9 points), which is a necessary prerequisite for wall-bounded MHD flows at high Ha and Ra numbers, where small-scale turbulence and thin boundary layers are typically present.

One modification aimed to improve performance in the case of convection with very strong vertical magnetic field (high Ha), where the flow is quasisteady as described below. The modification concerns the diffusive term $\sqrt{\frac{Pr}{Ra}}\boldsymbol{\nabla}^2\boldsymbol{u}$, which can be treated either explicitly (as in equation (3.3)) or implicitly. The implicit treatment has been implemented to tackle flow regimes at high Ha. In these cases, the viscous terms can become a source of numerical instability, which also imposes severe limitations on the time step. The implicit treatment of diffusive terms involves three additional elliptic problems to be solved for all three velocity components, therefore, computational time per integration time step increases. Our benchmarks with the implicit scheme show that its performance is about two to three times slower than the fully explicit version. At the same time, for Hartmann numbers $Ha > 1000$ the time-step can be up to 10 times higher. As a result, for a certain combination of parameters that is typically associated with a requirement of strong grid clustering, the computational efficiency can benefit from the implicit scheme, since the overall speed-up may increase approximately by factor of 5.

3.2 Grid sensitivity

Two aspects of the grid have been considered. One is the ability to correctly reproduce the turbulent Rayleigh-Bénard convection. Another is the accurate resolution of the Hartmann boundary layers, i.e. the boundary layers at walls perpendicular to

Ha	$N_x \times N_y \times N_z$	A_z	Δt	Nu	Re	N_{Ha}
0	$128 \times 128 \times 128$	1.5	1×10^{-3}	5.77	2740	–
	$128 \times 128 \times 128$	2.0	1×10^{-3}	5.78	2754	–
	$256 \times 256 \times 256$	2.0	5×10^{-4}	5.82	2769	–
300	$128 \times 128 \times 128$	2.0	1×10^{-3}	2.41	635	3
	$256 \times 256 \times 256$	2.0	5×10^{-4}	2.43	636	6
	$384 \times 384 \times 384$	2.0	2.5×10^{-4}	2.43	636	9

Table 3.1: Grid sensitivity analysis for Rayleigh-Bénard convection at $Pr = 0.025$, $Ra = 10^6$ in a cubical enclosure ($\Gamma = 1:1:1$) without magnetic field $Ha = 0$ and with a vertical magnetic field $Ha = 300$. We show the number of grid points in three direction and grid points clustering coefficient A_z in z direction. The grid is uniform in horizontal x, y direction. We check the global Nusselt number Nu, the Reynolds number Re and the number of grid points within Hartmann boundary layers, which is calculated approximately as Ha^{-1}. Δt is the time integration step.

the imposed magnetic field with thicknesses scaling as Ha^{-1}. Grid sensitivity study has been conducted considering Rayleigh-Bénard convection in a cubical enclosure at $Pr = 0.025$ and $Ra = 10^6$ without magnetic field, $Ha = 0$, and with a vertical magnetic field, $Ha = 300$, respectively. The results are summarized in table 3.1. We compare the global heat and momentum transfer, expressed by global Nusselt number Nu and Reynolds number Re respectively. It is shown that the global Nu and Re are relatively insensitive to the grid resolution. The resolution $128 \times 128 \times 128$ with $A_z = 2.0$ is already quite reasonable to calculate pure Rayleigh-Bénard convection denoted by $Ha = 0$ for $Ra = 10^6$, $Pr = 0.025$. For Rayleigh-Bénard convection with vertical magnetic field at $Ha = 300$, even the values computed on the crudest grid with 128^3 points differ from the values on the grid with 348^3 points by less than 1%. The difference between the values obtained on the grids with 256^3 and 384^3 decreases below 0.2%. We confirm that the resolution $256 \times 256 \times 256$ with $A_z = 2.0$ is fairly reasonable to calculate magnetic Rayleigh-Bénard convection at $Ha \leq 300$. This resolution has 6 points within the Hartmann layer at $Ha = 300$, which is calculated approximately as Ha^{-1}. The maximum and minimum grid steps in vertical direction are $\Delta z_{max} \approx 0.008$, $\Delta z_{min} \approx 0.0006$. And the grid steps are uniform in horizontal direction with $\Delta x = \Delta y \approx 0.004$. The time integration step is $\Delta t = 5 \times 10^{-4}$. At higher Ha, finer resolutions request. For all the DNS in this thesis, we keep at least 6 grid points within the Hartmann boundary layers. One should also notice that the grid points should not be stretched to the wall too much. Otherwise, the computational grid will be too coarse in the bulk to resolve the Rayleigh-Bénard convection system properly, according to the resolution criteria of Grötzbach [1983] for DNS of Rayleigh-Bénard which is refined by Scheel *et al.* [2013].

Ra	$N_x \times N_y \times N_z$	A_z	$Nu_{Ha=0}$	$Re_{Ha=0}$	$Nu_{Ha=100}$	$Re_{Ha=100}$
10^5	$128 \times 128 \times 128$	2.0	3.10	1021	1.64	274
5×10^5	$128 \times 128 \times 128$	2.0	4.86	2120	3.39	866
10^6	$256 \times 256 \times 256$	2.0	5.82	2730	4.43	1402
2×10^6	$256 \times 256 \times 256$	2.0	7.00	3632	5.79	2160

Table 3.2: Parameters for verification. The Prandtl number is fixed to $Pr = 0.025$, the aspect ratio to $\Gamma = 1:1:1$. The Rayleigh number Ra, the grid resolution with clustering coefficient A_z in z direction, the Nusselt number without magnetic field $Nu_{Ha=0}$ and with vertical magnetic field $Nu_{Ha=100}$, the Reynolds number without magnetic field $Re_{Ha=0}$ and with vertical magnetic field $Re_{Ha=100}$ are given.

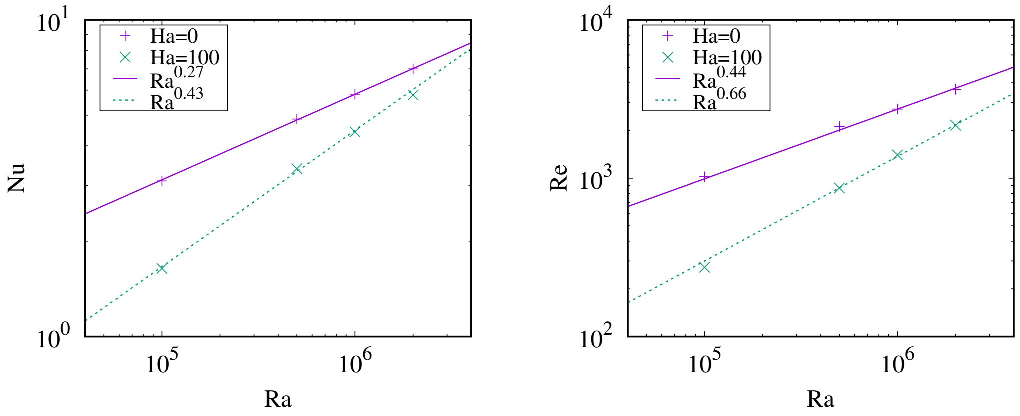

Figure 3.1: Left: Nu vs Ra with (×) and without (+) vertical magnetic field. The solid line presents the $Ra^{0.27}$ scaling and the dashed line presents the $Ra^{0.43}$ scaling. Right: Re vs Ra with (×) and without (+) vertical magnetic field. The solid line presents the $Ra^{0.44}$ scaling and the dashed line presents the $Ra^{0.66}$ scaling.

3.3 Verification

A preliminary verification of the numerical model has been conducted by generating the scaling law between the Nusselt number Nu and the Rayleigh number Ra in Rayleigh-Bénard convection in the absence of magnetic field and in the presence of a vertical magnetic field in a cubical enclosure. We consider a range of Ra from 10^5 to 2×10^6 at $Pr = 0.025$ without magnetic field ($Ha = 0$) and with a vertical magnetic field of $Ha = 100$. Parameters are summarized in table 3.2. As shown in figure 3.1, in the absence of magnetic field, we find a Nu versus Ra with a scaling law $Nu = (0.14 \pm 0.01)Ra^{0.27}$. The results agree very well with experiments by Rossby [1969], Cioni *et al.* [1997] and Takeshita *et al.* [1996] within uncertainty. The dependence of Reynolds number Re on Rayleigh number Ra follows $Re = (6.25 \pm 0.09)Ra^{0.44}$, which also agrees within uncertainty with the experimental results by Takeshita *et al.* [1996], where they found $Re = 6.24Ra^{0.46\pm0.02}$. With a vertical magnetic field, we find the Nu versus Ra with a scaling law $Nu = 0.01Ra^{0.43}$, which agrees very well to the regime II in Cioni *et al.* [2000], shown as $Nu = 0.1Ra^{0.43}Q^{-0.25}$. Here, $Q = Ha^2$. This concludes the verification of the numerical procedure adopted to model the Rayleigh-Bénard convection with and without magnetic field. In addition, with a vertical magnetic field, the Re versus Ra with a scaling law $Re = (0.15 \pm 0.04)Ra^{0.66\pm0.02}$.

Chapter 4

Rayleigh-Bénard convection under effects of a horizontal magnetic field

4.1 Introduction and problem setup

This chapter presents the numerical study of turbulent Rayleigh-Bénard convection in liquid metal under effects of an externally applied horizontal magnetic field. As mentioned in chapter 1, it is known that a sufficiently strong horizontal magnetic field tends to organize the convective motion into a flow pattern of quasi-two-dimensional rolls aligned with the magnetic field and the wave number of the convection rolls has a tendency to decrease with increasing of the Rayleigh number and to increase with increasing strength of the magnetic field [Burr & Müller, 2002; Tasaka *et al.*, 2016]. Particularly, Yanagisawa *et al.* [2013] and Tasaka *et al.* [2016] studied convection pattern in liquid gallium under an imposed horizontal magnetic field experimentally and established a regime diagram of convection patterns in relation to the values of Ra and Ha^2 for a square vessel with aspect ratio 5 : 5 : 1. The most remarkable one is the regime of spontaneous flow reversals characterized by reversals of the flow direction in the roll structure under an intermittent horizontal magnetic field. The relation between the roll size under magnetic field and the geometry vessel is an important constraint on the flow behavior, suggesting that the locations of the regime boundaries may depend on the aspect ratio of the vessel. Consideration of the other geometries and aspect ratios will give a deeper understanding of the spontaneous, repetitive transition of large scale convection structures.

Here we present DNS results of convection in liquid metal in two different geometries either a box with a square horizontal cross section and an aspect ratio of $\Gamma = 4 : 4 : 1$ or a box with a long rectangular horizontal cross section and an aspect ratio of $\Gamma = 1 : 4 : 1$. The magnetic field B_0 is homogeneously imposed in y direction

Run	Ra	Ha	Γ	$N_x \times N_y \times N_z$	Grid factor ($A_y = A_z$)
series 1	10^6	$0, 50, 100$ $150, 200, 300$	$4:4:1$	$512 \times 512 \times 128$	2.0
series 2	10^6	$0, 50, 100$ $150, 200, 300$	$1:4:1$	$128 \times 512 \times 128$	2.0

Table 4.1: Parameters of the simulations on turbulent Rayleigh-Bénard convection in liquid metal under effects of an externally applied horizontal magnetic field in y direction. The Prandtl number is fixed to $Pr = 0.025$. A_y and A_z are the grid stretching coefficients defined in (3.9).

in both geometry. Input parameters are summarized in table 4.1. The Prandtl number is fixed to $Pr = 0.025$ and the Rayleigh number is fixed to $Ra = 10^6$. With the chosen Ra and Pr, the flow is already turbulent in the absence of magnetic field. The Hartmann number is varying from 0 to 300. For each case, the fully developed Rayleigh-Bénard convection at zero magnetic field is used as initial state. The grid resolution is summarized in table 4.1 as well. The grid is uniform in x direction, and stretching in vertical z direction and in horizontal y direction based on the equation (3.9). Referring to the grid sensitivity study of Rayleigh-Bénard convection under a vertical magnetic field, the resolution is already reasonable to calculate general pattern and global transport for the chosen Ra and Pr even for the highest Hartmann number of $Ha = 300$.

4.2 Results in a square box with aspect ratio $\Gamma = 4:4:1$

In this section, we show the DNS results of the impact of a horizontal magnetic field on liquid metal convection flow in a closed box with a square horizontal cross section and an aspect ratio of $\Gamma = 4:4:1$. The parameters used in this section are summarized in table 4.1 as series 1. The Prandtl number is fixed to $Pr = 0.025$ and the Rayleigh number is fixed to $Ra = 10^6$. The magnetic field B_0 is homogeneously imposed in y direction with the Hartmann number varying from 0 to 300. A part of the results have been published in [Liu *et al.*, 2016].

Figure 4.1 displays snapshots of convection pattern at six different strengths of horizontal magnetic field by the contours of vertical velocity field u_z on middle horizontal cross section ($z = 0$). The regions with the largest vertical velocity magnitude $|u_z|$ can be considered as the boundaries of convective circulations. Blue indicates downwards flow and red means upwards flow. It is shown that the external horizontal magnetic field tends to organize the flow motion as roll-like structures aligned with the magnetic field as expected. With the chosen $Pr = 0.025$, $Ra = 10^6$ and $\Gamma = 4:4:1$,

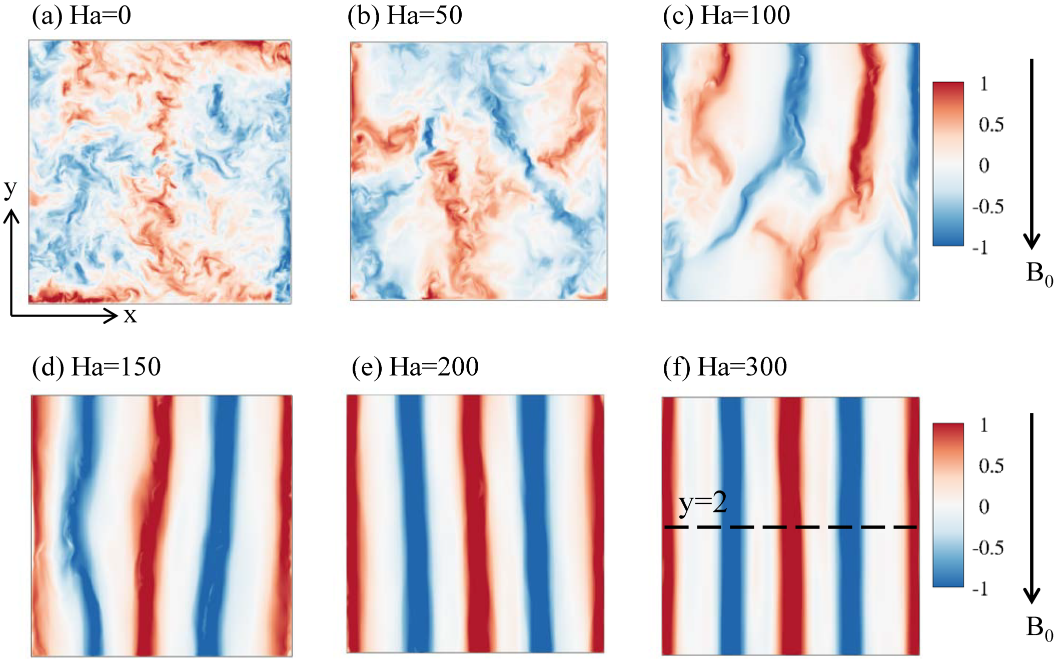

Figure 4.1: Convection pattern under effects of a horizontal magnetic field in y direction for six Ha values with $Pr = 0.025$, $Ra = 10^6$ and $\Gamma = 4:4:1$. Horizontal cross sections at mid-plane ($z = 0$) of instantaneous vertical velocity field u_z at $t = 400T_f$ are shown. Blue indicates downwards flow and red indicates upwards flow. The center of the blue and red contour indicates the boundaries of convection circulations.

the dominant number of rolls is four for $Ha \geq 150$, indicating that the aspect ratio of one roll is ~ 1. With the highest Hartmann number of $Ha = 300$, this four-roll-like structure is quasisteady, while with relatively low magnetic field ($Ha = 150, 200$) the structure is fluctuating with time. Next, we will give a detail report of the behavior of the convection under different strengths of horizontal magnetic fields.

4.2.1 Time dependent patterns

In this subsection, we presents time dependent results of convection under different strengths of magnetic fields. We will show the time-space maps of convection pattern, and the corresponding time evolution of the momentum and heat transport. The time evolution of the momentum transport is described by the time-dependent r.m.s. velocity

$$u_{rms}(t) = \sqrt{< u_x^2 + u_y^2 + u_z^2 >_V}, \tag{4.1}$$

and its three components in different directions, which are defined relatively as

$$u_x(t) = \sqrt{< u_x^2 >_V},\ \ u_y(t) = \sqrt{< u_y^2 >_V},\ \ u_z(t) = \sqrt{< u_z^2 >_V}. \tag{4.2}$$

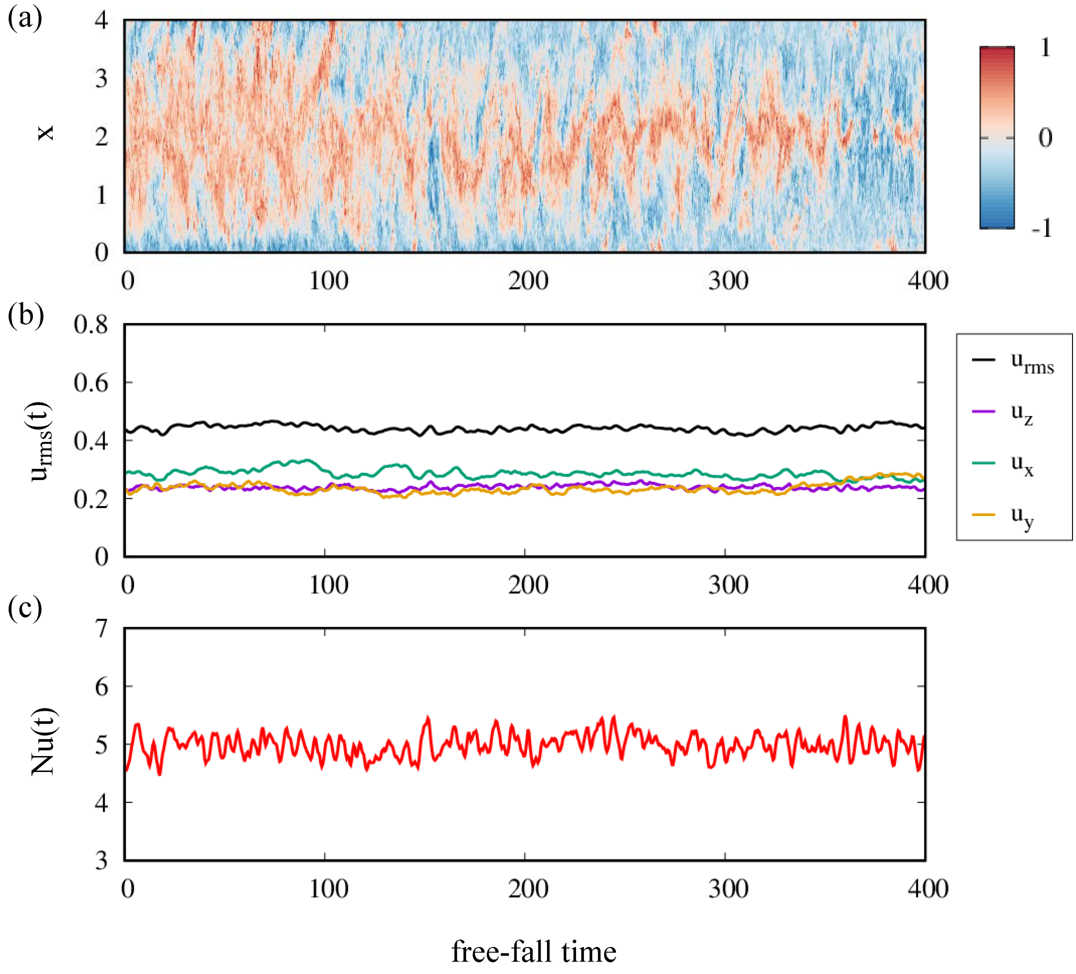

Figure 4.2: Time-dependent results for $Ha = 0$, $Ra = 10^6$ and $\Gamma = 4:4:1$. (a) Time-space maps of vertical velocity u_z along $y = 2$ at horizontal mid-plane ($z = 0$) denoted by the dashed line in panel (f) of figure 4.1. (b) Time various of r.m.s. velocity and its three components (Eq. 4.1 and 4.2). (c) Time various of the Nusselt number (Eq. 4.3).

The time evolution of heat transport is quantified by the the time-dependent Nusselt number

$$Nu(t) = 1 + \sqrt{RaPr} < u_z T >_V . \tag{4.3}$$

Figure 4.2 summarizes the time dependent results for $Ha = 0$ at $Pr = 0.025$, $Ra = 10^6$. Panel (a) shows the the time-space maps of vertical velocity u_z along $y = 2$ at horizontal mid-plane ($z = 0$) denoted by the dashed line in panel (f) of figure 4.1. There are no roll-like structures, but typical large-scale circulations as shown in figure 4.1(a). Panel 4.2(b) displays the time series of r.m.s. velocity. The magnitude of the velocity components in all the three directions are similar which indicates an isotropic convection. Panel (c) shows the time variations of the Nusselt number Nu, and its time-averaged value over 400 free-fall time units is about 4.98.

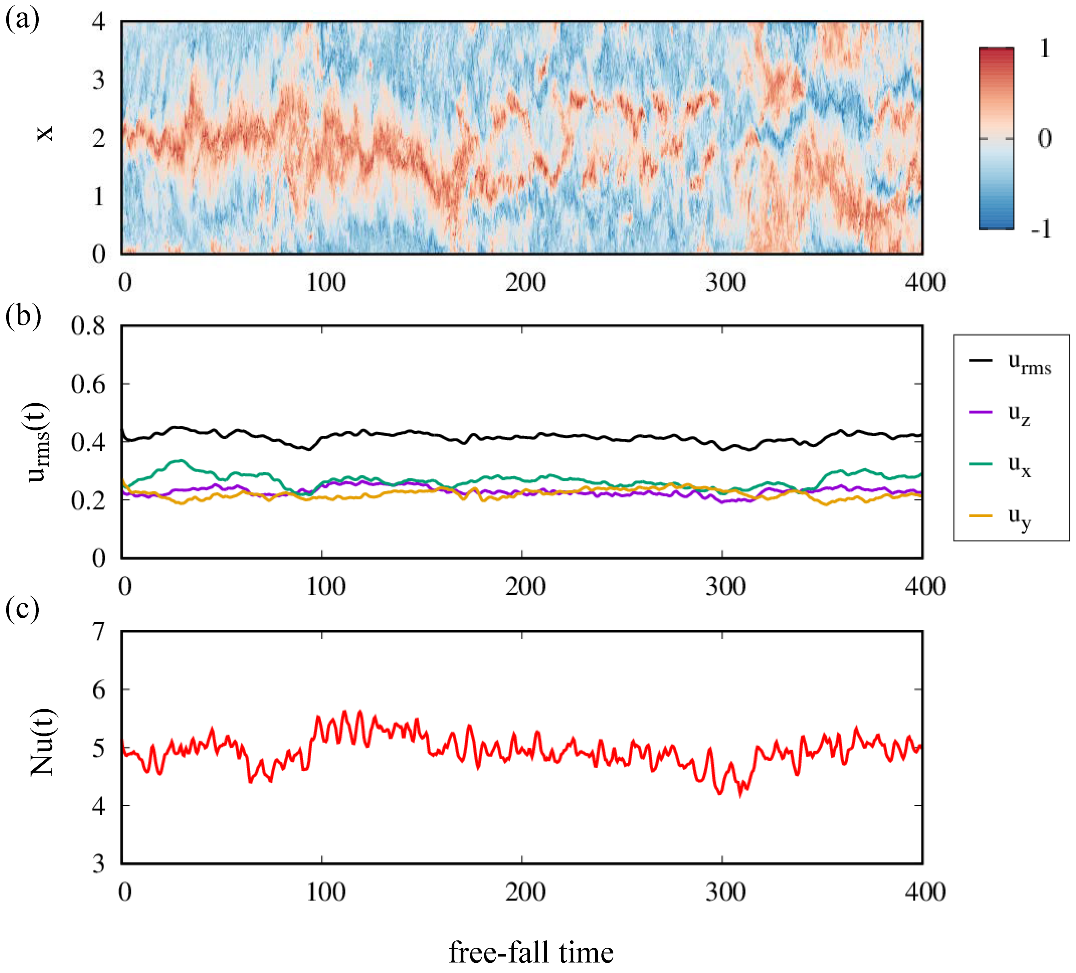

Figure 4.3: Similar figure to 4.2 but for $Ha = 50$, $Ra = 10^6$ and $\Gamma = 4:4:1$. $Ra/Ha^2 = 400$.

Figure 4.3 displays the time dependent results for $Ha = 50$ at $Pr = 0.025$, $Ra = 10^6$. The flow behavior is similar to that without magnetic field as shown in figure 4.2. The magnitude of the three velocity components in all the directions remains comparable, indicating that no roll-like structure is established. The time and volume averaged total r.m.s. velocity is about 0.42 which is about 0.95 times that of $Ha = 0$. The time and volume averaged Nusselt number over 400 free-fall time units is about 4.93 which is slightly smaller than that of $Ha = 0$. The results indicates that a very low magnetic field has no obvious influence on the global convection structure but tends to suppress the small fluctuations which may reduce the heat and momentum transport in the system.

Figure 4.4 summarizes the time dependent results for $Ha = 100$ at $Pr = 0.025$, $Ra = 10^6$. The influence of the horizontal magnetic field becomes observable that flow pattern as shown in panel (a) reveals a three-roll dominated structure and the structure is highly three dimensional (also see figure 4.1(c)). In the *r.m.s* velocity profiles (figure 4.4(b)), we observe irregular high-amplitude fluctuations with the highest magnitude larger than the non-MHD case. The velocity component in y direction which is parallel

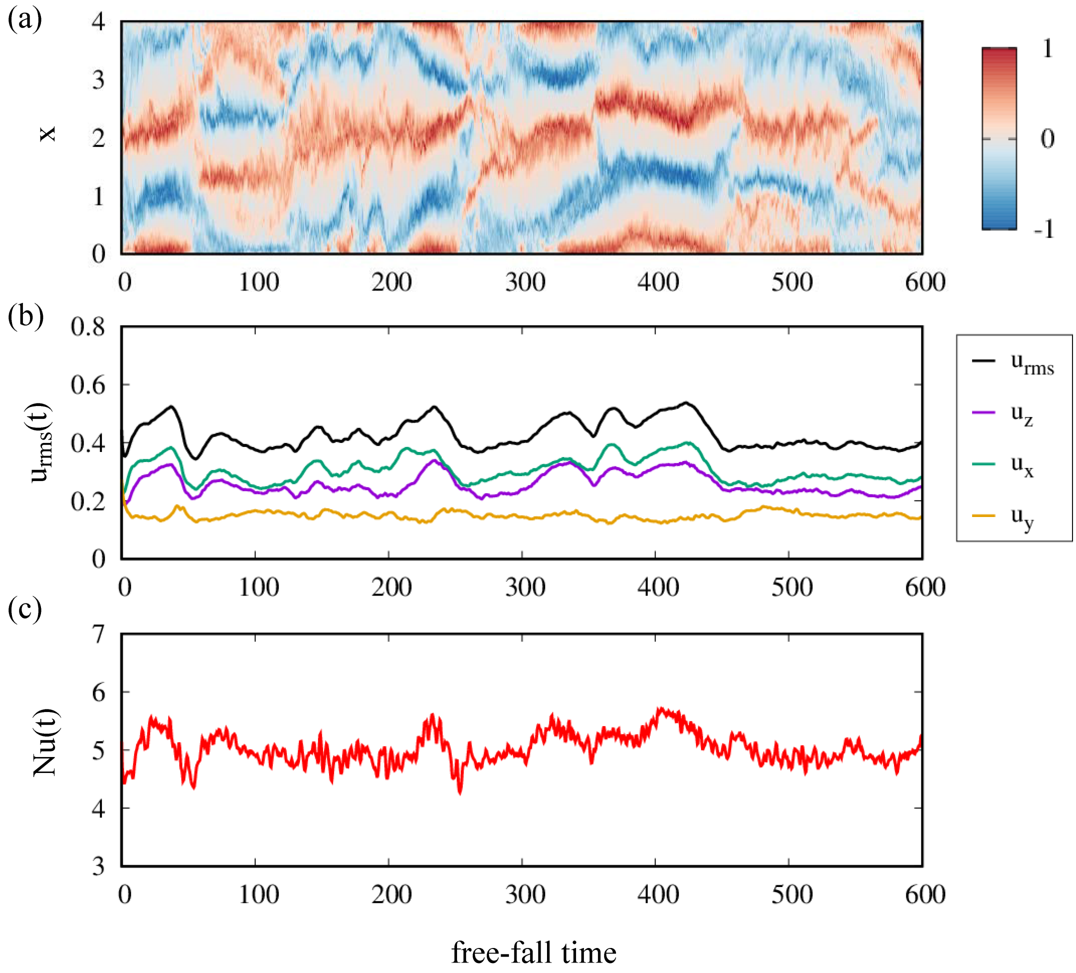

Figure 4.4: Similar figure to 4.2 but for $Ha = 100$, $Ra = 10^6$ and $\Gamma = 4:4:1$. $Ra/Ha^2 = 100$.

to the direction of magnetic field, decreases obviously with its time-averaged value to the total value being 0.34 approximately. For $Ha = 0$, the ratio is about 0.54.

Figure 4.5 shows the time dependent results for $Ha = 150$ at $Pr = 0.025$, $Ra = 10^6$. A dominated four-roll structure is clearly observed in panel (a) and the flow direction in the rolls reverses at irregular time intervals. Figure 4.6 displays 3D pattern for three snapshots at different instants in time denoted by the three vertical dashed lines in 4.5. Time point A ($t = 270$) denotes a position with one highest u_{rms} and C ($t = 340$) denotes the position with the next highest u_{rms}, while B ($t = 303$) denotes the position with the lowest u_{rms} in between. As shown in figure 4.6, at point A, the pattern takes a form of four-roll structure aligned with the imposed magnetic field. This structure has a high values of $u_{rms} \sim 0.68$ which is meanly contributed by the flow motion in x and z directions. The velocity component in y direction, which is parallel to the magnetic field, is about 0.078, its ratio to the total value $u_y/u_{rms} \approx 0.11$, reflecting the strong two dimensional property of the convection rolls. At point B, the four-roll structure evolves to a new structure which is dominated by rolls with larger wavelength. The

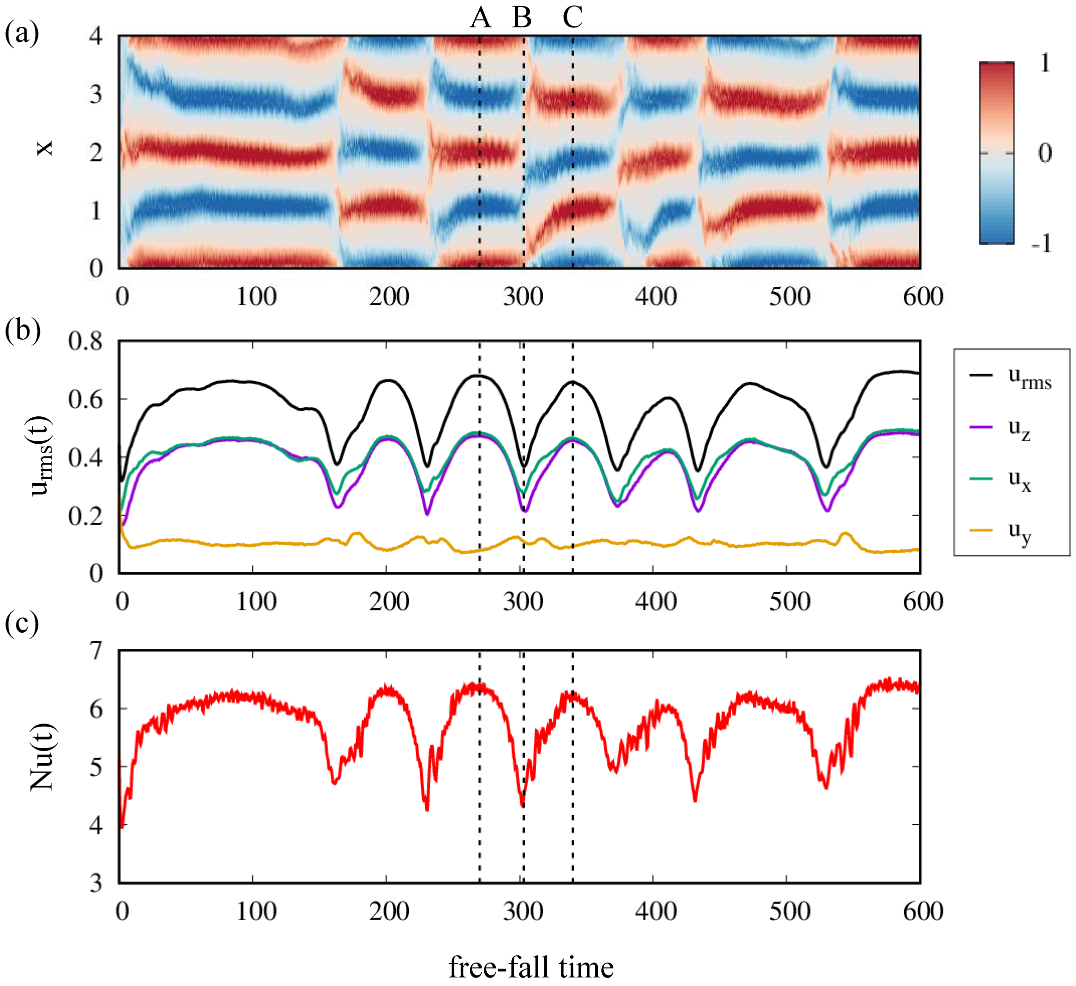

Figure 4.5: Similar figure to 4.2 but for $Ha = 150$, $Ra = 10^6$ and $\Gamma = 4:4:1$. $Ra/Ha^2 = 44.4$.

rolls are broken in the middle and have a low u_{rms} of about 0.37, which is about 0.54 times that at A. But the y-component velocity is increased to 0.11, with its ratio to the total velocity $u_y/u_{rms} \approx 0.30$. At point C, the flow evolves to a new quasi 2D four-roll structure aligned with the imposed magnetic field with the u_{rms} increasing to a new high value of 0.66 and u_y decreasing to a low value of 0.094. However, the rotations of the rolls are reversed comparing to the structure at A. The profile of the Nusselt number Nu has similar fluctuation as the u_{rms} which means that the quasi 2D four-roll structure can transport more heat than the structures in between. The Nusselt numbers Nu at A, B, C in figure 4.5(c) are 6.41, 4.48, 6.28 respectively.

Figure 4.7 presents the time dependent results for $Ha = 200$ at $Pr = 0.025$, $Ra = 10^6$. Similar results are observed as for $Ha = 150$ that the convection is dominated by a four-roll structure aligned with the imposed magnetic field with the flow direction in the rolls reversing spontaneously, which causes the high-amplitude and low-frequency fluctuation in the velocity profile as well as in the heat transport profile. The total *r.m.s* velocity u_{rms} has a high value when a quasi 2D four-roll structure is established and

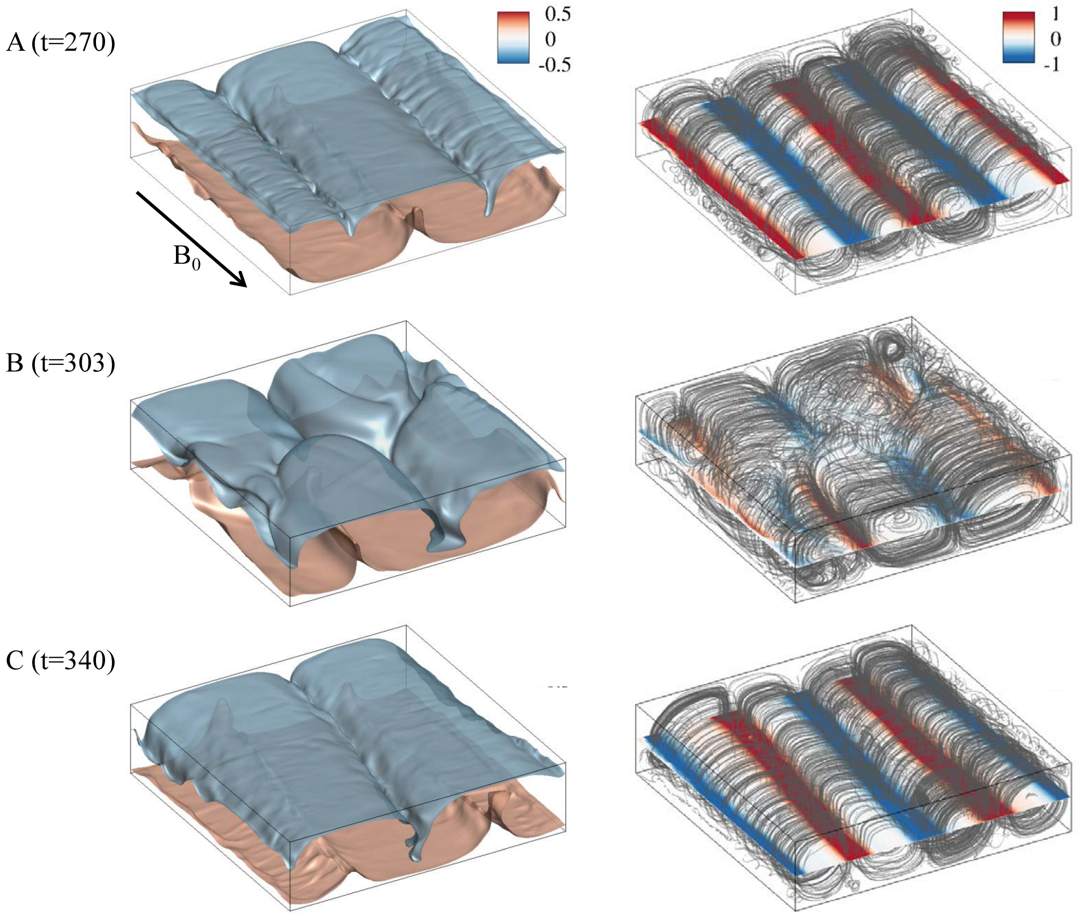

Figure 4.6: 3D structures of convection flow for $Ha = 150$, $Ra = 10^6$ and $\Gamma = 4:4:1$. Three snapshots are shown for three different instants in time denoted by the three vertical dashed lines in figure 4.5. Left column shows two isosurfaces of temperature field ($T = \pm 0.25$). Right column shows streamlines of 3D velocity field together with the horizontal distribution of vertical velocity u_z at mid-plane ($z = 0$) with red for upwards motion and blue for downwards motion.

has a low value in between as well as the Nusselt number Nu, while the y-component velocity, which is parallel to the magnetic field, has a small value in a four-roll like structure and a higher value in between. Similar to the analysis for $Ha = 150$, we mark three time points in figure 4.7 by three vertical dashed lines that A denotes the position with the first highest u_{rms} during one reversal procedure, B the position with the lowest u_{rms} and C the position with the next new highest u_{rms}. The u_{rms} at A, B, C in figure 4.7(b) are 0.70, 0.33, 0.70 respectively, the u_y/u_{rms} are 0.09, 0.24, 0.09 and the Nu in figure 4.7(c) are 6.57, 4.35, 6.56 respectively. The whole procedure from A ($t = 223$) to C ($t = 400$) lasts for 177 free-fall time unit, which is about 2.5 times that for $Ha = 150$. And for $Ha = 150$, the period of the four-roll structure breaking (A to B) is comparable to the four-roll structure resetting (B to C) with $t_{AB}/t_{BC} \approx 0.9$. While

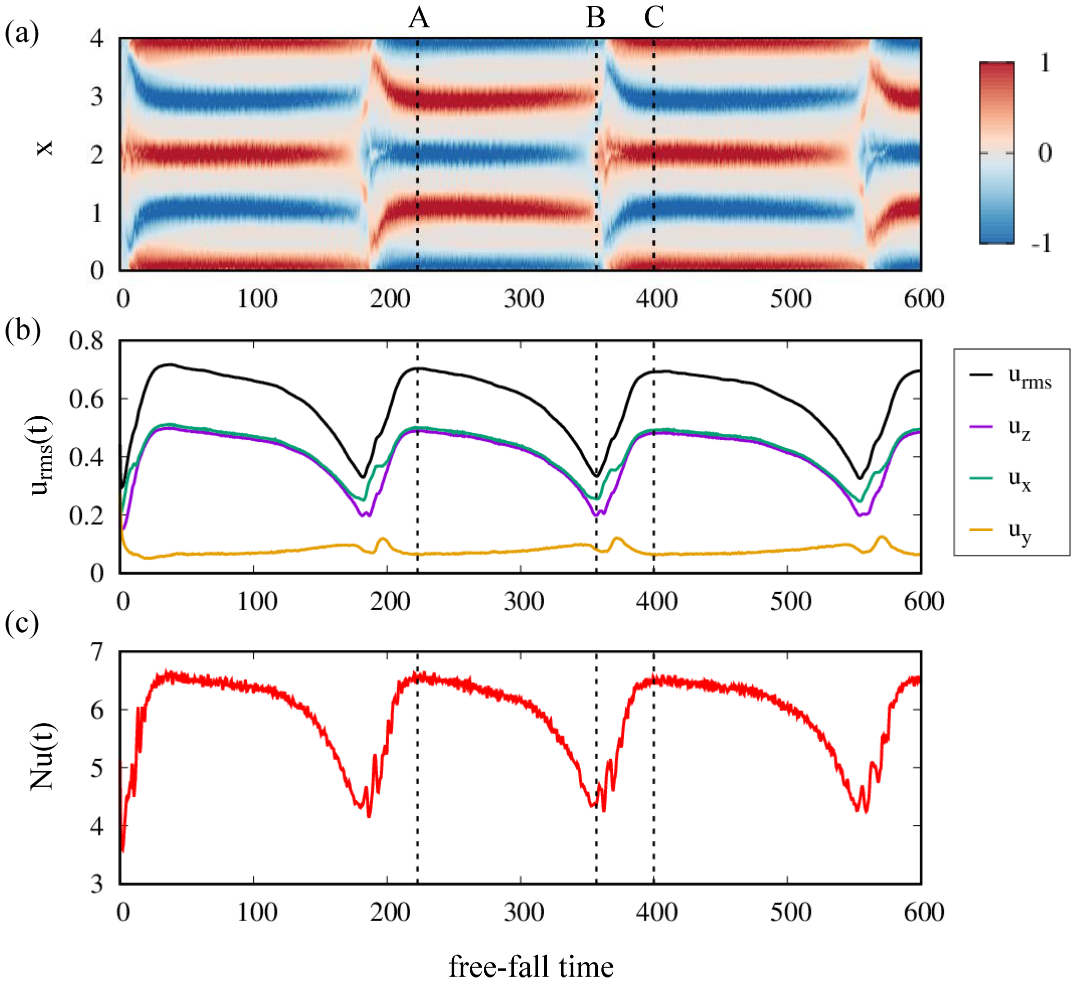

Figure 4.7: Similar figure to 4.2 but for $Ha = 200$, $Ra = 10^6$ and $\Gamma = 4:4:1$. $Ra/Ha^2 = 25$.

for $Ha = 200$, the breaking procedure is much slower than the resetting procedure with $t_{AB}/t_{BC} \approx 3.1$.

Figure 4.8 displays the results for $Ha = 300$ at $Pr = 0.025$, $Ra = 10^6$. A quasisteady and quasi 2D four-roll structure is established without reversals. This structure carries a high *r.m.s.* velocity of $u_{rms} \sim 0.70$, which is about 3.6 times that for $Ha = 0$. The u_y/u_{rms} are 0.06 which is 0.1 times that for $Ha = 0$. The Nusselt number is $Nu = 6.57$, about 1.32 times that for $Ha = 0$.

Similar to Yanagisawa *et al.* [2013] and Tasaka *et al.* [2016], we identified different convection pattern regimes which are in relation to the Rayleigh number Ra and the Hartmann number Ha. At low magnetic field ($Ha = 0$, 50), the flow regime is developed turbulence with fluctuating large-scale pattern without rolls. At strong magnetic field ($Ha = 300$), the flow regime is quasisteady 2D rolls pattern parallel to the magnetic field. In between, we observe weakly constrained rolls with fluctuations ($Ha = 100$) and the remarkable spontaneous flow reversals which is less regular at $Ha = 150$ and more regular at $Ha = 200$. Next, we will give a detailed investigation

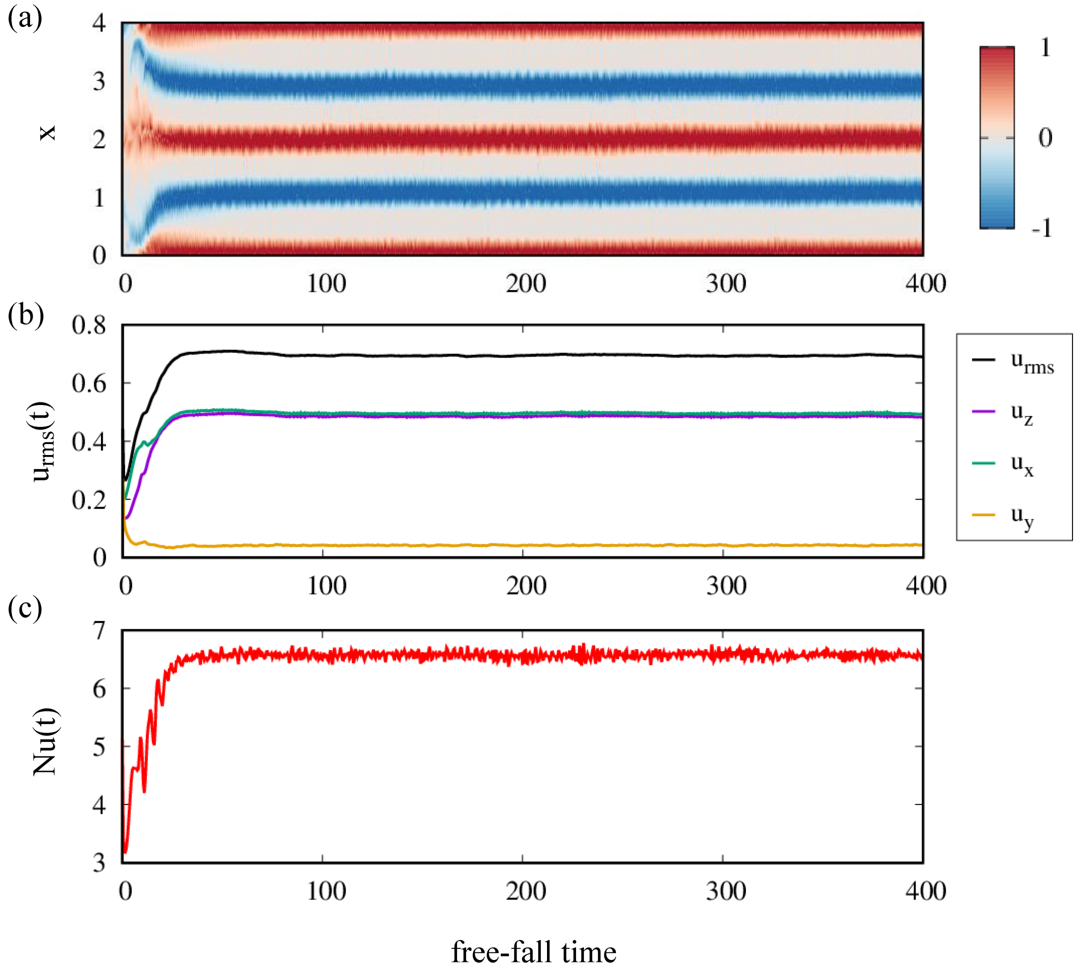

Figure 4.8: Similar figure to 4.2 but for $Ha = 300$, $Ra = 10^6$ and $\Gamma = 4:4:1$. $Ra/Ha^2 = 11.1$.

of flow reversals regimes in our geometry of $\Gamma = 4:4:1$ by considering the two cases with $Ha = 150$ and $Ha = 200$ at $Pr = 0.025$, $Ra = 10^6$ to show a deeper understanding of the spontaneous, repetitive flow reversals.

4.2.2 Flow reversals

In this subsection, we present detailed 3D process of one flow reversal procedure and analyze how the kinetic energy E_k and dissipation rates evolve when the reversals proceed. The kinetic energy is defined as

$$E_k(t) = \frac{1}{2} < u_x^2 + u_y^2 + u_z^2 >_V . \tag{4.4}$$

The viscous dissipation rate ε, the Joule dissipation rate ε_j and the thermal dissipation rate ε_T have been defined in equations (2.53), (2.54) and (2.55) respectively. In this section, these values are averaged throughout the volume of the vessel.

Figure 4.9 shows the results for $Ha = 150$, $Ra = 10^6$ and $\Gamma = 4:4:1$. In panel

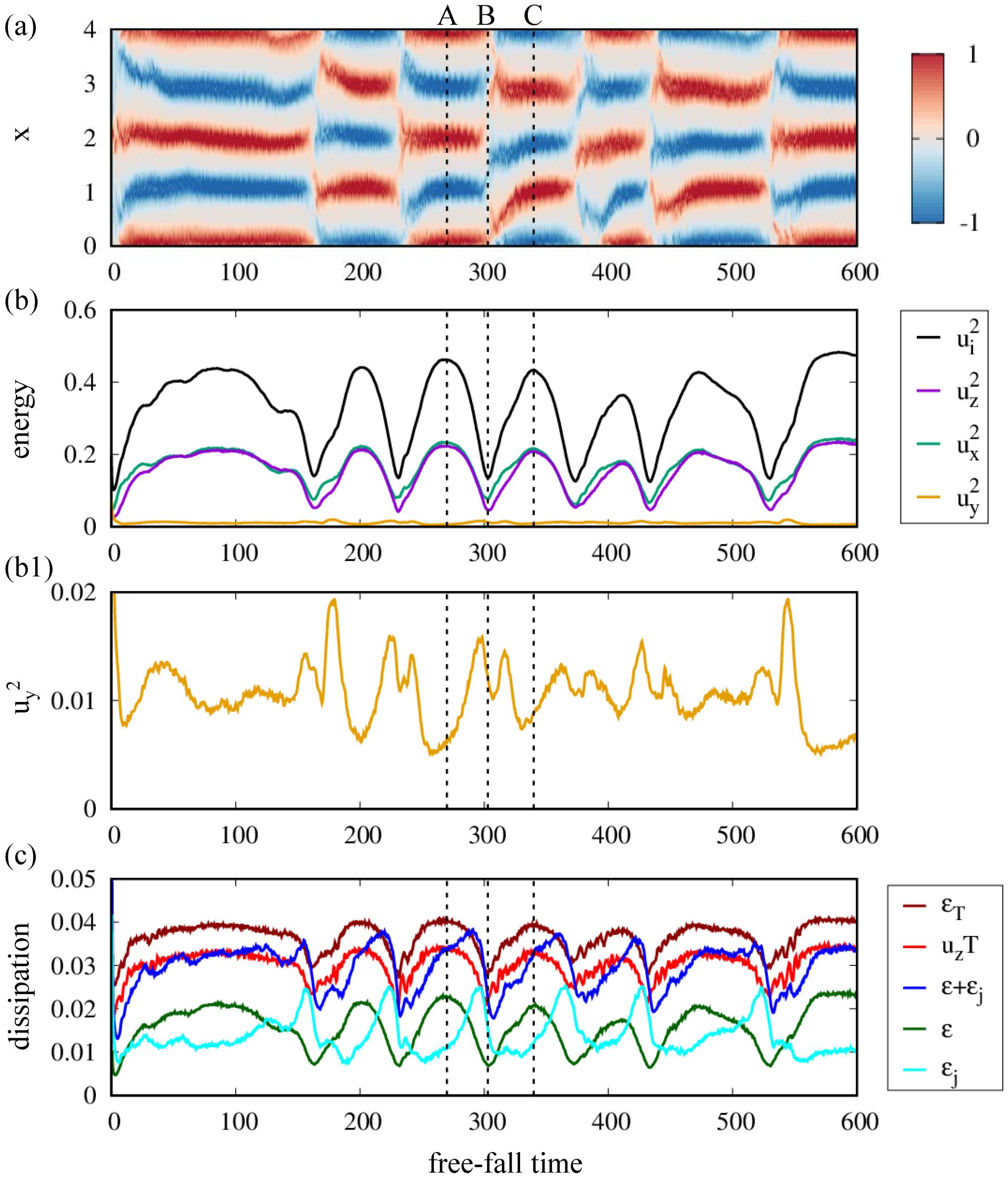

Figure 4.9: Results for $Ha = 150$, $Ra = 10^6$ and $\Gamma = 4 : 4 : 1$. (a) Time-space maps of vertical velocity same as to the figure 4.5(a). (b) Time various of kinetic energy. We show $u_i = 2E_k$ and its three components. y-component energy u_y^2 is zoomed in (b1). (c) Time various of the volume averaged thermal dissipation rate ε_T, heat transport u_zT and viscous dissipation rate ε in addition to the Joule dissipation rate ε_j.

(a), we recall the spatio-temporal velocity map as shown in figure 4.5(a). The corresponding time evolution of volume averaged energy is shown in figure 4.9(b), where we show $u_i^2 = 2E_k$. Its three components in different directions are shown as well in figure 4.9(b) with y–component energy u_y^2 zoomed in (b1). Figure 4.9(c) displays the time various of the volume averaged dissipation rates, including thermal dissipation

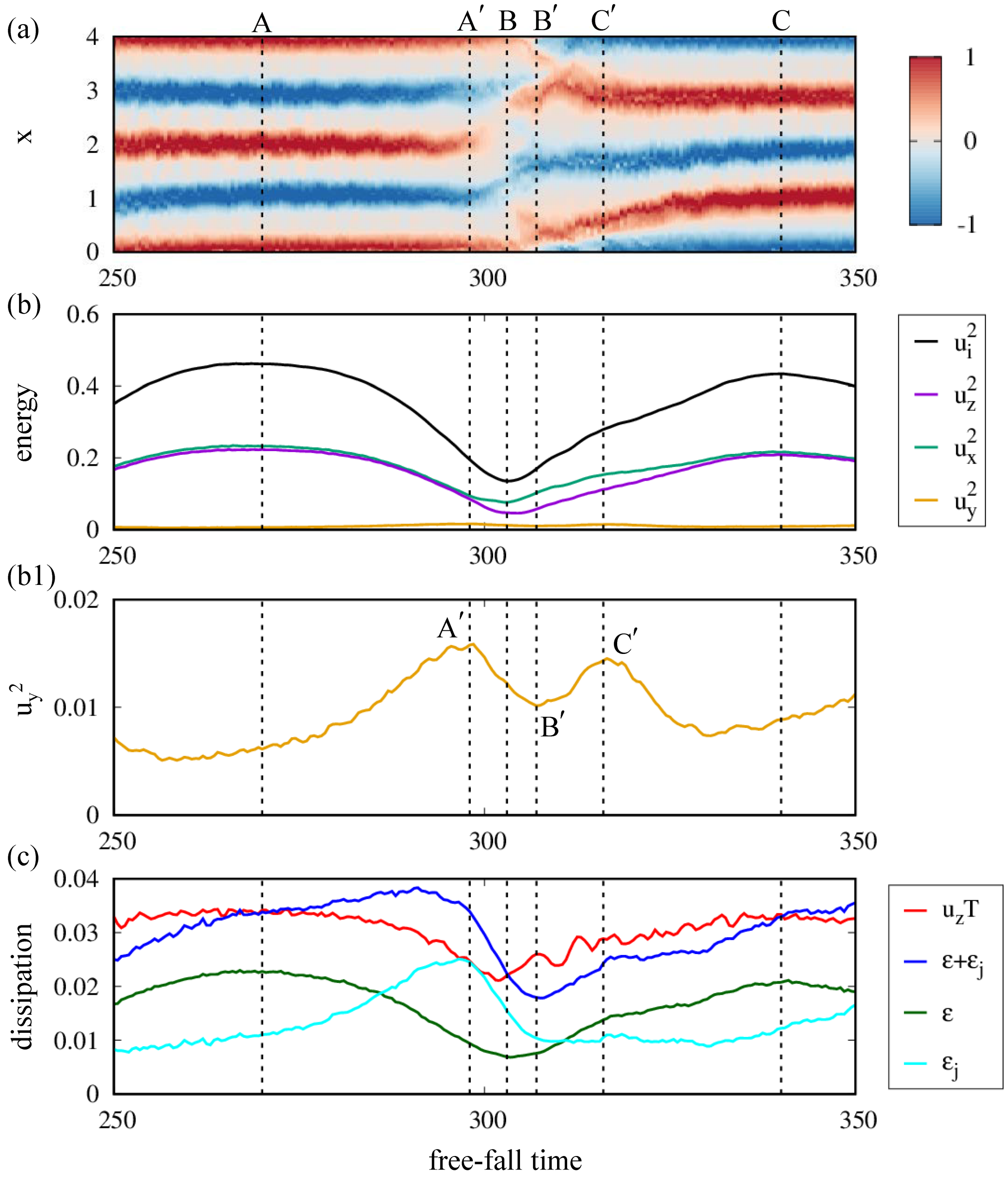

Figure 4.10: Enlarged time series of figure 4.9 with the time points used in figure 4.11 denoted by the vertical dashed lines.

rate $< \varepsilon_T >_V$, the viscous dissipation rate $< \varepsilon >_V$ in addition to the Joule dissipation rate $< \varepsilon_j >_V$. Besides, we will discuss the dissipation role of $< \varepsilon >_V + < \varepsilon_j >_V$ comparing to the source of potential energy $< u_z T >_V$ (see equation (2.52)). During the following discussion in this chapter, we omit $< \cdot >_V$.

The detailed flow reorganization progress during one reversal procedure from A to C is presented in figure 4.10 and 4.11. Six representative time points denoted by the vertical dashed lines in figure 4.10 will be used in the analysis. The dashed lines denoted by A, B, C are the same as in figure 4.5, which denote the positions of the first highest total energy (r.m.s. velocity), the lowest total energy (r.m.s. velocity) and the next new highest total energy (r.m.s. velocity) during one reversal procedure respectively. Apart from A, B, C, the other three instants of time denoted by A', B', C' are also presented. A' is the position with the first highest y–component energy u_y^2, C' the second highest u_y^2 and B' the lowest u_y^2 in between. Figure 4.11 displays 3D convection pattern for the six different instants. Patterns at time points A, B, C have been presented in figure 4.6. They are included here as well to show a complete reversal procedure.

At point A ($t = 270$), the pattern shows a quasi 2D four-roll structure aligned with the imposed magnetic field B_0. This structure has high values of total energy u_i^2 which is mainly contributed by the flow motion in x and z directions and has a low value of y–component energy u_y^2. The results are in a line with the former discuss on the r.m.s. velocity profiles. For the convenience of discussion, we number the rolls as 1, 2, 3, 4 as shown in figure 4.11. And the rotation directions of rolls from left to right are clockwise, counterclockwise, clockwise, counterclockwise respectively.

From A to A' , the shape and size of the rolls are changing with the back (frontal) half of the rolls No.1 and 2 expanding (shrinking) while No.3 and 4 shrinking (expanding). A new roll appears at left of the back half of the roll No.1, but we do not observe a new roll at the opposite corner. The procedure indicates an occurrence of a global horizontal circulation which bends the aligned rolls and has a style of skewed-varicose instability. During this procedure, u_y^2 is increasing and reaches a maximum at A' so as the Joule dissipation rate ε_j. Although the viscous dissipation rate ε is decreasing, $\varepsilon + \varepsilon_j$ is increasing which is larger than the source of the potential energy $u_z T$, resulting a decrease of total energy u_i^2.

From A' to B, with the rolls bending further and the new roll growing further, the back half of the roll No.4 as well as the frontal half of the roll No.1 disappear, and the rolls No.2 and No.3 are disconnected in the middle. The original four-roll structure is broken at point B as shown in figure 4.11. During A' to B, u_y^2 reduces as well as the Joule dissipation ε_j, but $\varepsilon + \varepsilon_j$ is still larger than $u_z T$, therefore, u_i^2 reduces further. At time point B, where $\varepsilon + \varepsilon_j$ decreases crossing $u_z T$, the total energy u_i^2 reaches its lowest value of one reversal procedure, which is about 0.3 times that at time A.

From B to C', the back half of the roll No.1 tends to connect with the frontal half of the roll No. 3 and the roll No.2 tends to connect with the roll No.4. In the mean time, the back half of the roll No.3 tends to grow along the right sidewall and the new roll tends to connect to the frontal half of the third roll. In between, u_y^2 reaches a lowest value at B', where the structure performs an aligned roll structure. Here, $\varepsilon + \varepsilon_j$ also reaches a lowest value. Since $\varepsilon+\varepsilon_j$ is smaller than u_zT, the energy u_i^2 is increasing.

At point C', a new four-roll structure is observed and this structure evolves to a quasi 2D four roll structure at time point C with the energy increases to a new high value, where $\varepsilon+\varepsilon_j$ increases crossing u_zT. However, the rotation directions of rolls in the new quasi 2D structure are counterclockwise, clockwise, counterclockwise and clockwise form left to right respectively, which are reversed comparing to the former ones at A.

Figures 4.12, 4.13 and 4.14 present reversal procedures for $Ha = 200$ with $Pr = 0.025$, $Ra = 10^6$. Similar analysis are presented here as for $Ha = 150$. The total energy u_i^2 has a high value when a quasi 2D four-roll structure establishes and has a low value in between as well as the u_zT, ε_T and ε. While the Joule dissipation rate ε_j has a small value in a four-roll like structure and a higher value in between. One also sees that the highest value of energy u_i^2 is established when $\varepsilon+\varepsilon_j$ increases crossing u_zT and the lowest value of u_i^2 is established when $\varepsilon+\varepsilon_j$ decreases crossing u_zT.

Six representative time points, denoted by the vertical dashed lines in figure 4.13, are also used to analyze the detailed 3D process of one flow reversal procedure from A to C. The dashed lines A, B, C denote the positions of the first highest total energy, the lowest total energy and the next new highest total energy during one reversal procedure respectively, while A', B', C' denote the position with the first highest y–component energy u_y^2, the lowest u_y^2 and the second highest u_y^2 in between respectively.

Similar reversal procedure can be identified as to the case for $Ha = 150$ as shown in figure 4.13 and 4.14. From A to A', the back half of the rolls are moving left while the frontal half of the rolls moving right as a result of the skewed-varicose instability with a global horizontal circulation. From A' to B, the original four-roll structure is broken with the back half of roll No.4 and frontal half of roll No. 1 disappearing. From B to B', the back half of roll No.1 (No.2) is connecting to the frontal half of roll No.3 (No.4). Two aligned rolls with larger aspect ratio emerge at B' accompanying with the residual structure of the back half of roll No.3 and the frontal half of roll No.2 at corners. From B' to C', the rolls at corners grow along the sidewalls to generate a new four-roll structure. This structure further evolves to a quasi 2D four-roll structure at time point C, with the rotation of each rolls being opposite that at A.

Different to the case with $Ha = 150$, the reversals occur at very regular intervals with a certain time period of $\sim$ 180 free-fall time units, which is significantly longer than the case of $Ha = 150$. This is because the four-roll structure is more stable at a higher magnetic field and the growth rate of the skewed-varicose instability is much slower. The bending procedure from $A(t = 223)$ to $A'(t = 350)$ lasts for 127 free-fall time units at $Ha = 200$, which is about 4.5 times that of $Ha = 150$. And we do not observe a new roll structure generated at any corner during the whole reversal procedure. The period from A' to C' is comparable for the two cases, which lasts about 20 time units, indicating that the breaking and reconnecting during the reversal is very fast. For $Ha = 200$, $t_{A'C'}/t_{AC} \approx 0.12$.

We have presented the reversal process in detail by the visualization of the 3D structures during one circle. The occurrence of the horizontal circulation plays an important role to driven the reversals. Next we present more information about the horizontal circulation during different reversal procedures. Figure 4.15 shows the spatiotemporal distributions of vertical velocity at horizontal mid-plane ($z = 0$) along $y = 3.5$ in (a) and along $y = 0.5$ in (b). We detect 6 reversal cycles during the entire run at $Ha = 150$, $Ra = 10^6$. We observe similar procedure as shown in figure 4.11 for each reversal cycle. Particularly, the creation of a new roll in one corner and the skewed-varicose instability with global horizontal circulation are observed during each reversal procedure. The directions of the global horizontal circulation are reflected by the time-space velocity maps at two positions. Except the first reversal cycle, the directions of the horizontal circulation during the other five cycles are the same, which are clockwise as shown in figure 4.15(c). Figure 4.16 shows the results for $Ha = 200$. In this case, we detect 3 reversal cycles during the entire run. Similar reversal procedures are observed as shown in figure 4.14. However, the directions of the horizontal circulation are reversed during two consecutive reversal cycles. As shown in 4.16(c), during the first reversal the horizontal circulation is counterclockwise, then it changes to clockwise during the next reversal and becomes counterclockwise again during the third one.

4.2.3 Integral characteristics

The global transport of heat and momentum is summarized in table 4.2 as the integral Nusselt number Nu and the Reynolds number Re. The horizontal magnetic field strengthens the heat as well as the momentum transport in the system by reorganizing the flow structures as roll like structure aligned with the magnetic field. Since the quasi 2D roll like structure ensures a direct heat transfer between bottom and top walls, the uniform bulk central region of the convection is extended and the thermal boundary layers are thinner as the magnetic field increasing.

4.2.4 Summary and discussion

We have studied three-dimensional turbulent magnetoconvection in a closed box with a square horizontal cross section and an aspect ratio of $\Gamma = 4 : 4 : 1$ under influence of an external horizontal magnetic field. We identified different convection

Ha	Ra/Ha^2	Nu (Nu^A, Nu^B)	Re (Re^A, Re^B)	δ_T	δ_{Ha} ($1/Ha$)	Runtime
0	∞	4.98	2793	0.101	0.011	400
50	400	4.94	2626	0.101	0.011 (0.02)	400
100	100	5.06	2753	0.099	0.009 (0.01)	400
150	44.4	5.75 (6.41, 4.48)	3614 (2917, 835)	0.087	0.007 (0.007)	400
200	25	5.93 (6.57, 4.35)	3806 (3126, 700)	0.084	0.006 (0.005)	400
300	11.1	6.57	4394	0.076	0.004 (0.003)	350

Table 4.2: Integral characteristics of convection under influence of a horizontal magnetic field in a square box with aspect ratio $\Gamma = 4:4:1$. The Prandtl number is fixed to $Pr = 0.025$, the Rayleigh number to $Ra = 10^6$. The Hartmann number Ha, the ratio Ra/Ha^2, the Nusselt number Nu, the Reynolds number Re are given. For the two cases with flow reversals, we also given two instantaneous values denoted by A and B in figure 4.5 and 4.7. We also list thermal boundary layer thickness at top and bottom walls and the viscous boundary layer thickness by a slop method at Hartmann walls. The thickness calculated by $1/Ha$ is shown in parenthesis. Finally, the total runtime used for the integral is given in free fall time units, $T_\mathrm{f} = H/U_\mathrm{f}$.

pattern regimes for different strengths of the magnetic field. At low magnetic field, the flow regime is developed turbulence with fluctuating large-scale pattern without rolls. At sufficient strong magnetic field, the flow regime is quasisteady 2D four-roll pattern parallel to the magnetic field. In between, we observe another two regimes– weakly constrained rolls with fluctuations and spontaneous flow reversals. Similar results have been reported by Yanagisawa *et al.* [2013] and Tasaka *et al.* [2016], which studied convection pattern in liquid gallium under an imposed horizontal magnetic field experimentally in a square vessel with aspect ratio 5 : 5 : 1. Our present simulations reproduce the results in a square vessel with aspect ratio 4 : 4 : 1 by considering a Rayleigh number up to 10^6 and Hartmann number Ha up to $Ha = 300$.

The most remarkable regime that of flow reversals in which four rolls periodically change the direction of their circulation has been analyzed in detail. Similar to Yanagisawa *et al.* [2013, 2015] and Tasaka *et al.* [2016], the key regime of the flow reversals is the interaction of between the aligned convection rolls and global horizontal circulation caused by the skewed-varicose instability. The process can be generally described as bending (expanding and shrinking of the rolls), breakdown and reconnecting of the convection rolls. However, the detailed procedure may be different for the cases with different strength of magnetic field. For the specific DNS run with $Ha = 150$, we observed a creation of new roll structure at one corner, while for the run with $Ha = 200$, no new roll structure is observed. The direction of horizontal circulation which drives the bending of the aligned rolls is unchanged for the case with $Ha = 150$, while that for $Ha = 200$ reverses during two consecutive reversal cycles.

The regime shows an interesting similarity to the large-scale temporal intermittency in the channel flow with spanwise magnetic field which is found at intermediate values of Ha [Boeck *et al.*, 2008]. In both cases, the flow experiences long periods of nearly steady laminar behavior interrupted by short turbulent bursts. The magnetic field is not strong enough to suppress three-dimensional secondary instabilities and transition to turbulence. However the magnetic field is sufficient to suppress turbulence after just a short burst and return the flow back to nearly laminar base state. The Joule dissipation rate has a low value in laminar state and the the growth of secondary instability can resume. The result is the flow evolution in apparently endless and nearly identical cycles, each consisting of growth of instability, turbulent burst and return to the quasi laminar state.

Increase of Ha within the range of reversal existence reduces the strength of turbulent burst and prolongs the reversal circle, primarily via extending the stability growing stage. When the magnetic field is strong enough, it prevents the development of the secondary skewed-varicose instability and the flow shows a quasisteady 2D four-roll structure aligned with the magnetic field. The aspect ratio per roll is about $L_x : L_y : H = 1 : 4 : 1$.

The quasi 2D roll like structure ensures a direct heat transfer between bottom and top walls, extending the uniform bulk central region of the convection and thinning the thermal boundary layers, causing an increase of heat transfer coefficient. We have conducted a test run with much higher Hartmann number of $Ha = 500$ and find that the global heat and momentum transport decreases. A further increase of the Hartmann number will turn the Hartmann layer extremely thinner and their appropriate resolution will make the DNS very demanding. This is however can be done in the future.

4.3 Results in a long rectangular box with aspect ratio $\Gamma = 1 : 4 : 1$

As we discussed in the previous section, a horizontal magnetic field tends to reorganize the convection flow into roll-like structure aligned with the magnetic field. The aspect ratio per roll is about $L_x : L_y : H = 1 : 4 : 1$. In this section, we narrow the geometry to an aspect ratio of $\Gamma = 1 : 4 : 1$ and keep the other input parameters the same as the former one in a square box that the magnetic field B_0 is homogeneously imposed in y direction which is parallel to the longest side walls, the Prandtl number is fixed to $Pr = 0.025$, Rayleigh number to $Ra = 10^6$ and the Hartmann number Ha varies from 0 to 300. The parameters are summarized in table 4.1 as series 2. For each case, the fully developed Rayleigh-Bénard convection at zero magnetic field is used as initial state.

Figure 4.17 displays the time evolution of energy, $u_i = 2E_k$ at different amplitudes of a horizontal magnetic field and figure 4.18 shows snapshots of the vertical velocity field on the middle horizontal plane at $t = 200T_f$. Without magnetic field ($Ha = 0$), flow pattern in the long rectangular box shows typical oscillating rolls with axes normal to the longest side walls of the box [Yanagisawa *et al.*, 2010*b*]. A low magnetic field ($Ha = 50$) has no obvious effect on the four-roll pattern, but decreases the oscillation of the rolls. With a sufficiently strong magnetic field ($Ha \geq 100$), the flow pattern is organized to a quasisteady one-roll structure aligned with the magnetic field. Interestingly, at moderated magnetic field especially for $Ha = 150$, we observe a long transition period before the one-roll structure established.

Figure 4.19 summarizes the time-dependent results for $Ha = 150$, $Ra = 10^6$ and $\Gamma = 1:4:1$ and figure 4.20 shows 3D flow structures at five instants of time denoted by the vertical lines in figure 4.19. The flow pattern shows a twisted roll structure during the transition period as shown in the top row of figure 4.20. The structure consists of two half-vessel-length rolls which have different orientations, i.e. left half roll rotates clockwise while the right half roll rotates counterclockwise. The two rolls are aligned with the magnetic field and are quasi 2D except the zone where they connect. We may call the connection as a ”knot”. The transition structure is set soon after the magnetic field imposed and then driven slowly by a motion along the magnetic field B_0 with the knot moving from center to one side of the box until a quasi 2D one-roll structure is settled.

During the transition period of $Ha = 150$, the flow has an total energy of $u_i^2 \approx 0.15$, which is mostly contributed by the flow motion in x and z direction that $u_x^2 \approx u_z^2 \approx 0.07$ and $u_y^2 \approx 0.007$. The results reflect that even the structure is twisted in the middle but still has a high 2D property. During this period, the viscous dissipation rate ε is comparable with the Joule dissipation rate ε_j, and $\varepsilon + \varepsilon_j$ is comparable with the potential energy u_zT. After the knot arriving at the end of the box (marked by C), the y direction motion begins to decrease obviously, then the Joule dissipation ε_j decreases, resulting that $\varepsilon + \varepsilon_j$ is smaller than u_zT, therefore, the energy increases. At point E ($t = 251$),where a quasi 2D one-roll structure is settled, the $\varepsilon + \varepsilon_j$ evolves to comparable with u_zT and the energy increases to a high value of 0.34 which is about 2.3 times higher than the transition state. The Nusselt number during the transition state is about 5.5 which is comparable to that of the final one-roll state. The Reynolds number during the transition state is about 2779, while for the final one-roll state, it is about 3678 which is 1.3 times higher.

The transition period lasts for about $200T_f$ at $Ha = 150$. Similar transition phenomenon is also detected for the case with $Ha = 100$ and $Ha = 200$, which lasts about

$100T_f$ for $Ha = 100$ and $50T_f$ for $Ha = 200$ respectively. The phenomenon is a result of the competition between buoyancy force and Lorentz force. But it is not clear yet why the transition period is not monotonously increasing with the magnetic field.

In this section, we have studied magnetoconvection in a closed long rectangular box with an external horizontal magnetic field parallel to the longest side walls. Different convection patterns are detected at different strengths of the magnetic field. At low magnetic field, the flow remains oscillating four-short-roll structure with axes normal to the longest side walls. For sufficiently strong magnetic field, the flow pattern shows one-long-roll structure parallel to the longest side walls, i.e. aligned the magnetic field. Flow reversals are not observed in this configuration. However, at moderate magnetic field, we observe a long transition period before the one-roll structure established. The flow pattern during the transition period shows an interesting twist roll structure which consists two half-vessel-length rolls with different orientations.

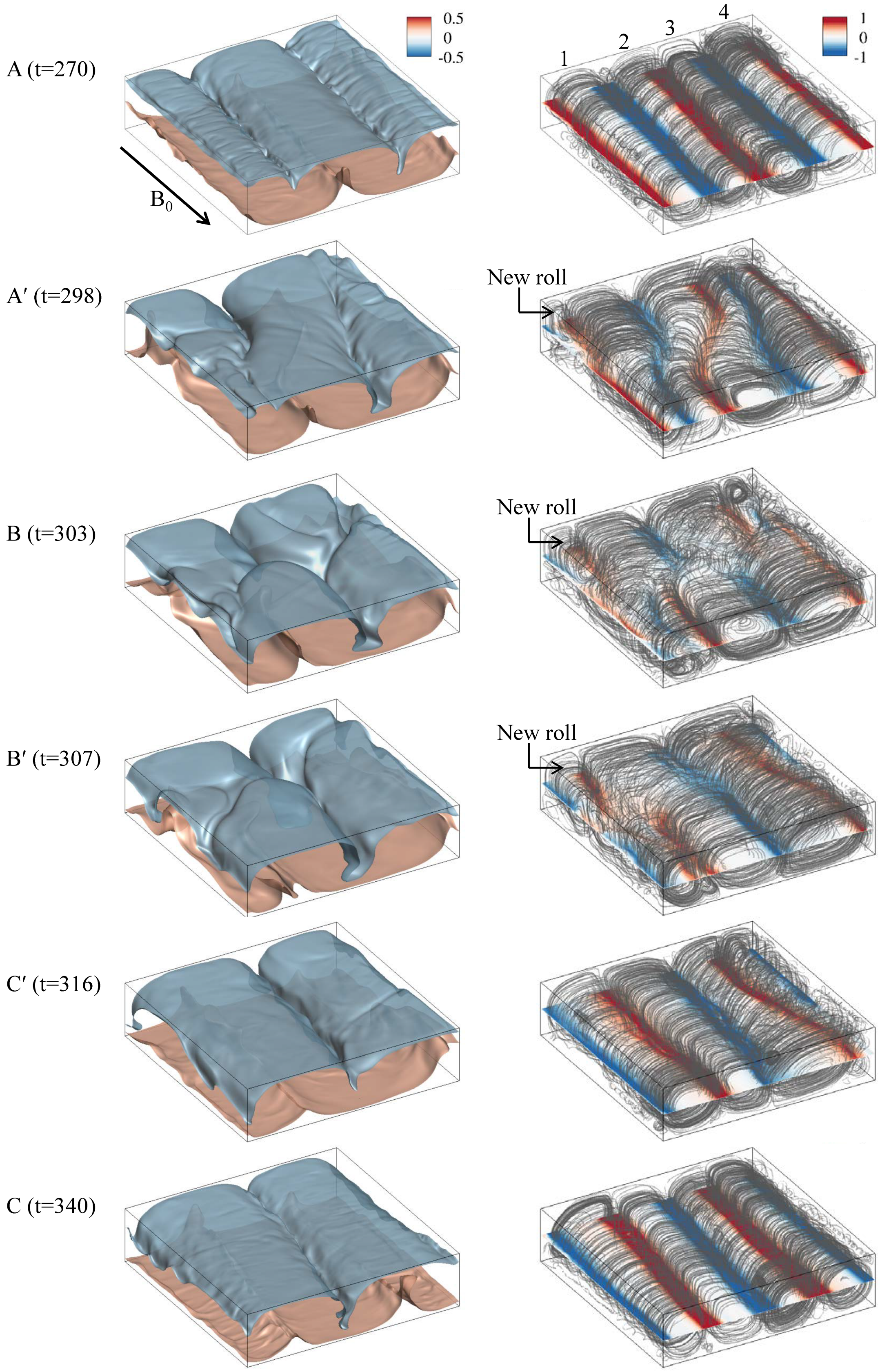

Figure 4.11: Flow evolution during one reversal procedure with $Ha = 150$, $Ra = 10^6$ and $\Gamma = 4 : 4 : 1$. Six snapshots are shown denoted by the six vertical dashed lines in figure 4.10. Left column shows two isosurfaces of temperature field ($T = \pm 0.25$). Right column shows streamlines of 3D velocity field together with the horizontal distribution of vertical velocity u_z at mid-plane ($z = 0$) with red for upwards motion and blue for downwards motion.

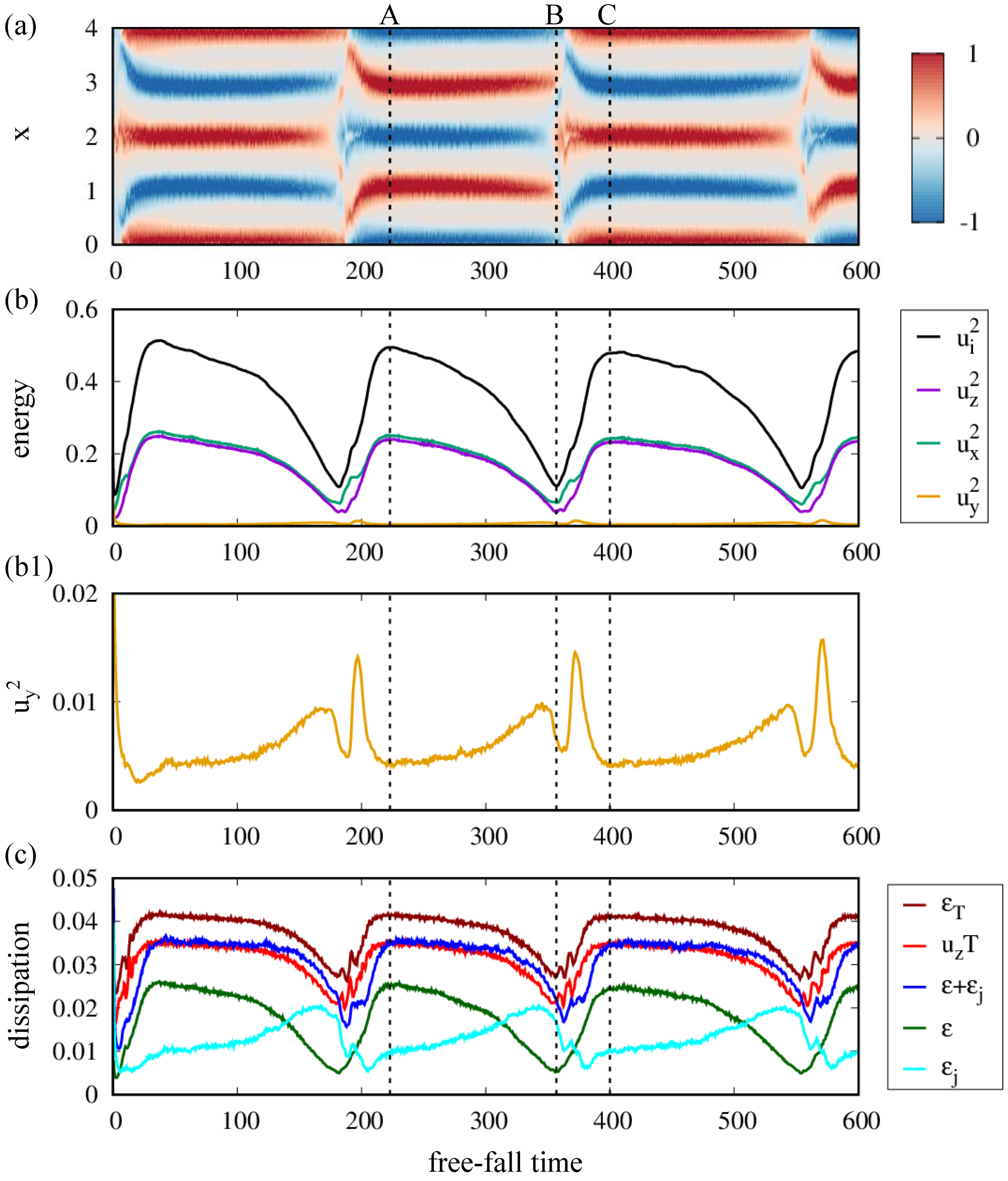

Figure 4.12: Results for $Ha = 200$, $Ra = 10^6$ and $\Gamma = 4:4:1$. (a) Time-space maps of vertical velocity same as to the figure 4.7(a). (b) Time various of kinetic energy. We show $u_i^2 = 2E_k$ and its three components. y-component energy u_y^2 is zoomed in (b1). (c) Time various of the volume averaged thermal dissipation rate ε_T, heat transport u_zT and viscous dissipation rate ε in addition to the Joule dissipation rate ε_j.

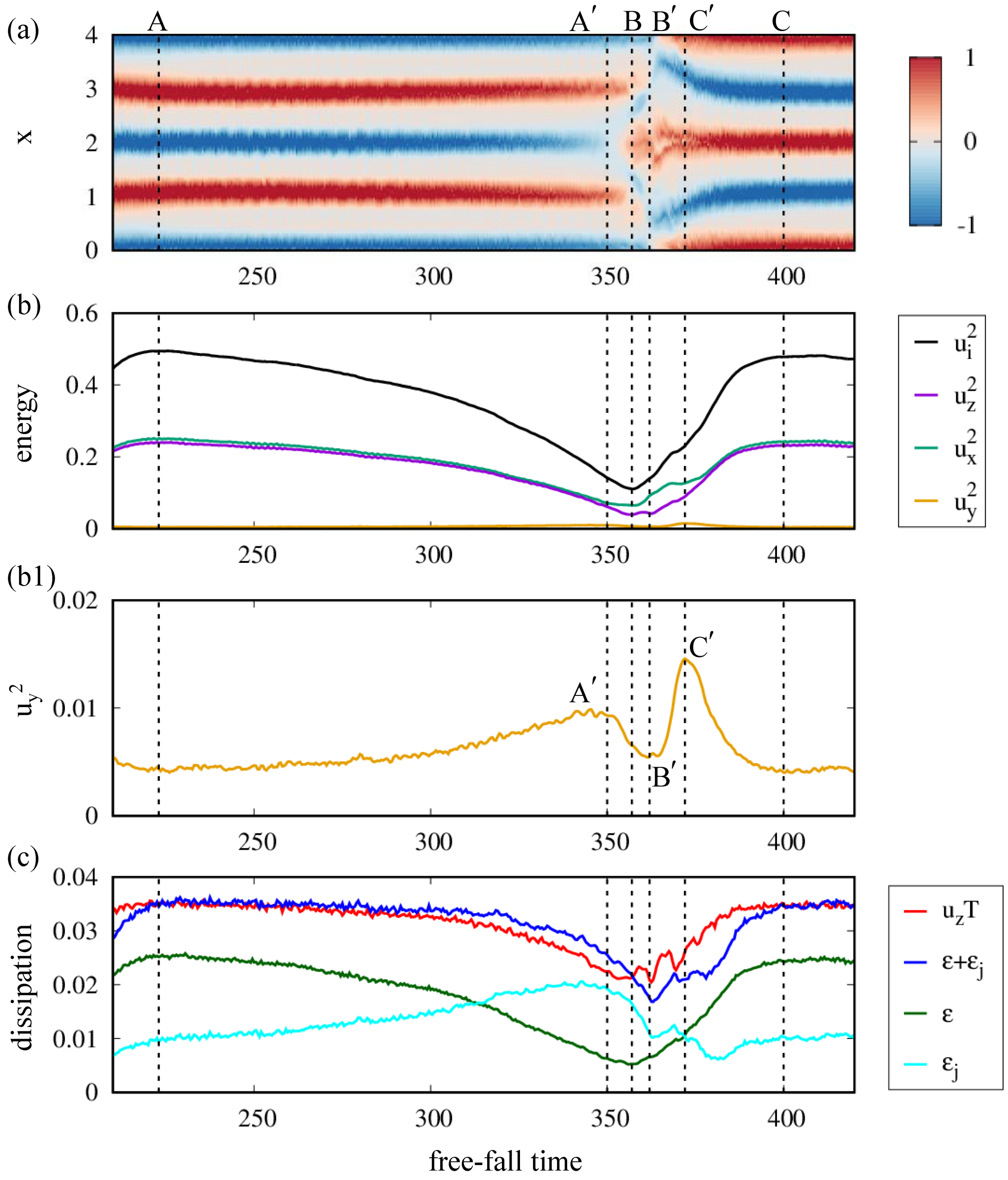

Figure 4.13: Enlarged time series of figure 4.12 with the time points used in figure 4.14 denoted by the vertical dashed lines.

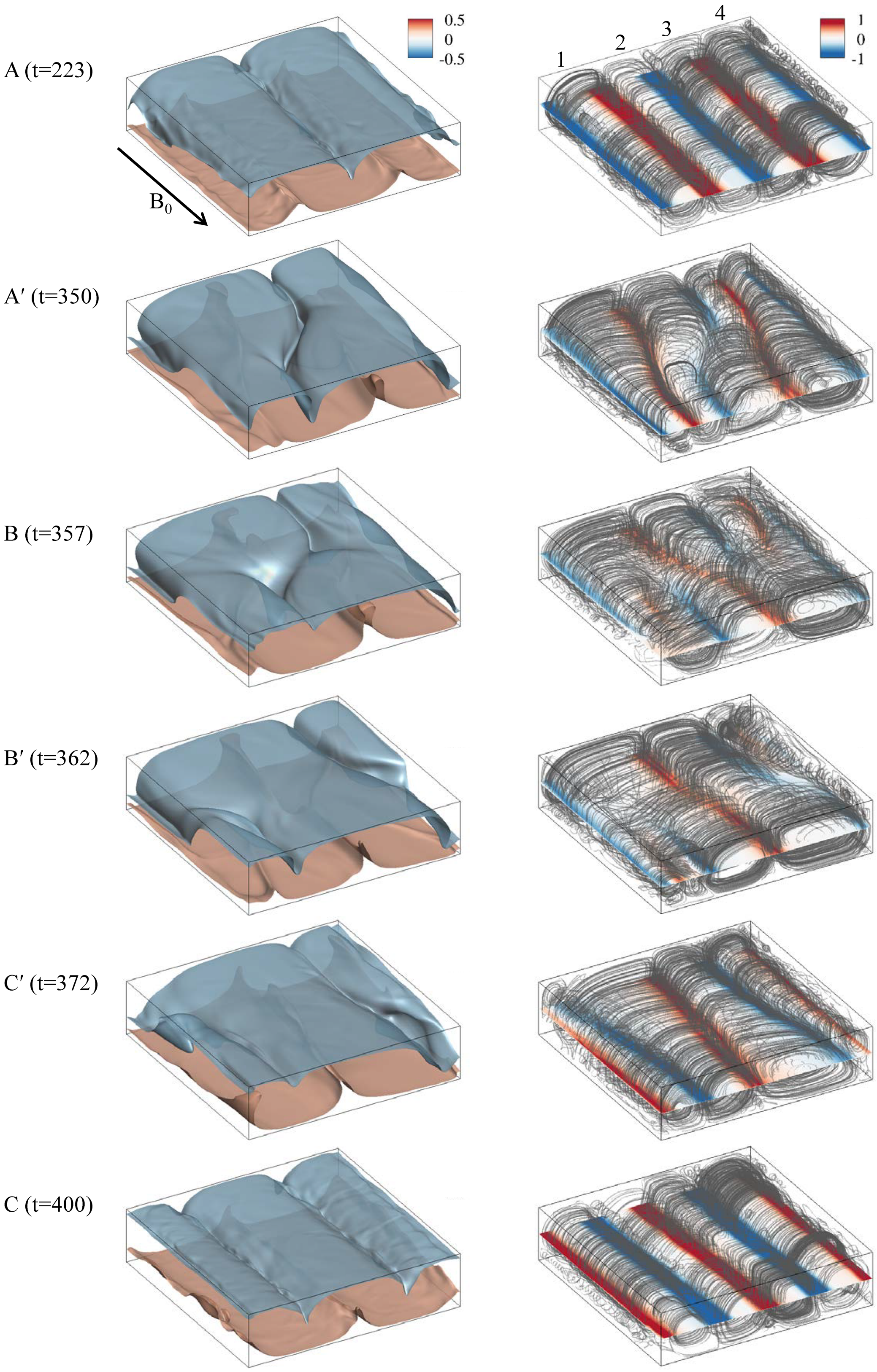

Figure 4.14: Flow evolution during one reversal procedure with $Ha = 200$, $Ra = 10^6$ and $\Gamma = 4:4:1$. Six snapshots are shown denoted by the six vertical dashed lines in figure 4.13. Left column shows two isosurfaces of temperature field ($T = \pm 0.25$). Right column shows streamlines of 3D velocity field together with the horizontal distribution of vertical velocity u_z at mid-plane ($z = 0$) with red for upwards motion and blue for downwards motion.

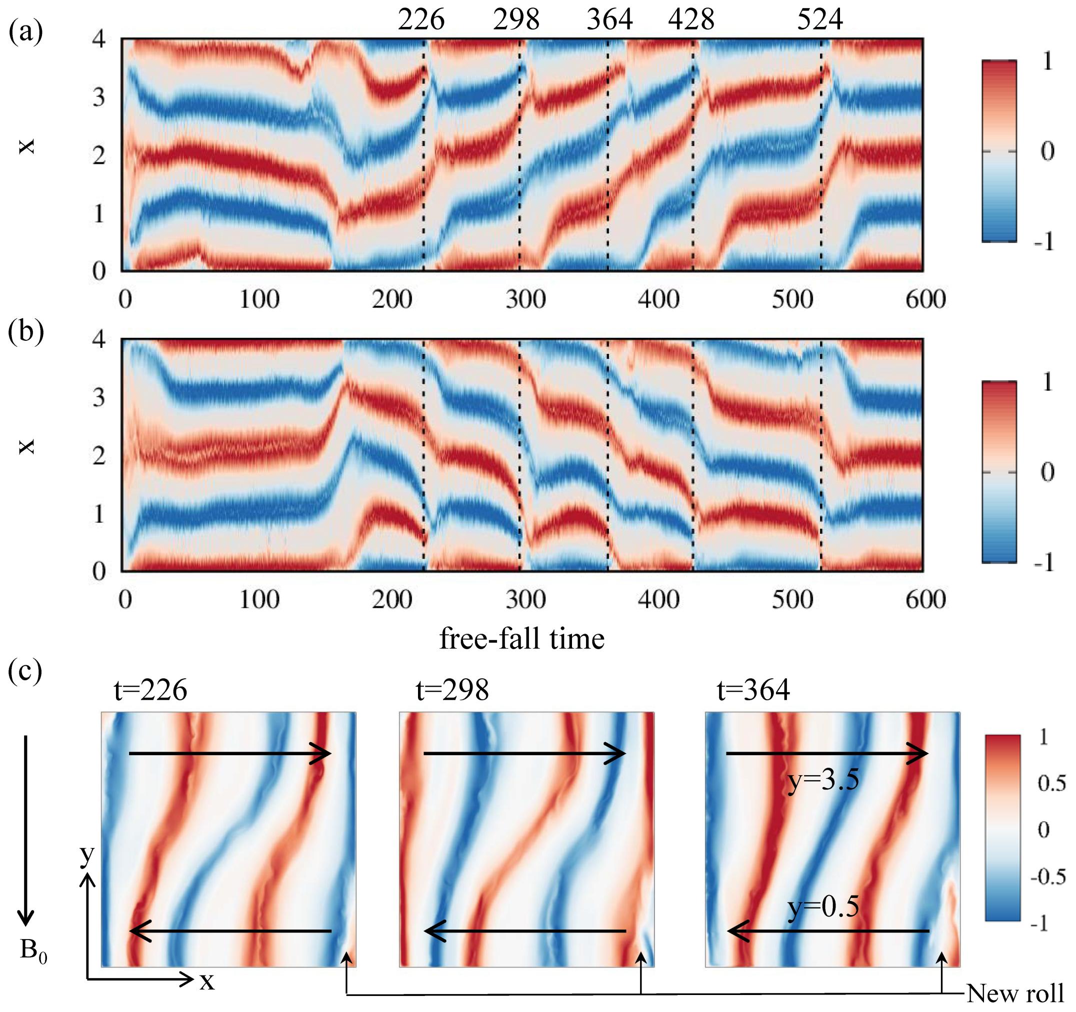

Figure 4.15: Results for $Ha = 150$, $Ra = 10^6$ and $\Gamma = 4:4:1$. Time-space maps of vertical velocity u_z at horizontal mid-plane ($z = 0$) (a) along $y = 3.5$ and (b) along $y = 0.5$. (c) Expected global horizontal circulations that driven the flow reversals. Snapshots of horizontal cross sections at mid-plane ($z = 0$) of instantaneous vertical velocity field at three different time instants are shown.

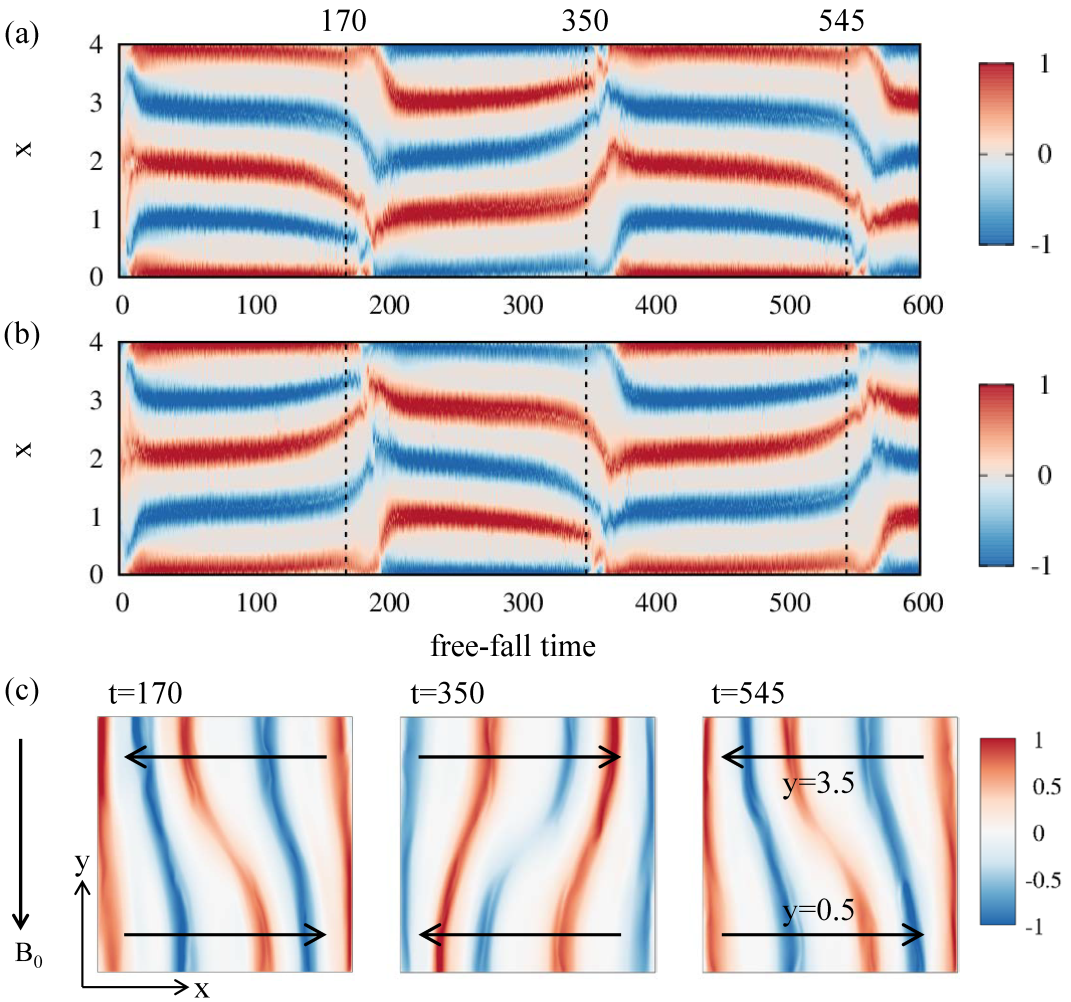

Figure 4.16: Similar figure to 4.15 but for $Ha = 200$, $Ra = 10^6$ and $\Gamma = 4:4:1$. Time-space maps of vertical velocity u_z at horizontal mid-plane ($z = 0$) (a) along $y = 3.5$ and (b) along $y = 0.5$. (c) Expected global horizontal circulations that driven the flow reversals.

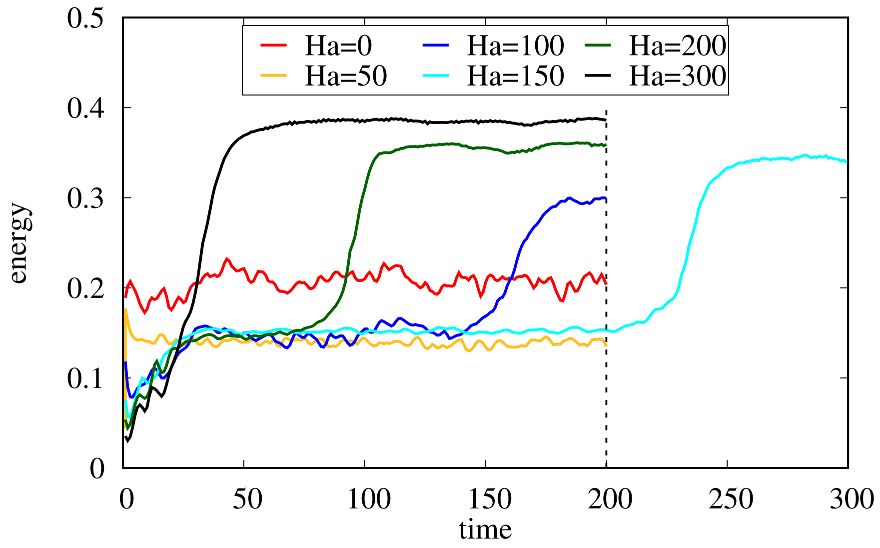

Figure 4.17: Time variations for kinetic energy (Eq. 4.4). We show $2E_k$ for six Ha values with $Pr = 0.025$, $Ra = 10^6$ and $\Gamma = 1:4:1$.

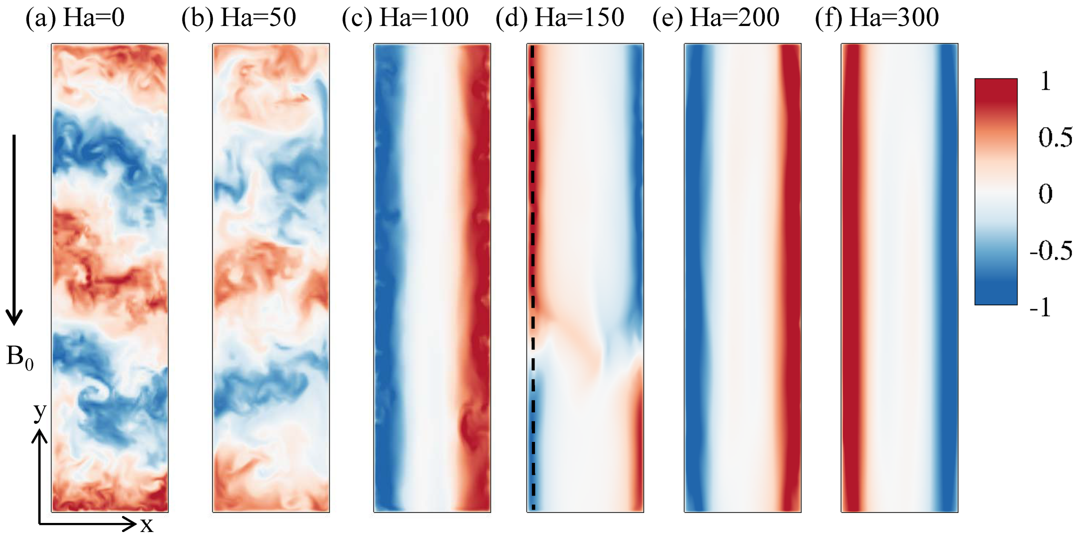

Figure 4.18: Convection pattern under effects of a horizontal magnetic field in y direction for six Ha values with $Pr = 0.025$, $Ra = 10^6$ and $\Gamma = 1:4:1$. Horizontal cross sections at mid-plane ($z = 0$) of instantaneous vertical velocity field u_z at $t = 200$ are shown. Blue indicates downwards flow and red indicates upwards flow.

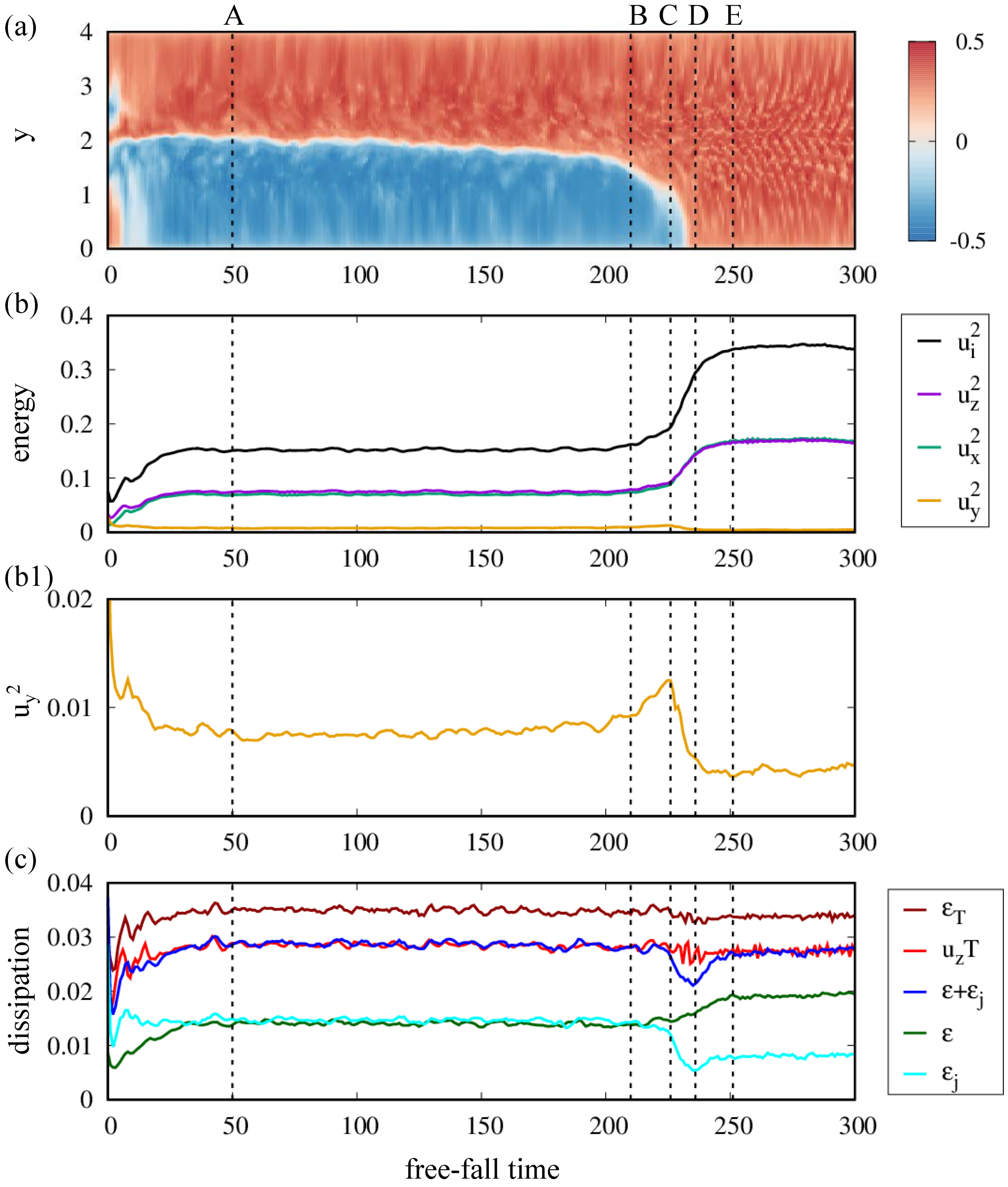

Figure 4.19: Time dependent results for $Ha = 150$, $Ra = 10^6$ and $\Gamma = 1:4:1$. (a) Time-space maps of vertical velocity u_z at horizontal mid-plane ($z = 0$) along the dashed line in figure 4.18(d). (b) Time various of kinetic energy (Eq. 4.4). We show $u_i^2 = 2E_k$ and its three components. y-component energy u_y^2 is zoomed in (b1). (c) Time various of the volume averaged thermal dissipation rate ε_T, heat transport u_zT and viscous dissipation rate ε in addition to the Joule dissipation rate ε_j.

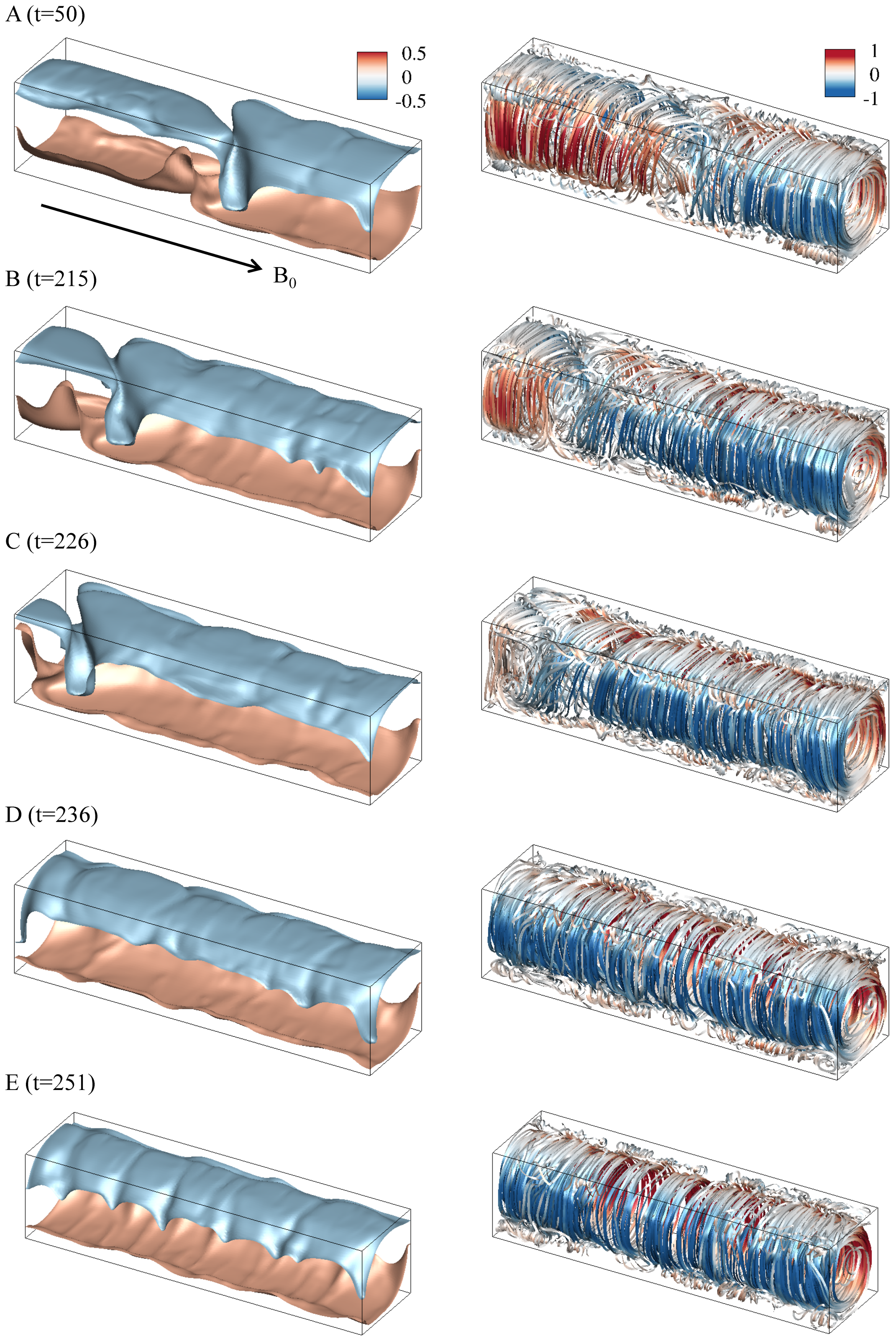

Figure 4.20: 3D structures of convection flow for $Ha = 150$, $Ra = 10^6$ and $\Gamma = 1:4:1$. Five snapshots are shown for different instants in time denoted by the five vertical dashed lines in figure 4.19. Left column shows two isosurfaces of temperature field ($T = \pm 0.25$). Right column shows streamlines of 3D velocity field with the lines colored by vertical velocity u_z. Red is for upwards motion and blue for downwards motion.

Chapter 5

Rayleigh-Bénard convection under effects of a vertical magnetic field

5.1 Overview and problem setup

This chapter presents the study of turbulent Rayleigh-Bénard convection in liquid metal under effects of an externally applied vertical magnetic field. As mentioned in chapter 1, a sufficiently strong vertical magnetic field will suppress the onset of Rayleigh-Bénard convection with the Chandrasekhar linear stability limit reached at $Ha_c \approx \sqrt{Ra}/\pi$ (see equation (1.1)), while laterally confined geometries tend to relax this constraint with a form of wall-attached convection present for $Ha > Ha_c$ [Busse, 2008; Houchens *et al.*, 2002]. In this chapter, we show how the convective turbulence structures and the heat and momentum transport are affected when the vertical magnetic field strength is increased towards and beyond the Chandrasekhar limit by different series of three-dimensional high-resolution DNS.

Main parameters used in the study are summarized in table 5.1. They comprise:

Series 1: $\Gamma = 1:1:1$, $Pr = 0.025$, $Ra = 10^6$, $0 \leq Ha \leq 600$. The runs start with a zero state from very beginning, triggered by a weak random noise.

Series 2: $\Gamma = 1:1:1$, $Pr = 0.025$, $Ra = 10^6$, $0 \leq Ha \leq 600$. The runs start with fully developed turbulent state at $Ha = 0$.

Series 3: $\Gamma = 4:4:1$, $Pr = 0.025$, $Ra = 10^6$, $0 \leq Ha \leq 300$. The runs start with fully developed turbulent state at $Ha = 0$.

Series 4: $\Gamma = 4:4:1$, $Pr = 0.025$, $Ra = 10^7$, $0 \leq Ha \leq 2000$. The runs start with fully developed turbulent state at $Ha = 0$.

We consider turbulent convection in liquid metal at a fixed Prandtl number of $Pr = 0.025$ in two different closed cells with either a small aspect ratio of $\Gamma = 1:1:1$, i.e. a cubic cell, or with a large aspect ratio of $\Gamma = 4:4:1$, i.e. a large square cell.

In the cases with $\Gamma = 1:1:1$, the Rayleigh number is fixed to $Ra = 10^6$. With the chosen Ra and Pr, the flow is already turbulent in the absence of a magnetic field. The Hartmann numbers are increased from $Ha = 0$ crossing the Chandrasekhar limit up to a value of $Ha \approx 2Ha_c$ with $Ha_c \approx 318$ for $Ra = 10^6$. For each case of $Ha \neq 0$, we have performed simulations with two different initial states either a zero state from very beginning or a fully developed turbulent state at $Ha = 0$. In the cases with large aspect ratio, two series of data sets are considered. First, the Rayleigh number is fixed to $Ra = 10^6$ and the Hartmann number is increased from $Ha = 0$ to $Ha = 300$ with a turbulent state at $Ha = 0$ as initial state. These runs are mainly used to explain some phenomena which are observed in a small aspect ratio. Second, the main focus of this work, the Rayleigh number is fixed to $Ra = 10^7$, with which the flow is highly turbulent in the absence of a magnetic field. The Hartmann number is increased up to $Ha = 2000$, which is also twice of the Chandrasekhar threshold Ha_c approximately with $Ha_c \approx 1007$ for $Ra = 10^7$. These runs start also from the fully turbulent state in the absence of magnetic field. The grid resolution used in each simulation with grid points inside the viscous (equation (2.46)) and Hartmann boundary layers (equation (2.47)) is listed in table 5.1. We have conducted the numerical simulations in a standard way. All simulations are computed starting from their initial conditions until the flow reaches a fully developed state. After that, the flow is computed for a period no shorter than a certain free fall time units, during which the time-averaged quantities are accumulated. The total runtime used in the integral analysis for different runs is summarized in table 5.1. The (turbulent) heat transfer measured by the Nusselt number (equation (2.43)) and the (turbulent) momentum transfer quantified by the Reynolds number (equation (2.44)) are summarized in table 5.1. A detailed report of the heat and momentum transfer regime as well as the determining mechanisms and features of the flow will be given in this chapter.

This chapter is organized as follows: section 5.2 presents the main results with a moderate Rayleigh number of $Ra = 10^6$ in a cubic box with $\Gamma = 1:1:1$. Part of the results have been published in Liu *et al.* [2015]. In section 5.3, we present the results with high Rayleigh number of $Ra = 10^7$ in a square box with $\Gamma = 4:4:1$. Part of the results have been published in Liu *et al.* [2018]. An extension of Grossmann and Lohse theory to magnetoconvection which is based on our simulation data will be introduced in section 5.4. The results have been published in Zürner *et al.* [2016].

Run	Γ	Ra	Ha	Ra/Ra_c	$N_x \times N_y \times N_z$	A_z	Nu	Re	N_{BL}	Runtime
series 1: start with a zero state from very beginning, triggered by a weak random noise										
1-1	$1:1:1$	10^6	0	∞	$256 \times 256 \times 256$	2.0	5.82	2730	8	100
1-2	$1:1:1$	10^6	50	40.53	$256 \times 256 \times 256$	2.0	5.50	2184	24	100
1-3	$1:1:1$	10^6	75	18.01	$256 \times 256 \times 256$	2.0	5.08	1758	19	100
1-4	$1:1:1$	10^6	100	10.13	$256 \times 256 \times 256$	2.0	4.43	140	15	100
1-5	$1:1:1$	10^6	150	4.50	$256 \times 256 \times 256$	2.0	3.42	956	11	100
1-6	$1:1:1$	10^6	200	2.53	$256 \times 256 \times 256$	2.0	3.54	990	8	100
1-7	$1:1:1$	10^6	300	1.13	$384 \times 384 \times 384$	2.0	2.43	636	9	100
1-8	$1:1:1$	10^6	500	0.41	$384 \times 384 \times 384$	2.5	1.36	295	10	30
1-9	$1:1:1$	10^6	600	0.28	$384 \times 384 \times 384$	2.5	1.25	216	9	30
series 2: start from a fully turbulent state of run 2-1 ($Ha = 0$)										
2-1	$1:1:1$	10^6	0	∞	$256 \times 256 \times 256$	2.0	5.82	2730	8	100
2-2	$1:1:1$	10^6	50	40.53	$256 \times 256 \times 256$	2.0	5.54	2182	24	100
2-3	$1:1:1$	10^6	75	18.01	$256 \times 256 \times 256$	2.0	5.05	1761	19	100
2-4	$1:1:1$	10^6	100	10.13	$256 \times 256 \times 256$	2.0	4.43	1399	15	100
2-5	$1:1:1$	10^6	150	4.50	$256 \times 256 \times 256$	2.0	3.41	955	11	100
2-6	$1:1:1$	10^6	200	2.53	$256 \times 256 \times 256$	2.0	2.64	723	8	100
2-7	$1:1:1$	10^6	300	1.13	$384 \times 384 \times 384$	2.0	1.61	399	9	100
2-8	$1:1:1$	10^6	500	0.41	$384 \times 384 \times 384$	2.5	1.36	293	10	30
2-9	$1:1:1$	10^6	600	0.28	$384 \times 384 \times 384$	2.5	1.12	160	9	30
series 3: start from a fully turbulent state of run 3-1 ($Ha = 0$)										
3-1	$4:4:1$	10^6	0	∞	$512 \times 512 \times 256$	2.0	5.25	2900	8	80
3-2	$4:4:1$	10^6	100	10.13	$512 \times 512 \times 256$	2.0	3.90	1282	15	80
3-3	$4:4:1$	10^6	200	2.53	$1024 \times 1024 \times 256$	2.0	2.32	628	8	80
3-4	$4:4:1$	10^6	300	1.13	$1024 \times 1024 \times 256$	2.0	1.34	308	6	80
series 4: start from a fully turbulent state of run 4-1 ($Ha = 0$)										
4-1	$4:4:1$	10^7	0	∞	$2048 \times 2048 \times 512$	2.5	9.75	7946	18	31
4-2	$4:4:1$	10^7	200	25.33	$2048 \times 2048 \times 512$	2.5	7.69	3532	29	31
4-3	$4:4:1$	10^7	500	4.05	$2048 \times 2048 \times 512$	2.5	4.11	1714	14	31
4-4	$4:4:1$	10^7	1000	1.01	$2048 \times 2048 \times 512$	2.5	1.41	565	8	31
4-5	$4:4:1$	10^7	1500	0.45	$2048 \times 2048 \times 512$	2.8	1.28	425	8	31
4-6	$4:4:1$	10^7	2000	0.25	$2560 \times 2560 \times 640$	2.8	1.15	287	8	31

Table 5.1: Main parameters of the simulations on turbulent Rayleigh-Bénard convection in liquid metal under effects of an externally applied vertical magnetic field. The Prandtl number is fixed to $Pr = 0.025$. The aspect ratio Γ, the Rayleigh number Ra, the Hartmann number Ha, the ratio Ra/Ra_c with $Ra_c \approx \pi^2 Ha^2$ (ratios $Ra/Ra_c < 1$ imply convection beyond the Chandrasekhar limit), the grid resolution with stretching coefficient A_z in the vertical direction, the Nusselt number Nu and the Reynolds number Re are given. We also list the number of horizontal grid planes inside the Hartmann layer with thickness $\delta_{\mathrm{Ha}} = 1/Ha$. In case of $Ha = 0$, we substitute the Hartmann layer thickness by the viscous boundary layer thickness $\delta_v = 1/(4\sqrt{Re})$. Finally, the total runtime used in the integral analysis is given in free fall time units, $T_{\mathrm{f}} = H/U_{\mathrm{f}}$.

5.2 Results for small aspect ratio cells with $\Gamma = 1:1:1$

In this section, we show the DNS results of the impact of a vertical magnetic field on liquid metal convection flow in a closed cubical cell with a small aspect ratio $\Gamma = 1:1:1$. The most important parameters used in this section are summarized in table 5.1 as series 1 and series 2. The Prandtl number is fixed to $Pr = 0.025$, the Rayleigh number to $Ra = 10^6$ and the Hartmann number is varying from 0 to 600 crossing the Chandrasekhar limit, where $Ha_c = \sqrt{Ra}/\pi \approx 318$ for the chosen $Ra = 10^6$. In series 1, the DNS runs start from a zero state from very beginning ($t = 0$) as shown in figure 5.1(a) and in series 2, the DNS runs start from a fully developed turbulent state of Rayleigh-Bénard convection in the absence of magnetic field of $Ha = 0$, as shown in figure 5.1(b). Time series of kinetic energy are shown in figure 5.2. We have relaxed all simulations starting from their initial conditions until the turbulent kinetic energy fluctuates around a steady state for lower Ha or saturates at a visibly constant level for higher Ha and then start the integral analysis. Figure 5.2 indicates that the runs which start from the very beginning need more time to relax than those based on $Ha = 0$, especially for the runs with higher Ha. The most obvious example is the run at $Ha = 200$. In addition, we observe a weak evolution of the profile near $800T_f$ for the run 1-7 that of $Ha = 300$ which starts from the very beginning. It implies that convection under strong vertical magnetic field may evolve very slow, if we run the simulations forever, different state may be detected, but we cannot afford that. In this study, we focus on the general characteristics based on the limited run times.

From the first view on the energy fluctuations 5.2, we observe that the vertical magnetic field tends to decrease the total energy as well as the fluctuations of the energy of turbulent convection in liquid metal. A sufficiently strong vertical magnetic field, especially those close to and beyond the Chandrasekhar limit, i.e. $Ha = 300$, 500, 600, the kinetic energy saturates at a visibly constant level with the fluctuation being suppressed completely. Next, we will give a detail discuss of the heat and momentum transfer in the system as well as the determining mechanisms and features of the flow.

5.2.1 Global transport of heat and momentum

The first analysis step is to study the global transport of heat and momentum in the system at hand. Figure 5.3 displays the the Nusselt number Nu and the Reynolds number Re versus square of the Hartmann number Ha^2 respectively. For the DNS runs in series 1, which start with the zero state at the very beginning, both Nu and Re decrease monotonically with the increase of Ha for $Ha \leq 150$, while from $Ha = 150$ to $Ha = 200$, we observe a slightly increase of Nu and Re. With Ha increasing

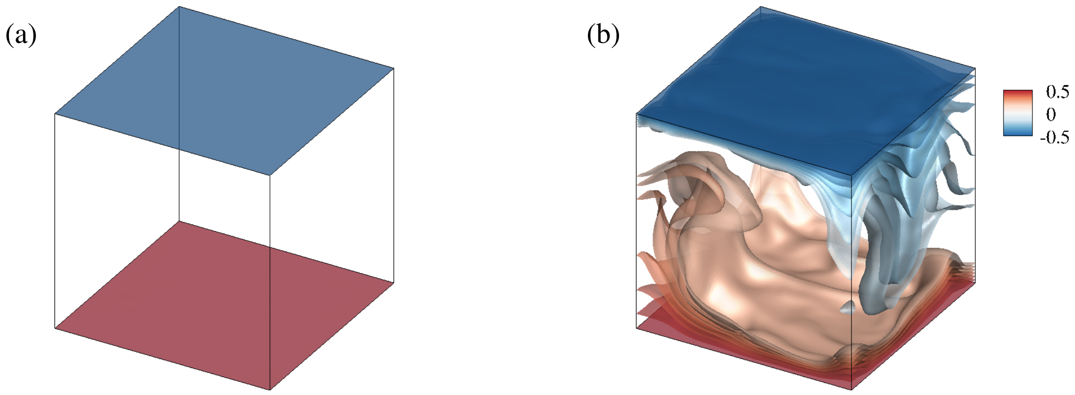

Figure 5.1: (a) Zero state at very beginning ($t = 0$), which is the initial state for the DNS runs in series 1. (b) A fully developed turbulent state at $Ha = 0$ with $Ra = 10^6$ and $Pr = 0.025$, which is the initial state for the DNS runs in series 2. Iso-surfaces of temperature field are shown.

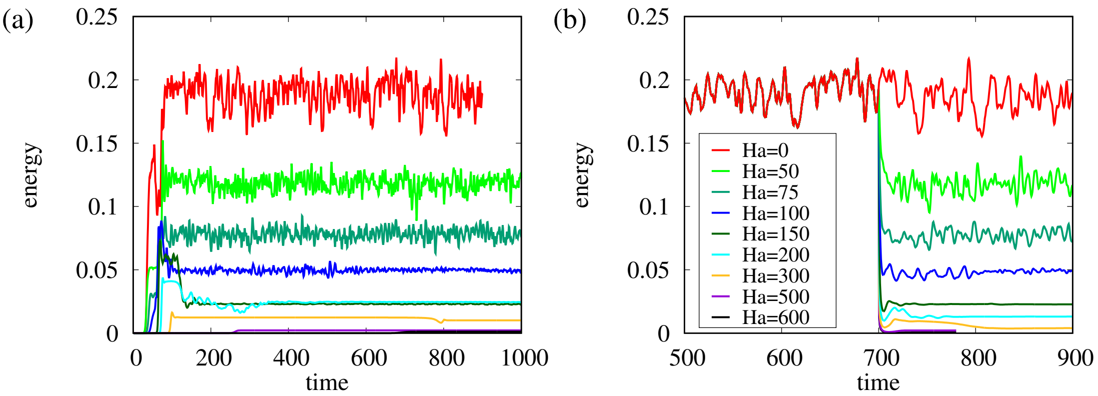

Figure 5.2: Time series of kinetic energy (Eq. 4.4). We show $2E_k$ for (a) the DNS series 1 which starts from the zero state at very beginning ($t = 0$), (b) the DNS series 2 which starts from the fully developed turbulent state at $Ha = 0$ (run 2-1).

further, both Nu and Re decrease monotonically again. For the DNS runs in series 2, which start with a fully developed turbulent state at $Ha = 0$, both Nu and Re decrease monotonically with the increasing of Ha up to $Ha = 600$. For $Ha \leq 150$, Nu as well as Re coincide with those in series 1 very well, while at $Ha = 200$ and $Ha = 300$, the Nu and Re are observably smaller than those in series 1.

The global momentum transport is further analyzed by displaying the root mean square (r.m.s.) velocities that have been obtained by a combined volume and time average which is denoted as $< \cdot >_{V,t}$. The r.m.s. values are defined as:

$$u_{rms} = \sqrt{< u_x^2 + u_y^2 + u_z^2 >_{V,t}}, \quad w_{rms} = \sqrt{< u_z^2 >_{V,t}}, \quad u_{rms}^h = \sqrt{< u_x^2 + u_y^2 >_{V,t}}. \quad (5.1)$$

Here, u_{rms} denotes the fully velocity field, w_{rms} the vertical velocity component and u_{rms}^h the horizontal velocity components. As shown in figure 5.4, the horizontal r.m.s.

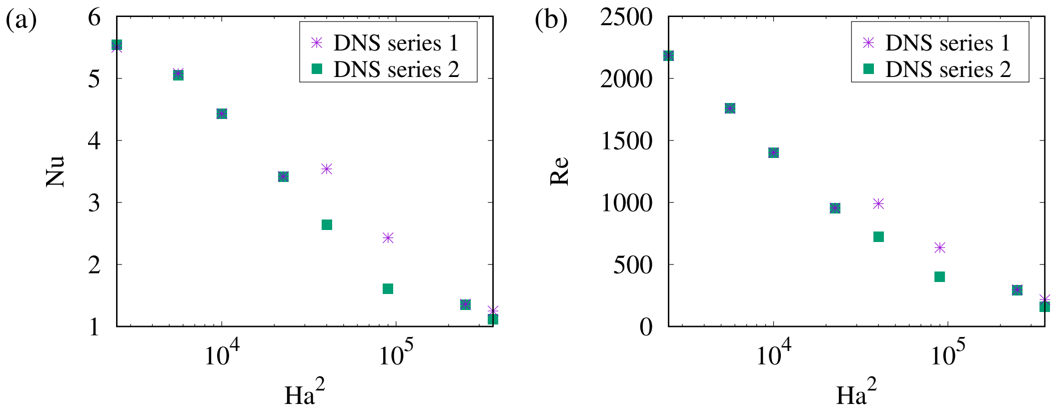

Figure 5.3: (a) The Nusselt number Nu and (b) the Reynolds number Re versus square of the Hartmann number Ha^2 for DNS runs with different initial states. Here, $Pr = 0.025$, $Ra = 10^6$ and $\Gamma = 1:1:1$. DNS series 1 starts from the zero state at very beginning and DNS series 2 starts from the fully developed turbulent state at $Ha = 0$.

velocities u^h_{rms} are increasingly suppressed as the external vertical magnetic field increases in DNS series 1 as well as in series 2. However, the vertical r.m.s. velocity w_{rms} increases obviously from $Ha = 150$ to $Ha = 200$ in series 1, which compensates for the decreases of horizontal components and results in the slight increase in total r.m.s. velocity u_{rms} as well as in Nu and Re from $Ha = 150$ to $Ha = 200$. In addition, the vertical r.m.s velocity w_{rms} has a comparable value with the horizontal r.m.s. velocity u^h_{rms} at the same Ha for $Ha \leq 300$ in series 2, which is also true for $Ha \leq 150$ in series 1. While the vertical r.m.s velocities w_{rms} at $Ha = 200$ and $Ha = 300$ in series 1 are obviously larger than the horizontal components u^h_{rms}. At highest Hartmann number $Ha = 600$, which is almost twice of the Chandrasekhar threshold, the Nusselt number decreases to almost the pure diffusion case of $Nu = 1$, but is still above 1, implying that the transport is not shut down completely. The Reynolds number also drops to a small value which corresponds with a quasisteady laminar flow.

This global analysis is refined in figures 5.5 and 5.6 by displaying the vertical profiles that have been obtained by a combined horizontal plane and time average which is denoted as $< \cdot >_{A,t}$. Figure 5.5 shows the profiles for selected DNS runs in series 1 which start from the zero state at the very beginning. Figure 5.5(a) shows the mean temperature profiles. A well-mixed region in the bulk of the flow in the absence of a magnetic field is observed. The imposed vertical magnetic field deforms the profile visibly, showing apparent shortening of the uniform bulk central region and thickening of the wall thermal boundary. For $Ha \geq 300$, the profile changes to an almost linear diffusion-dominated profile. The Nusselt number Nu can be decomposed into two

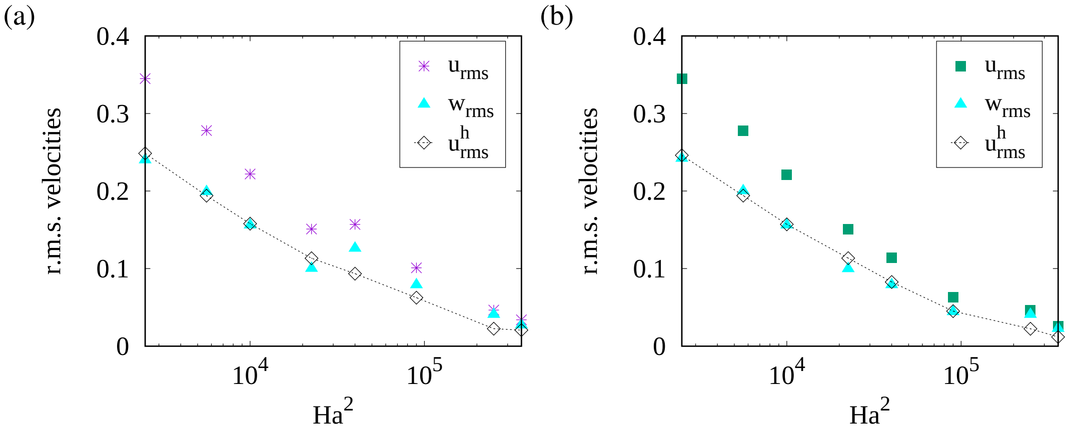

Figure 5.4: Root mean square (*r.m.s.*) velocities versus the square of the Hartmann number Ha^2. (a) for DNS series 1 that starts from the zero state at very beginning and (b) for DNS series 2 that starts from the fully developed turbulent state at $Ha = 0$. u_{rms} denotes the fully velocity field, w_{rms} the vertical velocity component and u^h_{rms} the horizontal velocity components (Eq. 5.1).

terms that stand for convective and diffusive heat fluxes across the layer,

$$Nu(z) = j_c(z) + j_d(z) = \sqrt{RaPr}\,\langle u_z T\rangle_{A,z} - \frac{\partial \langle T\rangle_{A,t}}{\partial z} = const\,. \tag{5.2}$$

Figures 5.5(b) and (c) display the profiles of the diffusive term, $j_d(z)$, and the convective term $j_c(z)$, respectively. As known from turbulent Rayleigh-Bénard convection, the diffusive term dominates in the boundary layers close to the plates while the convective term contributes almost completely to the turbulent heat transfer in the bulk. Their sum $Nu(z)$ has to be independent of z which is shown in 5.5(c) by the dashed line. This feature is observable for runs at $Ha \leq 300$. While the run with the highest Hartmann value of $Ha = 600$ is dominated by diffusion throughout the whole layer, i.e., $j_d(z) > j_c(z)$ for all $z \in [-0.5, 0.5]$. Similar results are observed at $Ha = 500$ which is not shown in the figure.

Figures 5.5(d, e, f) display the vertical profiles of the r.m.s. velocities, which are relatively defined as

$$u_{rms}(z) = \sqrt{< u_x^2 + u_y^2 + u_z^2 >_{A,t}},\ w_{rms}(z) = \sqrt{< u_z^2 >_{A,t}},\ u^h_{rms}(z) = \sqrt{< u_x^2 + u_y^2 >_{A,t}}. \tag{5.3}$$

Figure 5.5(d) display the total r.m.s. velocity profiles. For $Ha = 0$, total fluctuations u_{rms} are enhanced at the edge of the boundary layer, which is related to the detachment of thermal plumes Scheel & Schumacher [2016]. This process is increasingly suppressed as the external vertical magnetic field is increasing. The horizontal velocity fluctuations u^h_{rms}, as shown in figure 5.5(f) yield a significant contribution to this

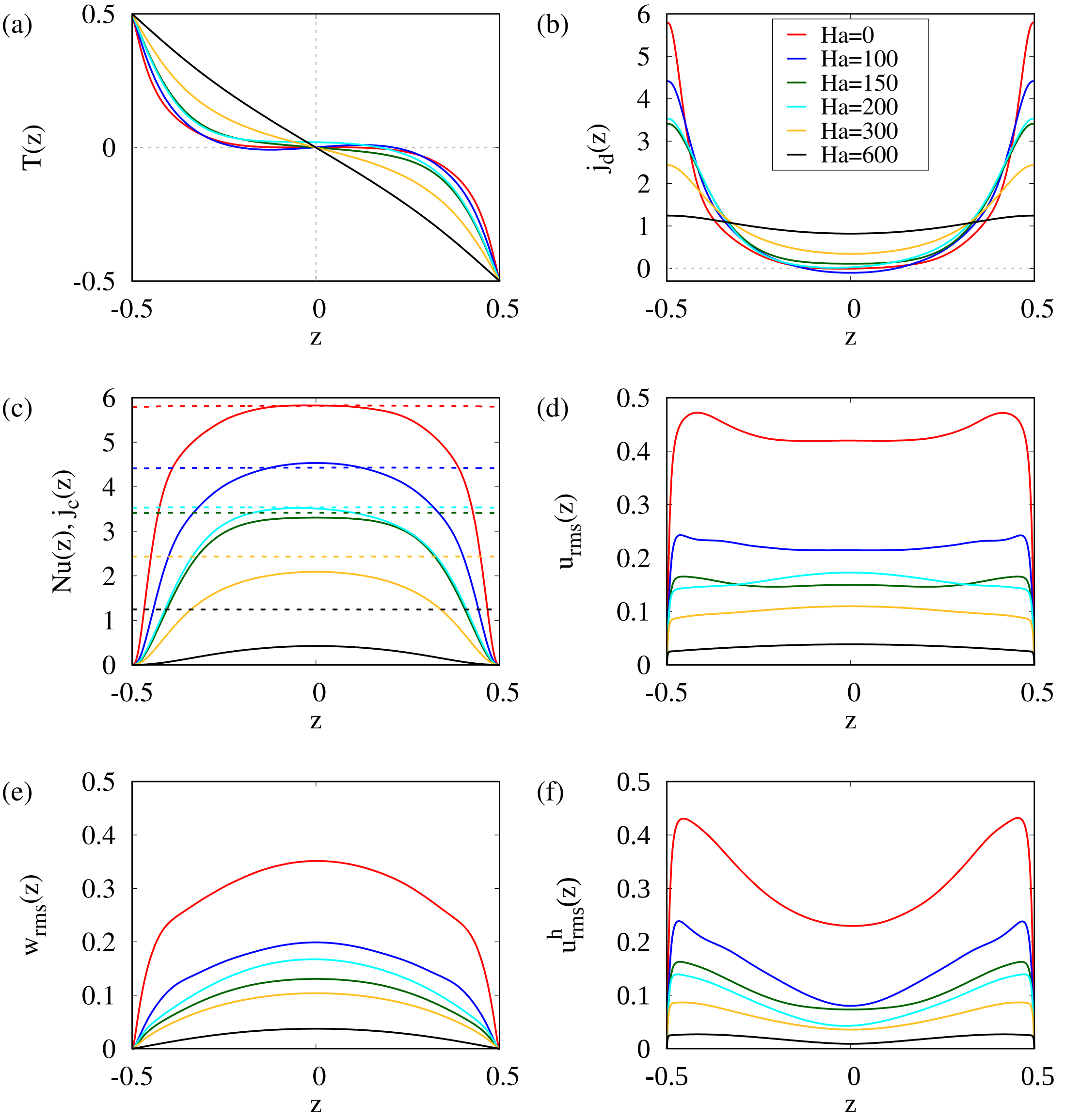

Figure 5.5: Results for data sets of series 1 that with $Pr = 0.025$, $Ra = 10^6$, $\Gamma = 1:1:1$ and starts from the zero state at very beginning. The z-dependent mean profiles of (a) temperature $T(z) =< T >_{A,t}$, (b) diffusive flux $j_d(z) = -\partial \langle T \rangle_{A,t}/\partial z$ and (c) convective heat flux $j_c(z) = \sqrt{RaPr} < u_z T >_{A,t}$ for various Hartmann numbers. The dashed lines in (c) are the corresponding Nusselt numbers $Nu(z) = j_c(z) + j_d(z)$. The z-dependent mean profiles of the r.m.s. velocity field for various Hartmann numbers with (d) for the total r.m.s. velocity $u_{rms}(z)$, (e) for the vertical r.m.s. velocity $w_{rms}(z)$ and (f) for the horizontal r.m.s. velocity $u^h_{rms}(z)$ (Eq. 5.3).

enhancement. And the horizontal fluctuation level of u^h_{rms} decreases at all height as the magnetic field increasing. Figure 5.5(e) shows the vertical velocity fluctuations w_{rms}, which yield significant contributions to the total fluctuation u_{rms} in the bulk. The fluctuation level of w_{rms} first decreases as the magnetic field increasing to $Ha = 150$ and then increases from $Ha = 150$ to $Ha = 200$ at all heights and decreases again as the magnetic field increasing further. The significant increase of vertical component w_{rms}

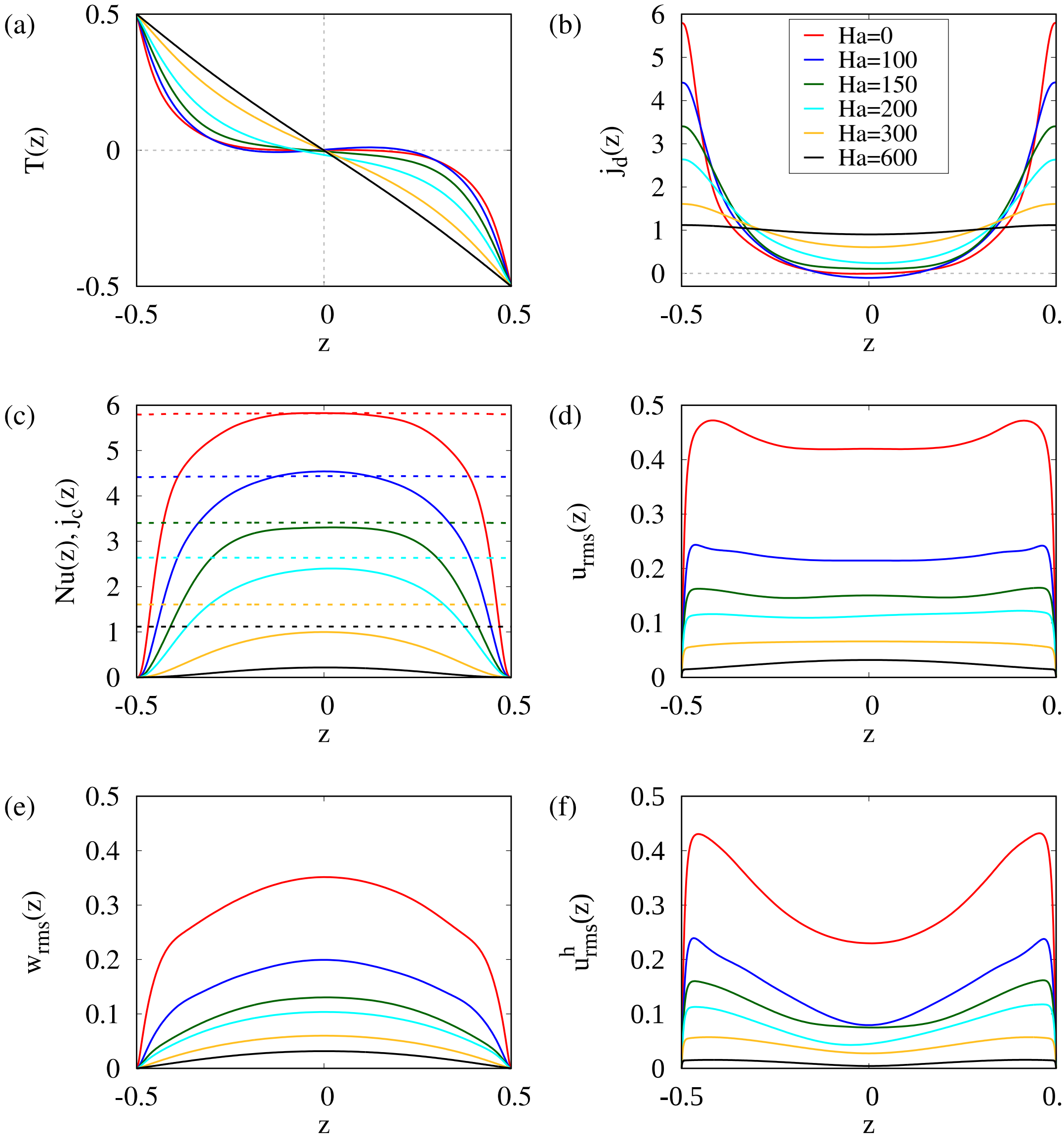

Figure 5.6: Similar to figure 5.5 but results for data sets of series 2 that with $Pr = 0.025$, $Ra = 10^6$, $\Gamma = 1:1:1$ and starts from the fully developed turbulent state at $Ha = 0$.

from $Ha = 150$ to $Ha = 200$ compensating the decrease of the horizontal component v_{rms} results in an obvious convex in the middle of the total fluctuation u_{rms} profile of $Ha = 200$, which crosses the profile of $Ha = 150$. For the run with $Ha \geq 300$, the obvious convex in the middle of u_{rms} is suppressed but still observable. The increase of vertical velocity fluctuations w_{rms} from $Ha = 150$ to $Ha = 200$ is also the reason for the slight increase of the convective fluxes as shown in figure 5.5(c). The results are in line with those shown in figure 5.3(a) and 5.4(a).

Figure 5.6 shows the vertical profiles for selected DNS runs in series 2 which start from turbulent state at $Ha = 0$. By comparing the profiles between the two series with different initial states, we could see that profiles bear very similar characteristics for the runs with $Ha \leq 150$, which is in line with the results shown in figure 5.3 that the global heat transport *Nu* and the global momentum transport *Re* coincide very well. While convex in the middle of total r.m.s. velocity profile u_{rms} at $Ha = 200$ in figure 5.5(d) is not observed here. It is not only the horizontal velocity fluctuation level decrease monotonically at all height but also that the total velocity fluctuation level as well as the vertical velocity fluctuations decrease as a whole as the external vertical magnetic field increasing from $Ha = 0$ to $Ha = 600$. The results are in line with those shown in figure 5.3(b) and 5.4(b).

In addition, an inverse in the mean temperature profiles is observed at low vertical magnetic field ($0 < Ha \leq 100$) in both DNS series 1 and series 2. As shown in figure 5.5(a) and 5.6(a), the profile for $Ha = 100$ is crossing that for $Ha = 0$ in the bulk. This phenomenon is further illustrated in 5.5(b) and 5.6(b) that the diffusive heat flux $j_d = -\partial < T >_{A,t} / \partial z$ at $Ha = 100$ become negative at the center of the cubic cell. Inverse phenomenon has been reported in experiments by Cioni *et al.* [2000] and in simulations by Hanjalić & Kenjereš [2000]. Cioni *et al.* [2000] did experiments in liquid metal mercury confined in a cylinder with a diameter-to-height aspect ratio of 1 and they reported that $dT/dz > 0$ in the interior at $Ra = 3.9 \times 10^8$ and $Ha \approx 849$ ($Ra/Ra_c \approx 54$) by measuring vertical temperature profiles along the cell axis which indicates that convection is blocked in the bulk but persists near the lateral walls from which horizontal motion could maintain the stable stratification. Hanjalić & Kenjereš [2000] did simulations using T-RANS approach in a liquid with $Pr = 0.71$ within a square box with length-height aspect ratio of 8 and they reported that the imposed vertical magnetic field deforms the mean temperature with thinning of the thermal boundary layers and extension of the core region with uniform and even inverse temperature profiles at $Ra = 10^7$ and Ha =20, 100. However, in our DNS, we do not observe thinning of the thermal boundary layers. Instead, the vertical magnetic field tends to thick the thermal boundary layers for all the DNS runs summarized in table 5.1. But we do observe an inverse in the mean temperature profiles in the central bulk region for the runs with $Ra = 10^6$, $Pr = 0.025$ and $0 < Ha \leq 100$ in the small cubic cell.

We ascribe the inverse phenomenon in temperature field to the highly confined aspect ratio. We repeat the simulation in a square box of aspect ratio $\Gamma = 4 : 4 : 1$ with the same $Ra = 10^6$, $Pr = 0.025$ and Ha =0, 100, 200, 300, summarized as series 3 in table 5.1 and the corresponding vertical profiles are shown in figure 5.7. We could see that the characteristics are very similar, while the inversion of the slope in the mean temperature profiles at low magnetic field $Ha = 100$ is not observed here. Another surprising result due to confined aspect ratio is that the temperature profiles are not symmetric between lower and upper halves of the cubic cell at moderate magnetic

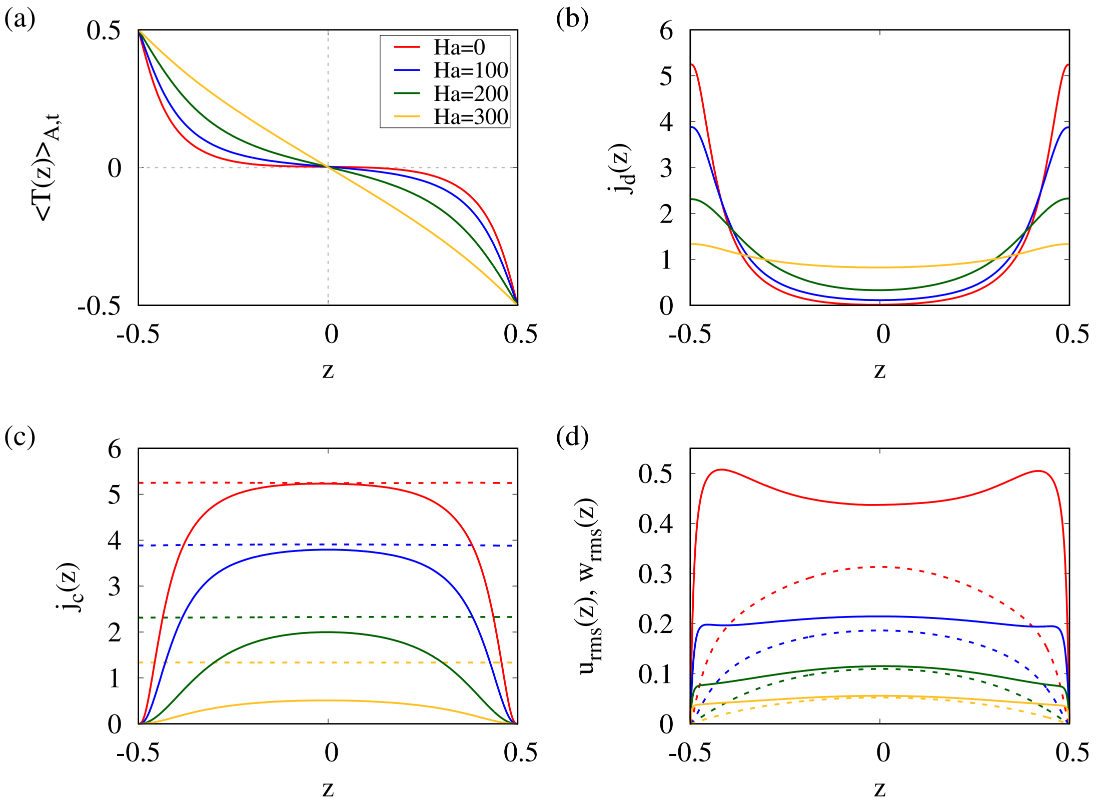

Figure 5.7: Results for data sets of series 3 that with $Pr = 0.025$, $Ra = 10^6$, $\Gamma = 4:4:1$. The z-dependent mean profile of (a) temperature $T(z) = \langle T \rangle_{A,t}$, (b) diffusive flux $j_d(z) = -\partial \langle T \rangle_{A,t} / \partial z$, and (c) convective flux $j_c(z) = \sqrt{RaPr} \langle u_z T \rangle_{A,t}$ for various Hartmann numbers. The dashed lines in (c) are the corresponding Nusselt numbers $Nu(z) = j_c(z) + j_d(z)$. (d) The z-dependent mean profile of the root-mean-square (rms) velocity field for various Hartmann numbers with the solid lines for total rms velocity $u_{rms}(z)$ and the dashed lines for vertical rms velocity $w_{rms}(z)$ (Eq. 5.3).

fields ($Ha = 150,\ 200$) especially for $Ha = 200$, as shown in figure 5.5(a) and 5.6(a). This phenomenon is also not observed for the case in a square box. The results indicates that the convection has a very complicated structure in a small cubic box and is better mixed in a large geometry.

The inversion of the slope in the mean temperature at low magnetic field and the asymmetric profiles at moderate magnetic field could also be caused by the relatively low Rayleigh number of $Ra = 10^6$, with which the flow in the cubic box is soft turbulent instead of hard turbulent, which means the convection is not mixed very well. This can be checked in the further.

Next, we move on to report the general structure of the flow at different strengths of the magnetic field and its connection to the heat and momentum transport.

5.2.2 Flow structure at different strengths of magnetic field

We begin the discussion by presenting the general structure of the flow in the absence of magnetic field ($Ha = 0$) with $Ra = 10^6$ and $Pr = 0.025$ in a cubic box with $\Gamma = 1:1:1$ (Run 1-1). It is known that Rayleigh-Bénard convection confined in a cube has a complex three-dimensional flow structure. Under fully developed conditions the flow structure is characterized by a large scale circulation (LSC) developing in a plane containing one of the diagonals of the cell. This structure is not static, with the LSC undergoing reorientations, or switching, between the two diagonal planes. The dynamic of the LSC is also geometry and input parameters dependent [Daya & Ecke, 2001; Foroozani *et al.*, 2017; Qiu & Xia, 1998; Wagner *et al.*, 2014]. For the chosen $Pr = 0.025$ and $Ra = 10^6$ (Run 1-1), the flow pattern in a cubic box is shown in figure 5.8. Isosurfaces of instantaneous temperature field at three different instants in time and the corresponding skin friction field $\boldsymbol{s} = (\partial u_x/\partial z, \partial u_y/\partial z)$ at the bottom plate are shown. The skin friction field can be considered as a blueprint of the near-wall viscous boundary layer dynamics [Bandaru *et al.*, 2015]. One can see that the primary flow structure takes form of a single LSC which is spreading over the whole area and changing its orientation with time. The wind direction in a plane near the bottom plate at $z = -0.498$ can be calculated by

$$\phi(z = -0.498, t) = arctan\left(\frac{< u_y(z = -0.498, t) >_A}{< u_x(z = -0.498, t) >_A}\right). \tag{5.4}$$

Figure 5.9(a) shows the value of ϕ corresponding to the direction. The red profile denoted by Run 1-1 in figure 5.9(b) displays the time-dependent orientation angle corresponding to the run shown in figure 5.8. We could see that the direction of wind on a plane near the bottom wall oscillates between -0.75π and -0.25π approximately. Figure 5.8(a, d) show an example of flow structure near $\phi = -0.75\pi$ and figure 5.8(c, f) near $\phi = -0.25\pi$. It is clearly shown that the LSC is oscillating between the two diagonal planes. Figure 5.8(b, e) show an example of flow structure in the between near $\phi = -0.5\pi$ that the flow is mainly pointing to the negative y-direction. During our limited run time, the averaged y-direction velocity component over the whole plane near bottom wall is always negative, which indicates that with the chosen input parameter the LSC is oscillating between two adjacent diagonals. We also check the *Nu* and *Re* at different instants. It shows that the diagonally organized structure transports more heat and momentum. We have repeated the simulation with exact same input parameters and initial state for several times and detected another two oscillating procedures as shown in figure 5.9(b). The purple profile denoted by 'Run 1-1a' indicates the LSC oscillating between 0.25π and 0.75π while the green profile denoted

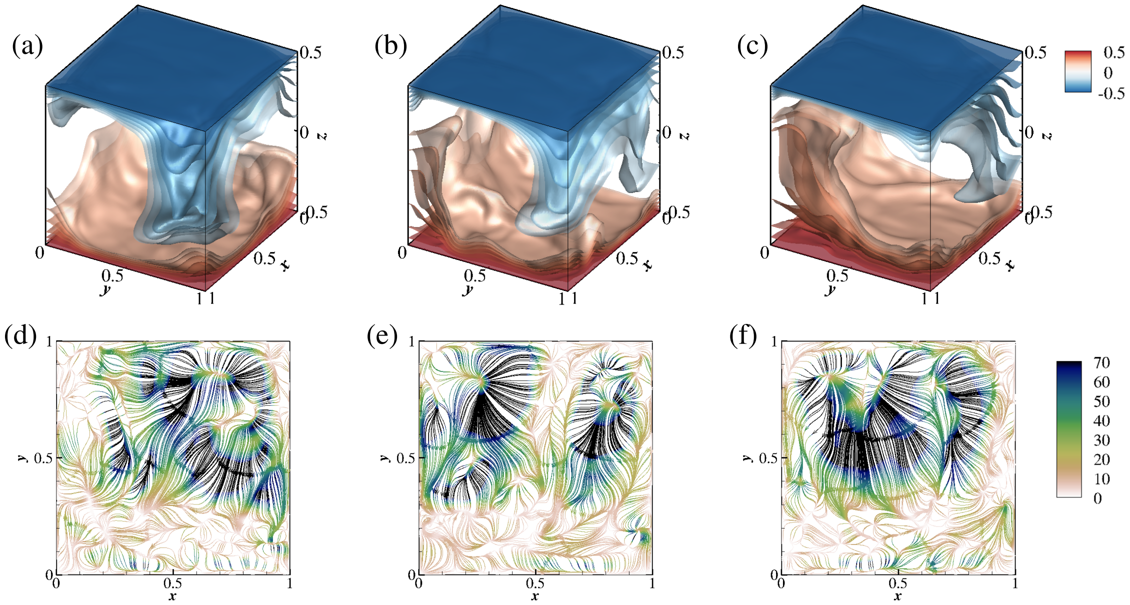

Figure 5.8: Instantaneous flow pattern in the absence of magnetic field at $Pr = 0.025$, $Ra = 10^6$ in a cubical box (Run 1-1). Three different snapshots are shown. (a, b, c) show isosurfaces of temperature field. (d, e, f) show streamlines of the skin friction field $\boldsymbol{s} = (\partial u_x/\partial z, \partial u_y/\partial z)$ at the bottom plate. Field lines are colored by the magnitude of the vector field. $Nu = 6.33, 5.44, 6.50$ and $Re = 2841, 2658, 2837$ from left to right.

by 'Run 1-1b' indicates the LSC oscillating between -0.25π and 0.25π. For all the three cases shown in 5.9(b), the LSC is locked between two adjacent diagonals, i.e., the direction of LSC is changing over a range of 0.5π. And the oscillating frequency is approximately 0.0163 T_f^{-1} for all the three cases. The time-averaged flow pattern corresponding to the three runs in 5.9(b) are shown in figure 5.10. The average is taken over the last 100 T_f shown in 5.9(b). Foroozani *et al.* [2017] found that the LSC in a cube can oscillate over the whole cell, i.e. over a range of 2π, with input parameter $Pr = 0.7$ and $Ra = 10^8$ during a run time of 1200 eddy-turnover time which is approximately 36000 free-fall time units. If we run our simulation longer enough we may also detect LSC oscillating over arrange of 2π or if we repeat the same simulation again and again, we may detect more different oscillating procedures. Nevertheless, we can general summarize that the flow pattern in Rayleigh-Bénard convection that confined in a cube with $Ra = 10^6$ and $Pr = 0.025$ take forms of a single LSC occupying almost complete central region with its orientation oscillating with time. And the diagonally organized structure transports more heat and momentum.

We now move on to present some qualitative illustration of the effect of a vertical magnetic field. Fgiures 5.11, 5.12 and 5.13 summarize the general flow pattern in a cubic cell of $\Gamma = 1:1:1$ at various Hartmann numbers with $Pr = 0.025$, $Ra = 10^6$ that are computed starting from the zero state at very beginning, corresponding to the DNS runs in series 1. Time-averaged temperature field, velocity field as well as the

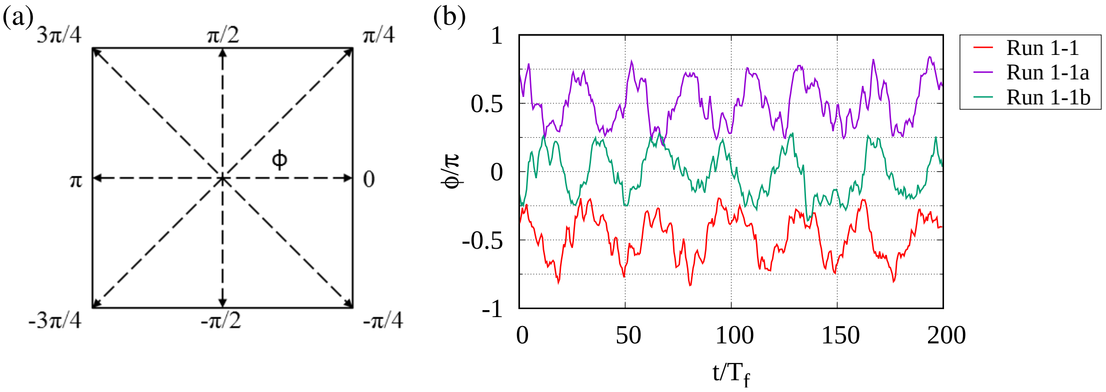

Figure 5.9: (a) Schematic of orientation angle ϕ corresponding to the flow direction. (b) Local orientation angle ϕ as a function of time as measured in free-fall time units for $z = -0.498$ (near bottom plate) at $Pr = 0.025$, $Ra = 10^6$ and $Ha = 0$ in a cubic box. The red line is for the run shown in figure 5.8 (Run 1-1). The other two show another two different orientation regimes detected at the same input parameters.

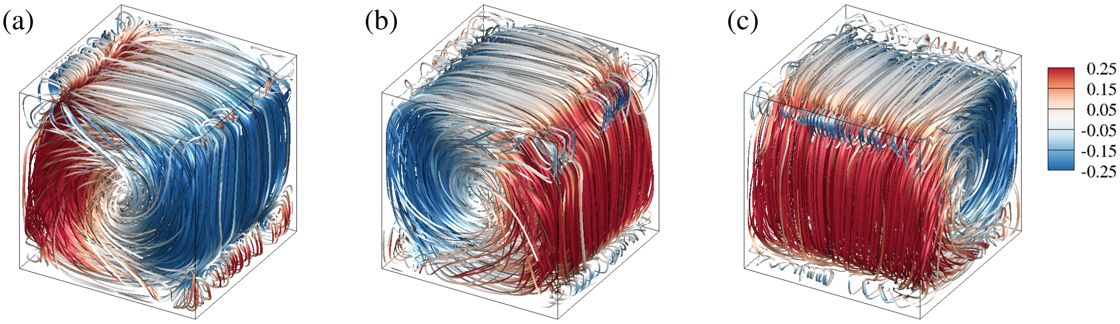

Figure 5.10: Time-averaged flow pattern over 100 T_f corresponding to the three runs shown in figure 5.9(b). (a) for 'Run 1-1', (b) for 'Run 1-1a' and (c) for 'Run 1-1b'. Streamlines of time-averaged velocity field are shown. The line are colored by vertical velocity component.

skin friction field at the bottom plate are shown respectively. The runtime used in the time-averaging is summarized in table 5.1. At low magnetic field ($Ha < 100$), taking $Ha = 50$ for example as shown in panel (a) in figure 5.11 and 5.12, the flow structures remain very similar with the nonmagnetic case (see figure 5.10) with a LSC occupying the entire cell and changing direction with time between two diagonal plane. Figure 5.14 displays the corresponding local orientation angle (see equation (5.4)) of wind on a plane near the bottom wall as a function of time for various Hartmann numbers. Long period and high amplitude fluctuations in the profile of $Ha = 0$ which are corresponding to the orientation oscillation of the LSC are damped significantly by the vertical magnetic field. The frequency of the large scale fluctuations are 0.0163, 0.0138, and 0.0063 (in unit of T_f^{-1}) for $Ha = 0$, $Ha = 50$ and $Ha = 75$ respectively. From $Ha = 100$, the influence of the vertical magnetic field becomes obviously that the global flow tends to be locked near a single diagonal plane as shown in panel (b) in figures 5.11−5.13. Figure 5.14 confirms that the large scale circulation is neither

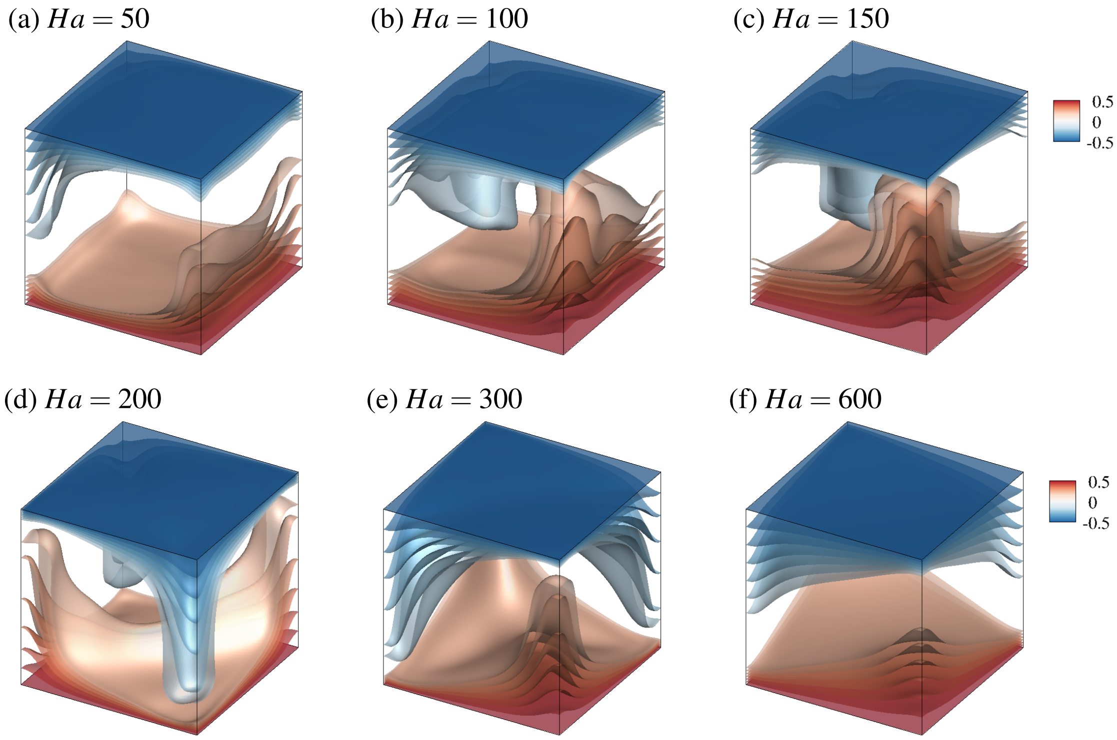

(a) $Ha = 50$ (b) $Ha = 100$ (c) $Ha = 150$

(d) $Ha = 200$ (e) $Ha = 300$ (f) $Ha = 600$

Figure 5.11: Isosurfaces of the time-averaged temperature field at various Hartmann numbers. Data sets in series 1 are considered which are computed from the zero state at very beginning.

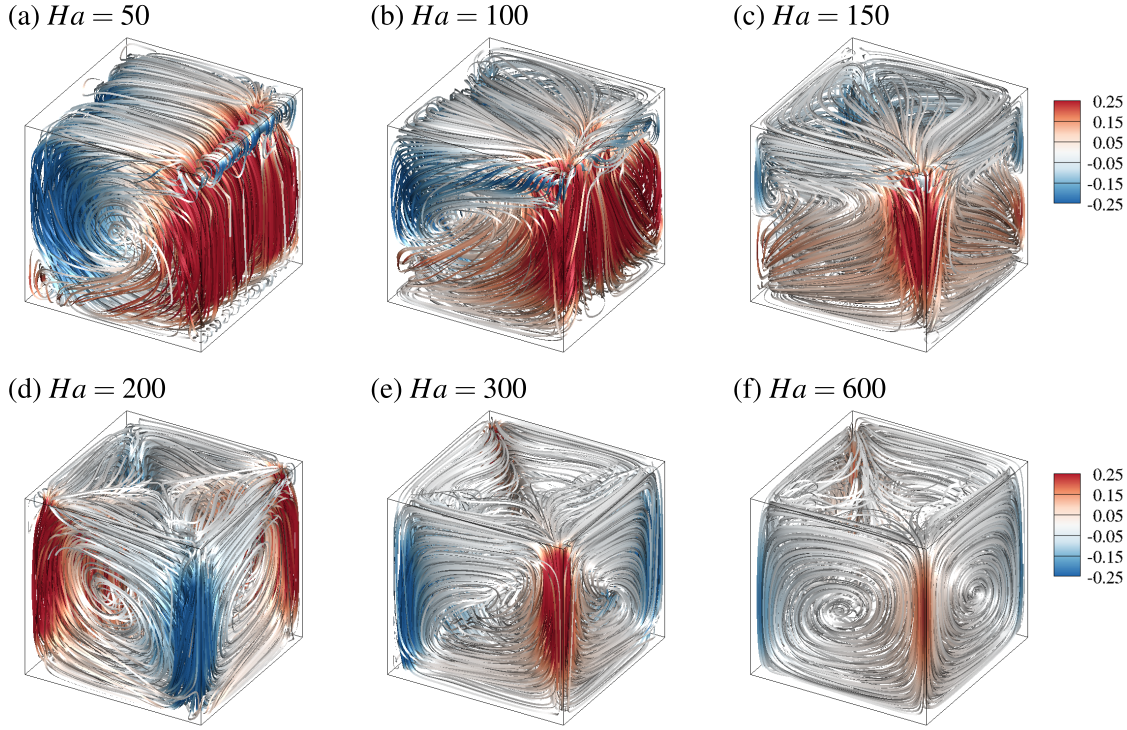

(a) $Ha = 50$ (b) $Ha = 100$ (c) $Ha = 150$

(d) $Ha = 200$ (e) $Ha = 300$ (f) $Ha = 600$

Figure 5.12: Streamlines of the time-averaged velocity field at various Hartmann numbers. Field lines are colored by vertical velocity component. Data sets in series 1 are considered which are computed from the zero state at very beginning.

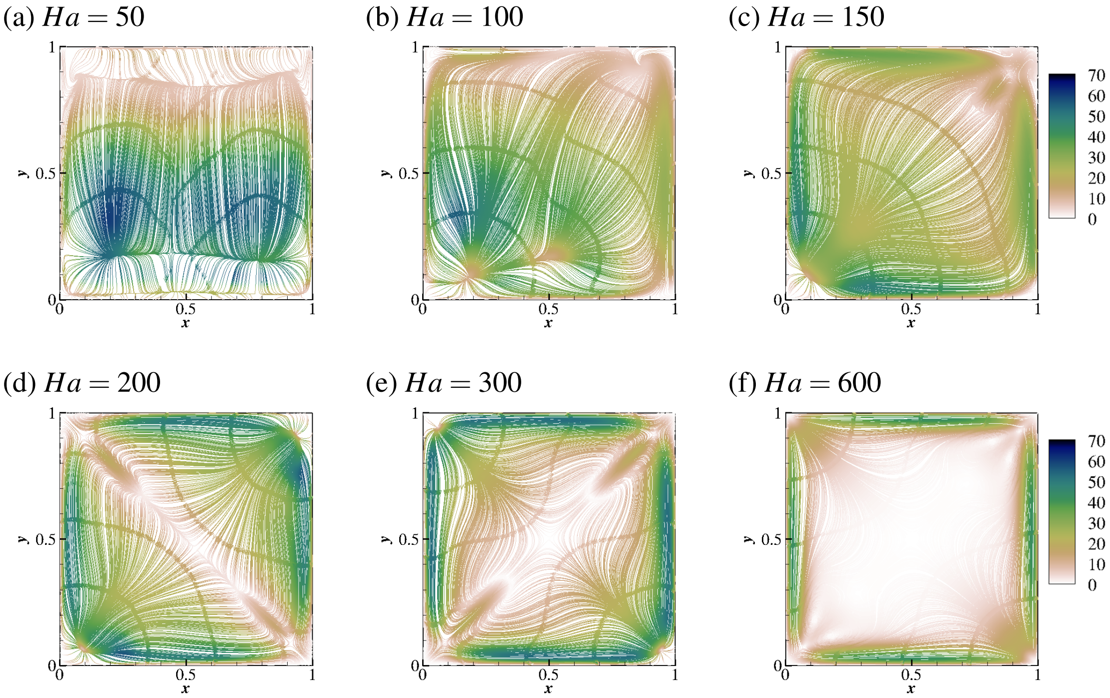

(a) $Ha = 50$ (b) $Ha = 100$ (c) $Ha = 150$

(d) $Ha = 200$ (e) $Ha = 300$ (f) $Ha = 600$

Figure 5.13: Skin friction field $\boldsymbol{s} = (\partial u_x/\partial z, \partial u_y/\partial z)$ at the bottom plate for various Hartmann numbers. The field lines are colored by the magnitude of the vector field. Data sets in series 1 are considered that computed from the zero state at very beginning.

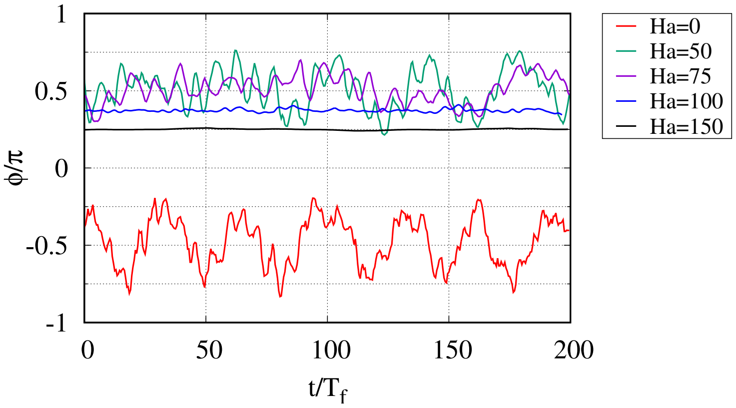

Figure 5.14: Local orientation angle ϕ ((Eq. 5.4)) as a function of time as measured in free-fall time units at $z = -0.498$ (near bottom plate) for various Hartmann number ($Ha \leq 150$). Data sets in series 1 are considered that computed from the zero state at very beginning.

parallel to one set of side walls nor orients diagonally and slight oscillations are still observed. At $Ha = 150$, the profile in figure 5.14 is almost a straight line at a constant orientation angle of $\phi = -0.25\pi$ which indicates the flow is quasi-steady and orients diagonally. Panel (c) in figures 5.11−5.13 show that the time-averaged flow pattern is almost symmetric by one of the diagonal plane. With the magnetic field increasing further, the flow tends to avoid following the diagonal direction, but moving attached to the sidewalls. The flow pattern takes form of hot fluid arising in two opposite corners

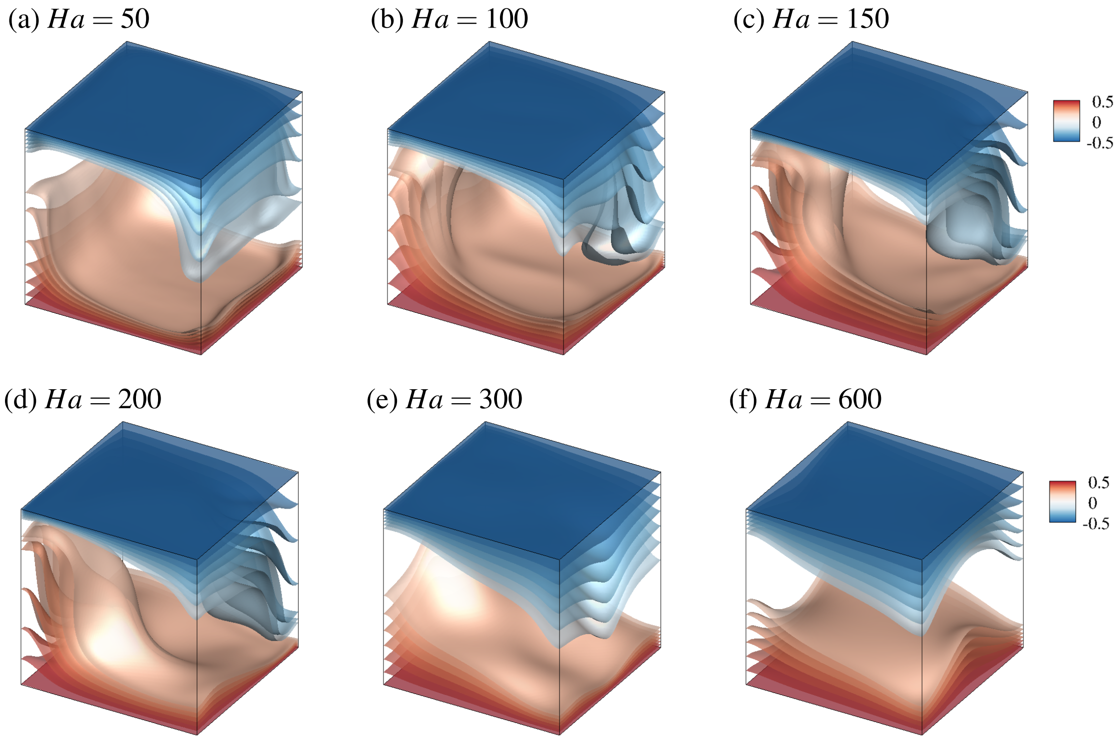
(a) $Ha = 50$ (b) $Ha = 100$ (c) $Ha = 150$

(d) $Ha = 200$ (e) $Ha = 300$ (f) $Ha = 600$

Figure 5.15: Similar to figure 5.11, but data sets in series 2 are considered which are computed starting from the fully developed turbulent state at $Ha = 0$ (see figure 5.1(b)).

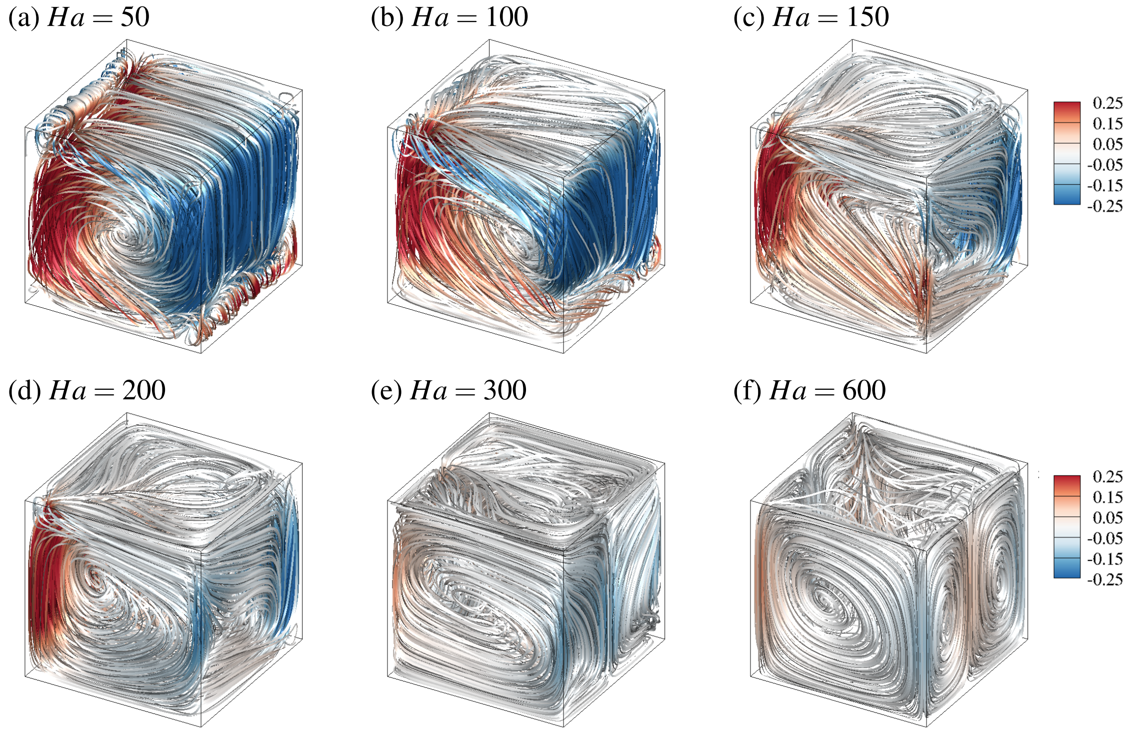
(a) $Ha = 50$ (b) $Ha = 100$ (c) $Ha = 150$

(d) $Ha = 200$ (e) $Ha = 300$ (f) $Ha = 600$

Figure 5.16: Similar to figure 5.12, but data sets in series 2 are considered which are computed starting from the fully developed turbulent state at $Ha = 0$ (see figure 5.1(b)).

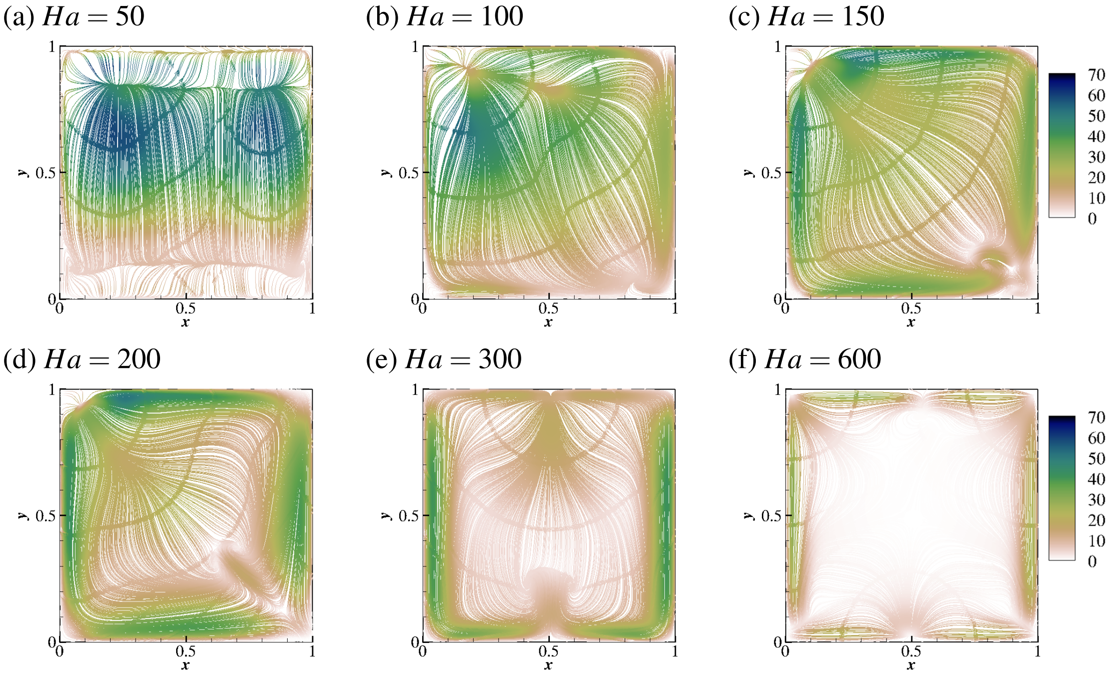
(a) $Ha = 50$ (b) $Ha = 100$ (c) $Ha = 150$

(d) $Ha = 200$ (e) $Ha = 300$ (f) $Ha = 600$

Figure 5.17: Similar to figure 5.13 but data sets in series 2 are considered which are computed starting from the fully developed turbulent state at $Ha = 0$ (see figure 5.1(b)).

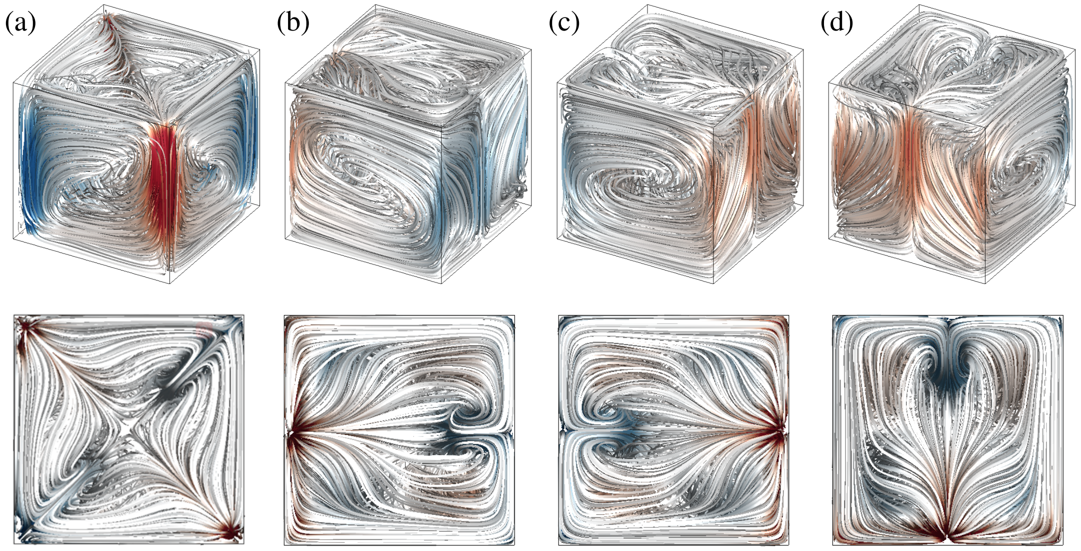

Figure 5.18: Time-averaged flow pattern at $Ha = 300$ based on different initial states: (a) zero state from very beginning, (b) fully turbulent state at $Ha = 0$, (c) state at $Ha = 100$, (d) state at $Ha = 150$. The second row display the top view of the first row.

and cold fluid descending in the adjacent corners, as shown in panel (d-f) in figure 5.11 and 5.12. The structures are increasingly closely attached to the sidewalls as the magnetic field increasing. For the highest Hartmann number of $Ha = 600$, the structure still survives and the flow motion in the interior of the cell are almost completely suppressed.

We continue to present the results corresponding to the DNS runs in series 2, which are computed starting from the fully developed turbulent state in the absence of magnetic field as shown in figure 5.1(b). The input parameters are still fixed to $Pr = 0.025$, $Ra = 10^6$ and $\Gamma = 1:1:1$. Figures 5.15, 5.16 and 5.17 summarize the time-averaged temperature field, velocity field as well as the skin friction field at the bottom plate respectively, for various Hartmann numbers. The general flow patterns for $Ha \leq 150$ remain quite similar between the two DNS series that with different initial states. Although the positions where the hot fluid arises and cold fluid descends are different, which is due to the nature of Rayleigh-Bénard convection, the integral heat and momentum transports are the same as shown in figures 5.3 and 5.4. With strong magnetic field that $Ha \geq 200$, the flow tend to be expelled from the interior to the near-wall regions similar to the runs in series 1. However, the wall attached structures are organized quite differently between the two DNS series. For $Ha = 200$ in series 2 (Run 2-6, which is computed starting from the fully developed turbulent state of $Ha = 0$), as shown in panel (d) in figures 5.15−5.17, the flow pattern remains similar to that for $Ha = 150$ that the hot fluid arises at one corner and the cold flow descends at the opposite corner with the whole flow being more expelled from the interior. However, the flow pattern for $Ha = 200$ in series 1 (Run 1-6 , which is computed starting from a zero state from very beginning), as shown in panel (d) in figures 5.11 and 5.12, takes form of the hot fluid arising in two opposite corners and the cold fluid descending in the adjacent corners, which carries more vertical momentum transport as shown in figure 5.5(e), resulting the corresponding Nu and Re higher than those in series 2 at $Ha = 200$ and even higher than those at $Ha = 150$. For $Ha = 300$ in series 2 (Run 2-7), as shown in panel (e) in figures 5.15−5.17, the flow takes form of two-roll-like structure pointing from one sidewall to the opposite sidewall instead of any diagonal motion.

Figure 5.18 displays the flow pattern at $Ha = 300$ based on different initial states. Besides the two initial states, i.e., zero state and fully turbulent state, that we mentioned already, we add the pattern at $Ha = 300$ based on the flow state at $Ha = 100$ and $Ha = 150$ respectively. As shown in figure 5.18, the general features of the pattern based on $Ha \neq 0$ are the same. We have checked that the Nusselt and Reynolds numbers are also similar in these three cases. The differences come from the position where the hot fluid rises and the cold fluid sinks. This is due to the natural feature of Rayleigh-Bénard convection that plume detach randomly from the top and bottom plates into the bulk of the cell. Since the diagonal structure transports more heat and momentum, the Nu and Re in figure 5.3 at $Ha = 300$ in series 1 (run 1-7) are larger than those the runs in series 2 (run 2-7).

5.2.3 Summary and discussion

We summarize here the main DNS results of the impact of a vertical magnetic field on liquid metal convection flow in a closed cubical cell with a small aspect ratio $\Gamma = 1:1:1$. In the absence of magnetic field, the flow pattern in Rayleigh-Bénard convection that confined in a cube with $Ra = 10^6$ and $Pr = 0.025$ takes form of a single LSC occupying almost complete central region with its orientation oscillating with time. A vertical magnetic field inhibits the oscillation of LSC and thus decreases the heat and momentum transport. As the magnetic field is increased, the convection tends to be expelled from the interior to the near-wall regions with the fluid motion almost completely absent in the bulk.

By conducting DNS with different initial states, we detected multiple states for equal input parameters. These multiple states may influence the heat and momentum transport obviously, especially for the runs with moderate magnetic field. The reason is that different LSC states occupy the cell that dominate transport.

For the runs with low magnetic field, we observe an inversion of the slope of the mean temperature profiles in the bulk of the cubic cell which is due to the highly confined small aspect ratio.

5.3 Results for large aspect ratio cells with $\Gamma = 4:4:1$

In this section, we show the DNS results of the impact of a vertical magnetic field on liquid metal convection flow in a closed square cell with a large aspect ratio $\Gamma = 4:4:1$. We mainly show the results concerning the high Rayleigh number runs summarized as series 4 in the table 5.1. The Prandtl number is still fixed to $Pr = 0.025$. the Rayleigh number is increased to $Ra = 10^7$, with which the flow is highly turbulent in the absence of magnetic field. The Hartmann number is increased up to $Ha = 2000$, which is twice of the Chandrasekhar threshold Ha_c approximately with $Ha_c \approx 1007$ for $Ra = 10^7$. All the DNS runs for magnetoconvection start from a fully turbulent state in the absence of magnetic field for the same Ra.

The values of the Reynolds number Re and Nusselt number Nu of non-MHD case (run 4-1) are comparable with those from Scheel & Schumacher [2016] for Rayleigh-Bénard convection in mercury at $Pr = 0.021$ in a closed cylindrical cell at $\Gamma = D/H = 1$ where $Nu = 10.11 \pm 0.05$ and $Re = 8450 \pm 100$ is reported. For the magnetoconvection runs, we compares our Nusselt numbers Nu against the experiments in a closed cylinder by Cioni *et al.* [2000] as shown in figure 5.19. It can be seen that the experimental data record coincides well with the DNS data below the Chandrasekhar limit for all the runs in series 4, where large aspect ratio $\Gamma = 4:4:1$ and the highest Rayleigh

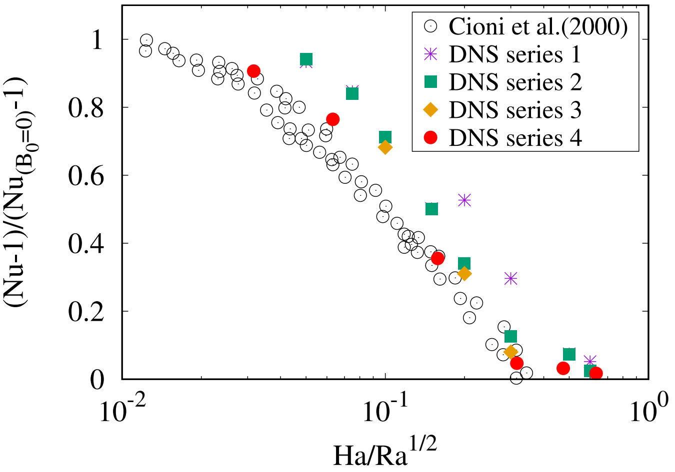

Figure 5.19: Nusselt number Nu normalized with respect to the Nusselt number value at $B_0 = 0$ versus $Ha/\sqrt{Ra}$. A part of the data of the experiment by Cioni *et al.* [2000] is added (open circles).

number $Ra = 10^7$ are considered. For comparison, we also include the DNS results of series 1-3 as shown in table 5.1, where a relatively low Rayleigh number of $Ra = 10^6$ are considered. The values are larger than the experimental results especially for the cases at low magnetic fields. Furthermore, the results for small aspect ratio, i.e., series 1 and 2, are also slightly larger than the results for large aspect ratio, i.e., series 3 for the same Ha. Deviations are observed for the highest magnetic fields, where the data points of the simulation branch off due to the existence of wall modes. This figure already underlines the sensitivity of the turbulent heat transfer with respect to the aspect ratio.

Next we move on to report how the convective turbulence structures and the heat and momentum transport are affected by a vertical magnetic field in detail. We will first present the results of magnetoconvection towards the Chandrasekhar limit in section 5.3.1 and then discuss the wall modes beyond the Chandrasekhar in section 5.3.2.

5.3.1 Magnetoconvection towards the Chandrasekhar limit

5.3.1.1 Flow patterns and characteristic scales

First, we present flow patterns of the magnetoconvection flows towards the Chandrasekhar limit. DNS runs of 4-1 to 4-4 in series 4, are considered here, that $Ra = 10^7$, $Pr = 0.025$, $\Gamma = 4:4:1$ and $Ha \leq 1000$. Figure 5.20 displays the flow structure by presenting two isothermal surfaces of the instantaneous temperature field. Panel (a) in figure 5.20, for $Ha = 0$, indicates a fully turbulent convection in the absence of magnetic field. With a vertical magnetic field, the plumes are randomly distributed with a wide base and peaked cores as shown in panel (b) and (c), which are for $Ha = 200$

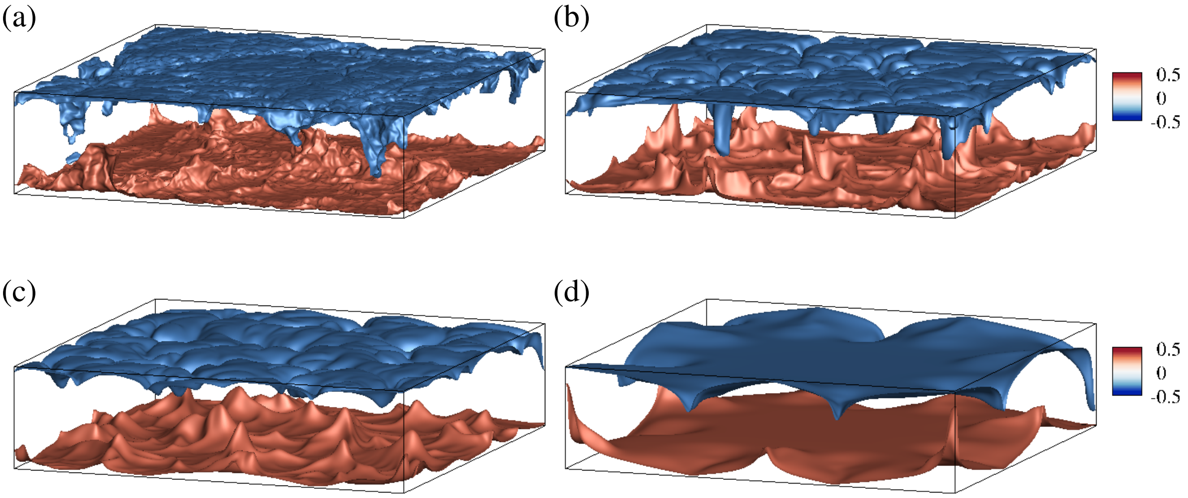

Figure 5.20: Snapshots of the magnetoconvection flow towards the Chandrasekhar limit for $Pr = 0.025$, $Ra = 10^7$ and $\Gamma = 4:4:1$. We display isosurfaces of instantaneous temperature field $T = \pm 0.32$. (a) $Ha = 0$, (b) $Ha = 200$, (c) $Ha = 500$, (d) $Ha = 1000$.

and $Ha = 500$ respectively. From $Ha = 200$ to $Ha = 500$, the plumes become more cylindrical in base shape and more orderly populated. Such a reorganization is a consequence of magnetic damping of the horizontal fluid movement and turbulent fluctuations in the horizontal directions. When the magnetic field strength approaching the Chandrasekhar limit $Ha_c \approx \sqrt{Ra}/\pi \approx 1000$, as shown in panel (d), the temperature field in the bulk is almost linearly stratified and the plumes persist near the side walls.

Further illustration of the structural reorganization is given in figure 5.21. The top row, panels (a)–(d), displays instantaneous snapshots of the vertical velocity component in the midplane at $z = 0$. It is observed that the average distance between strongly up- and downwelling fluid is decreased as Ha grows. In the bottom row, panels (e)–(h), we display the resulting time-averaged data that have been obtained for an average over the total integration time of 31 free fall time units T_f. The observation is similar. An increasing magnetic field fragments the vertical velocity field patterns. At the Chandrasekhar limit, the differences between an instantaneous snapshot and the time-averaged field are very small which implies a quasisteady behavior. The vertical velocity component seems to be completely expelled from the center of the cell when compared with the data for $Ha \ll 10^3$. The flow patterns are attached to the near-wall regions. The alternating up- and down-wellings indicate roll structures which are indeed detected.

A typical scale of the velocity pattern is found by a Fourier analysis. We take the vertical velocity component in the midplane, $u_z(x,y,0,t)$ and transform each sample into Fourier space thus obtaining $\hat{u}_z(k_x,k_y,t)$. An azimuthally averaged power spec-

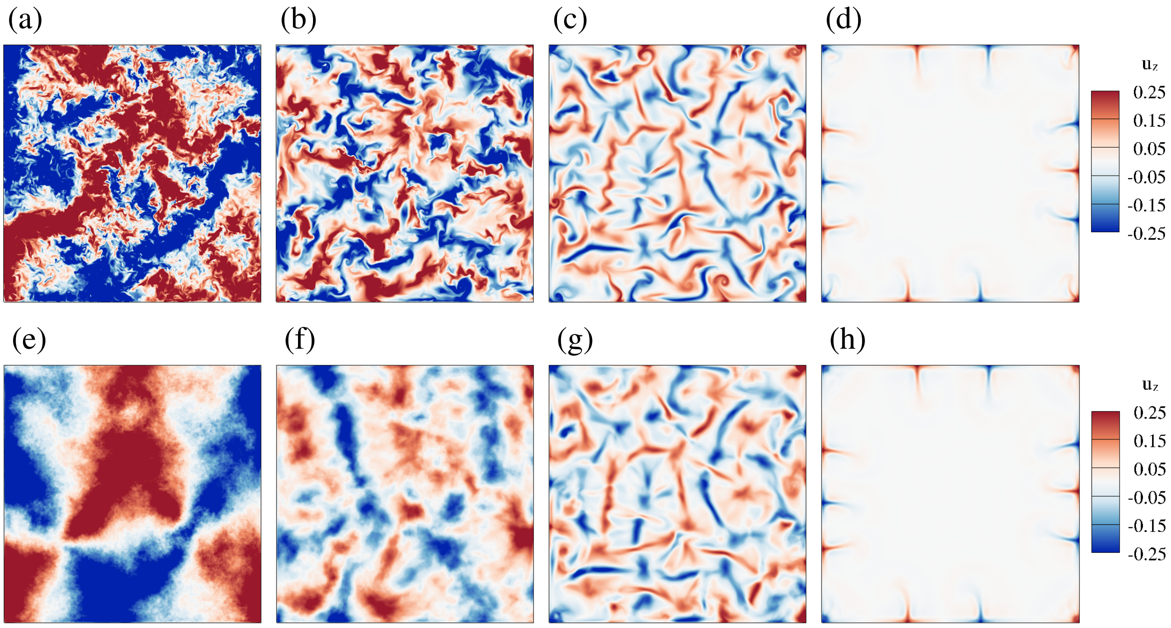

Figure 5.21: Horizontal cross sections at mid-plane ($z = 0$) of instantaneous vertical velocity field (top row) and time-averaged vertical velocity field over 62 snapshots ($31T_f$) for various Hartmann numbers at (a, e) $Ha = 0$, (b, f) $Ha = 200$, (c, g) $Ha = 500$, (d, h) $Ha = 1000$. $Pr = 0.025$, $Ra = 10^7$ and $\Gamma = 4:4:1$.

trum is then obtained by

$$E(k) = \frac{1}{2\pi}\int_0^{2\pi} \langle|\hat{u}_z(k,k_\phi,\tau)|^2\rangle_t k\, dk_\phi\,. \tag{5.5}$$

Figure 5.22(a) shows the power spectra for the four DNS runs 4-1 to 4-4. All of them obey a wavenumber k_* at which the spectrum has a maximum. We associate a typical wavelength with this wavenumber which is given by $\lambda_* = 2\pi/k_*$. This wavelength stands for a typical distance between the down- and upwelling regions in figure 5.21. While the maximum wavenumber is shifted to larger values as Ha is increased, the maximum value drops by four orders of magnitude which underlines the strong damping of the fluid motion. The characteristic spatial scale which follows from this analysis is $\lambda_* \approx 2.7$, 2, 0.89, and 0.73 for $Ha = 0$, $Ha = 200$, $Ha = 500$, and $Ha = 1000$, respectively. It is clear that the structures in this DNS series are affected by the finite box size. Nevertheless, the trend to a fragmentation into smaller velocity patterns with increasing external vertical magnetic field is clearly visible. Similar patterns are observed for the temperature field and for the skin friction field, as shown in figure 5.23.

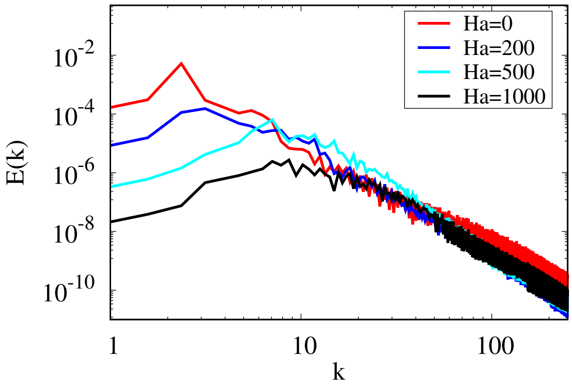

Figure 5.22: Time and azimuthally averaged vertical velocity at midplane ($z = 0$) in Fourier modes as a function of wavenumber k. The peaks of the profiles are at $k_* = 0.75\pi,\ \pi,\ 2.25\pi,\ 2.75\pi$ for $Ha = 0,\ 200,\ 500,\ 1000$ respectively.

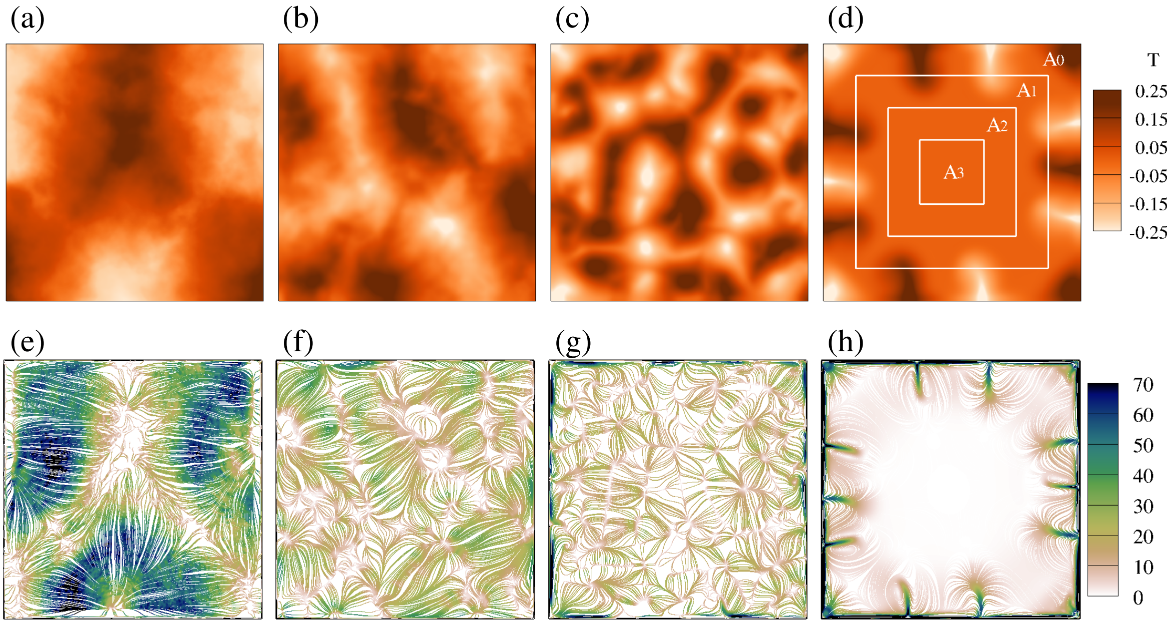

Figure 5.23: Horizontal cross sections of (a–d) the time-averaged temperature field at the midplane $z = 0$ and (e–h) the two-dimensional time-averaged skin friction field at the bottom plate $z = -0.5$ for various Hartmann numbers. From left to right $Ha = 0, 200, 500, 1000$. The white concentric squares in panel (d) denote subareas which will be used in shell analysis, where A_0 denotes for the entire cross-section area, and $A_1 = \frac{9}{16}A_0$, $A_2 = \frac{1}{4}A_0$, $A_3 = \frac{1}{16}A_0$. Field lines in panels (e)–(h) are colored by the magnitude of the vector field.

5.3.1.2 Global transport of heat and momentum

Figure 5.24 shows the vertical profiles for the DNS runs 4-1 to 4-4 in series 4. Figure 5.24(a) shows the temperature profiles for all six date set in series 4. The well-mixed bulk region for the turbulent cases at $Ha < 1000$ changes to an almost linear diffusion-dominated profile for $Ha \geq 1000$. Figure 5.24(b) and (c) display the profiles of diffusive heat fluxes $j_d(z)$ and the convective heat fluxes $j_c(z)$ respectively for

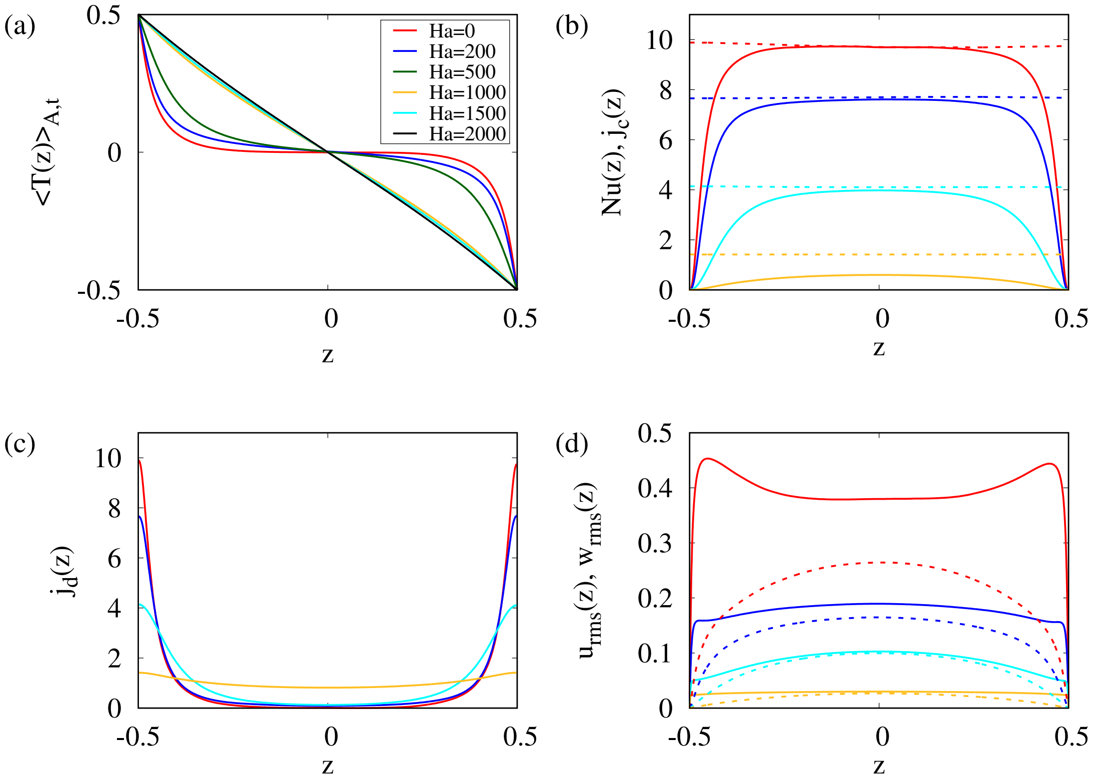

Figure 5.24: Results for $Pr = 0.025$, $Ra = 10^7$, $\Gamma = 4:4:1$ and $0 \leq Ha \leq 1000$. The z-dependent mean profile of (a) temperature $T(z) = \langle T \rangle_{A,t}$, (b) convective flux $j_c(z) = \sqrt{RaPr}\langle u_z T \rangle_{A,t}$, and (c) diffusive flux $j_d(z) = -\partial \langle T \rangle_{A,t} / \partial z$ for various Hartmann numbers. The dashed lines in (b) are the corresponding Nusselt numbers $Nu(z) = j_c(z) + j_d(z)$. (d) The z-dependent mean profile of the r.m.s. velocity field for various Hartmann numbers with the solid lines for total r.m.s. velocity $u_{rms}(z)$ and the dashed lines for vertical r.m.s. velocity $w_{rms}(z)$ (Eq. 5.3).

the runs with $Ha \leq 1000$. For $Ha < 1000$, the diffusive term $j_d(z)$ dominates in the boundary layers close to the plates and the convective term contributes almost completely to the turbulent heat transfer in the bulk. Panel (d) of figure 5.24 displays the r.m.s. velocity profiles of the runs with $Ha \leq 1000$. Total fluctuations u_{rms}, which are enhanced at the edge of the boundary layer for $Ha = 0$ due to the detachment of the thermal plumes, are increasingly suppressed by the vertical magnetic field. This is in line with a drop of the global momentum transfer that is measured by the Reynolds number. While the total fluctuations u_{rms}, are significantly larger than the vertical ones w_{rms}, for $Ha = 0$, this ratio decreases steadily as one moves towards the Chandrasekhar limit. It is not only that the fluctuation level decreases as a whole, but also the vertical velocity fluctuations w_{rms} provide an increasing fraction to the total fluctuation magnitude. Furthermore, we find that the ratio of the r.m.s. values taken in the full cell volume, $w_{\mathrm{rms}}/u_{\mathrm{rms}} = 0.55, 0.78, 0.90$ and 0.71 for $Ha = 0$, 200, 500 and 1000 respectively.

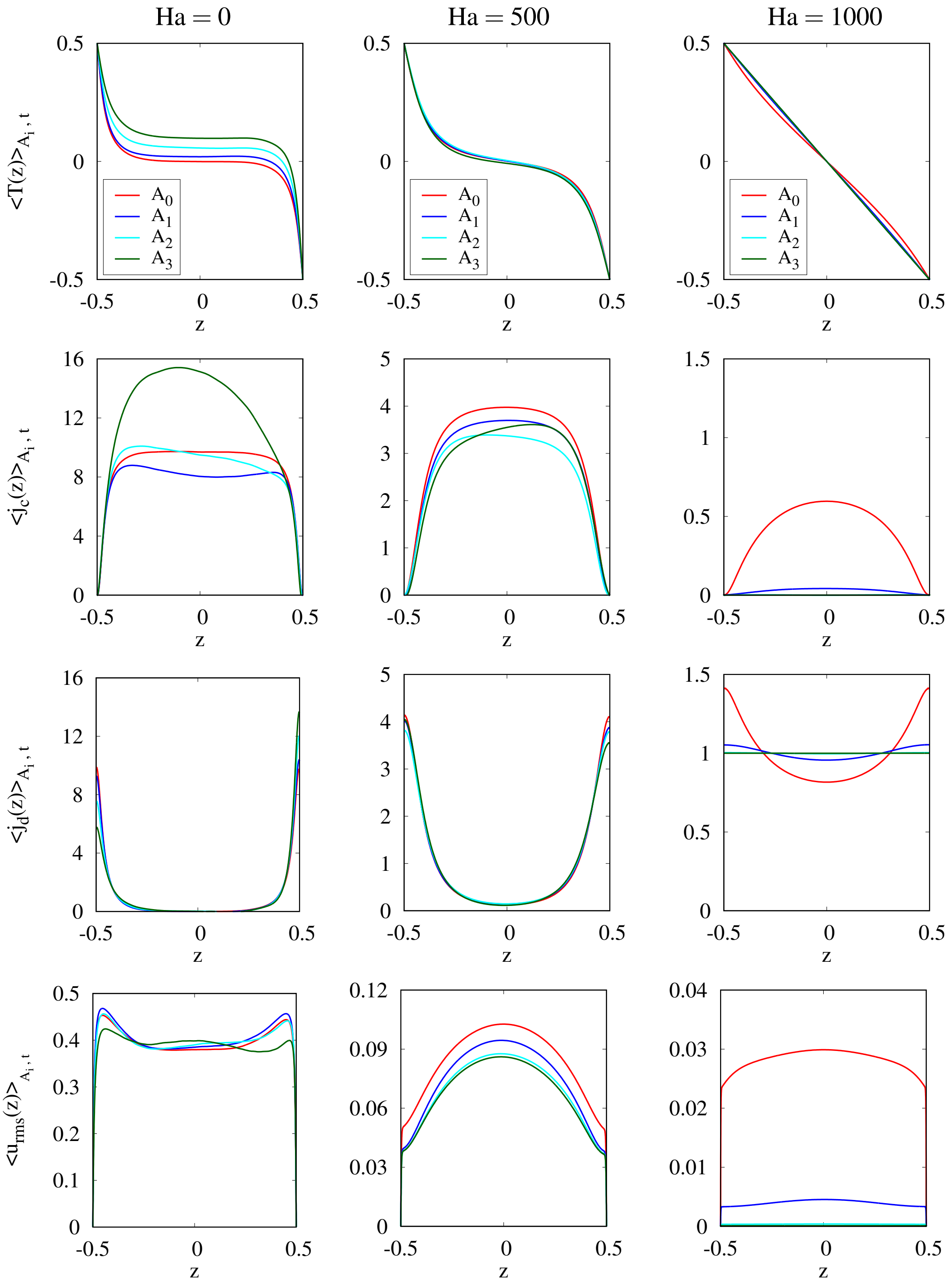

Figure 5.25: Shell analysis of the z-dependent mean profiles of temperature $\langle T(z)\rangle_{A_i,t}$ (first row) , convective flux $\langle j_c(z)\rangle_{A_i,t}$ (second row), diffusive flux $\langle j_d(z)\rangle_{A_i,t}$ (third row), and r.m.s. velocity $\langle u_{rms}(z)\rangle_{A_i,t}$ (last row) for various Hartmann numbers. Columns from left to right stand for $Ha = 0,\ 500,\ 1000$. The average is taken over time span of $31T_f$ and over different area A_i, where $A_i = \{A_0\,, A_1\,, A_2\,, A_3\}$ which are defined in figure 5.23.

5.3.1.3 Spatially refined analysis of turbulent transport

It has been shown that a doubling of the Hartmann number from $Ha = 500$ to 1000 pushes the patterns to the sidewalls. This suggests a scale-refined analysis of the turbulent transport processes. Figure 5.23(d) illustrates how this analysis will be done in detail. The panel contains concentric square subareas A_1, A_2, and A_3 that are nested in each other and take 9/16, 1/4, and 1/16 of A_0, respectively. A_0 denotes for the entire cross-section area. In the following the analysis of the turbulent transport is repeated in these successively smaller cross sections. The results are shown in figure 5.25. We display again profiles of the mean temperature, the convective and diffusive heat current, as well as the r.m.s. velocity (see also figure 5.24 for comparison). It is also noted that the ranges of the profiles differs significantly from one run to another. We cannot choose unique ranges and display the differences in the shells. For $Ha = 0$, it is observed that the temperature in the middle is enhanced which is traced back to the particular mean convection pattern (see figure 5.23(a)). This is in line with an enhanced convective heat flux in the cell center as shown in the left panel of the second row. The intermediate Hartmann number run at $Ha = 500$ display only mild variations in the mean vertical profiles from one shell to another. Similar features are observed for the DNS run at $Ha = 200$, but not shown here. The profiles for the case at $Ha = 1000$ differ to $Ha = 0$ and $Ha = 500$ significantly from shell to shell. It is worth to mention that the mean temperature profile taken for A_3 is almost perfectly a straight line for the case at $Ha = 1000$, which would stand for a purely diffusive transport. This behavior is in line with a strong suppression of the r.m.s. velocity amplitudes in the cell center. For the run at the Chandrasekhar limit we can thus confirm the observations from before. This small amount of existing convective heat transfer is expelled from the interior to the side wall regions. Near wall circulation rolls are the ones the carry the heat from the bottom to the top.

5.3.1.4 Dissipation rates

The vertical profiles of the plane-time averages of kinetic energy dissipation and thermal dissipation rate fields are plotted in figure 5.26. They are denoted by $\varepsilon_T(z) = <\varepsilon_T>_{A,t}$ and $\varepsilon(z) = <\varepsilon>_{A,t}$ respectively. The thermal dissipation rate field and kinetic energy dissipation rate field are defined as equation (2.55) and (2.53) respectively. The profiles show that both thermal and kinetic energy dissipation rates decrease in magnitude as the Hartmann number increases. The results have to be a consequence of diminished derivatives by the magnetic field. Comparing panel (a) and (b) of figure 5.26, we could see that for non-MHD case, thermal dissipation dominates in the boundary

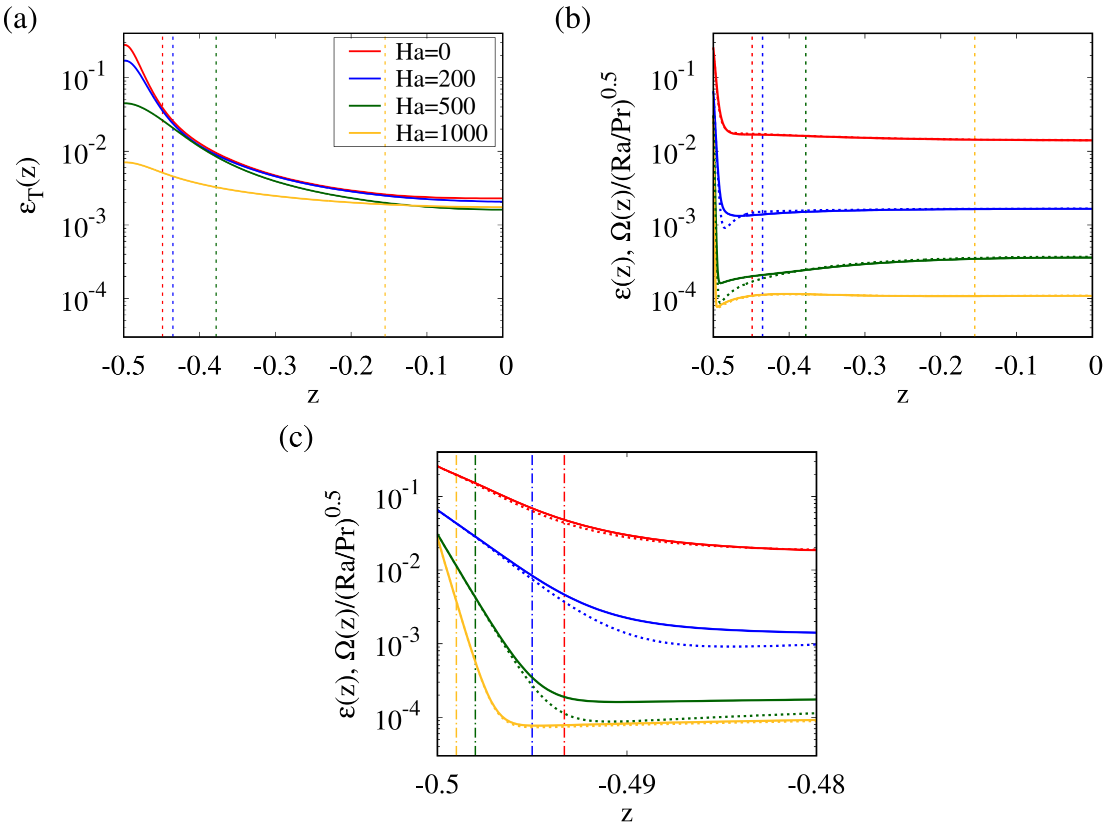

Figure 5.26: Results for $Pr = 0.025$, $Ra = 10^7$, $\Gamma = 4:4:1$ and $0 \leq Ha \leq 1000$. Energy dissipation rate profiles for various Hartmann numbers: (a) the thermal dissipation rate $\varepsilon_T(z)$; (b) the kinetic energy dissipation rate $\varepsilon(z)$. The dashed lines in (b) are the rescaled local enstrophy profiles. The vertical dashed lines in panel (a) and (b) denote the thermal boundary layer thicknesses $\delta_T = 1/(2Nu)$. (c) A zoom in of kinetic energy dissipation rate to the boundaries. The dot–dashed lines denote the velocity boundary layer thicknesses $\delta_{Ha} = 1/Ha$ ($Ha \neq 0$). All profiles are additionally averaged over the lower and upper halves of the cell.

layers while kinetic energy dissipation dominates in the bulk which is in a line with the results shown by Scheel & Schumacher [2016]. For the magnetoconvection case, thermal dissipation dominated both in the boundary layers and in the bulk.

Besides, we compare the vertical mean profile of the kinetic energy dissipation rate $\varepsilon(z)$ and the rescaled local enstrophy $\Omega(z)/\sqrt{Ra/Pr}$ in panel (b) and (c) of figure 5.26. Ω is the local enstrophy which can be defined by means of the vorticity field $\omega_i(\boldsymbol{x},t) = \varepsilon_{ijk}\partial_j u_k$ with $i,j,k = 1,2,3$ and given by $\Omega = \omega_i(\boldsymbol{x},t)\omega_i(\boldsymbol{x},t)$. In homogeneous isotropic turbulence the ensemble average of the mean dissipation and the local enstrophy are connected by an exact relation which translates in our units into $<\varepsilon>=<\Omega/\sqrt{Ra/Pr}>$. We observe deviations between the kinetic energy dissipation rate and the rescaled local enstrophy for the runs with moderate vertical magnetic field that of $Ha = 200$ and $Ha = 500$ and the deviations are located between the Hartmann boundary layer and the thermal boundary layer. The results imply that the vertical magnetic field induces anisotropy between the Hartmann boundary layer and the thermal boundary layer. This phenomenon is not observed for the case with higher Hartmann number.

5.3.1.5 Summary and discussion

Three-dimensional turbulent magnetoconvection at a Rayleigh number of $Ra = 10^7$ in liquid gallium at a Prandtl number $Pr = 0.025$ in a closed square cell of aspect ratio $\Gamma = 4 : 4 : 1$ is studied by means of direct numerical simulations. In absence of an external field the flow is fully turbulent with a Rayleigh number of $Ra = 10^7$. The strength of the externally applied vertical homogeneous magnetic field, which is quantified by the Hartmann number Ha, is increased from $Ha = 0$ up to a value $Ha = 10^3$ that brings the turbulent convection flow increasingly closer to the Chandrasekhar limit. By a Fourier analysis, we show that the convection patterns are reorganized with a decreasing characteristic horizontal wavelength as Ha increases. The turbulent heat transfer, which is investigated in concentric square shells, is found to become increasingly heterogeneously distributed with flow modes that are attached to the side walls for the largest values of $Ha = 1000$.

The reorganization of flow structures and the decrease of Nu with Ha has been discussed in transient Reynolds-averaged Navier-Stokes (T-RANS) simulations in square cells of aspect ratio 8:8:1 [Hanjalić & Kenjereš, 2000; Kenjereš & Hanjalić, 2004]. The present work extends these studies by resolving the turbulent fields to their smallest scales. Furthermore, we drive the system towards the Chandrasekhar limit, by doubling the Hartmann number to a vlaue of $Ha = 10^3$ in comparison to Kenjereš & Hanjalić [2004]. Our present work adds also high-Rayleigh-number DNS data to the $Ha - Ra$ parameter plane. Such data are necessary in an adaption of the Grossmann-Lohse theory of turbulent heat and momentum transfer [Grossmann & Lohse, 2000, 2001] to the case of magnetoconvection that was developed recently by Zürner *et al.* [2016]. This extension will be discussed in brief in section 5.4.

5.3.2 Wall modes beyond the Chandrasekhar limit

We move on to show our DNS results of the turbulent liquid metal convection under effects of a strong vertical magnetic field which is increased beyond the Chandrasekhar limit. Therefore DNS runs 4-4 to 4-6 in series 4 (table 5.1) are considered. The aspect ratio is $\Gamma = 4 : 4 : 1$ and the Prandtl number is fixed to $Pr = 0.025$, the Rayleigh number to $Ra = 10^7$. The linear stability limit is reached at $Ha_c \approx \sqrt{Ra}/\pi \approx 1000$ for the chosen Ra and Pr. Our numerical studies show that convective heat transfer is still present for Hartmann numbers up to $Ha = 2Ha_c$. We will demonstrate by a scale-refined analysis in concentric subvolumes that the transport of heat and momentum is maintained by subcritical flow modes which are attached to the sidewalls, similar to rotating Rayleigh-Bénard convection. The spatial organization and structure of these (quasisteady) wall modes will be studied in detail. Results shown in this subsection have been published in the *Journal of Fluid Mechanics* [Liu *et al.*, 2018].

5.3.2.1 Spatial structure of sidewall modes

Figure 5.27 displays snapshots of the velocity field structure of the magnetoconvection flows. Isosurfaces of the vertical velocity component and field lines of the velocity field are shown for runs at $Ha \geq 500$. For small external magnetic field strength, a cellular structure of up- and downwelling flows is observed that fills the entire cell. A sufficiently strong external magnetic field that corresponds here to $Ha \geq 1000$ expels convective motion from the interior of the cell where heat is then transported solely by diffusion. We note that the critical Hartmann number, which corresponds to the Chandrasekhar linear stability limit, is given by $Ha_c = \sqrt{Ra}/\pi \approx 1007$ for the present Rayleigh number of $Ra = 10^7$. Figures 5.27(b)–(d) display the structure of the wall modes, which consist of alternating up- and downwelling flow regions attached to the sidewalls. They correspond to neighboring circulation rolls which do not move along the sidewalls or oscillate as in rotating convection for the total integration times that we could run the simulations. The wall modes are ever closer attached to the sidewalls as Ha grows from 1000 to 2000. Interestingly, vertical velocity maxima reach out into the bulk in form of tongue-like filaments which might be a relic from the turbulent flow pattern, a point that will be analysed more closely in subsection 5.3.3.3. In order to illustrate that fluid motion is not completely absent in the bulk, we also plot horizontal mid-plane of vertical velocity component u_z as the magnitude in decadic logarithm as shown in figure 5.28.

5.3.2.2 Global and near-sidewall transport of heat and momentum

Table 5.1 shows that the Nusselt number is still larger unity for runs 4-4 to 4-6 beyond the Chandrasekhar limit. With growing Ha the global transport converges to the pure diffusion case at $Nu = 1$. The strong temporal velocity fluctuations of the highly inertial low–Pr turbulence for absent or weak magnetic fields decrease then to vanishingly small values and result in a practically quasisteady laminar wall mode flow. The global analysis of transport is refined in figure 5.29 by vertical mean profiles taken with respect to horizontal plane $A = \Gamma^2$ and time, $\langle\cdot\rangle_{A,t}$. Figure 5.24(a) has already shown the temperature profiles for all six data sets in series 4 that the well-mixed bulk

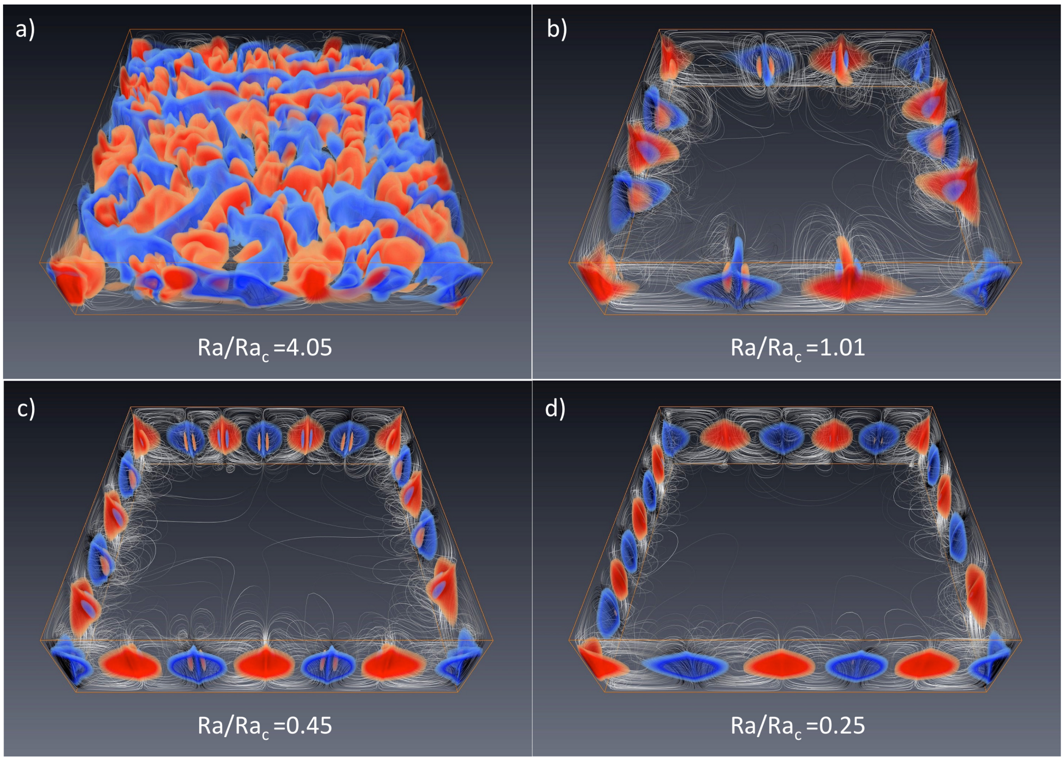

Figure 5.27: (Published in Liu *et al.* [2018]) Snapshots of the magnetoconvection flow at (a) $Ha = 500$. (b) $Ha = 1000$. (c) $Ha = 1500$. (d) $Ha = 2000$. We display isosurfaces of $u_z = \pm 0.01$ together with field lines of the velocity field that highlight the circulation rolls at the sidewalls. The ratio Ra/Ra_c is indicated in each of the panels with $Ra_\mathrm{c} = \pi^2 Ha^2$. For ratios of $Ra/Ra_\mathrm{c} < 1$ the linear stability theory predicts a purely diffusive transport in a fluid layer with $\boldsymbol{u} = 0$.

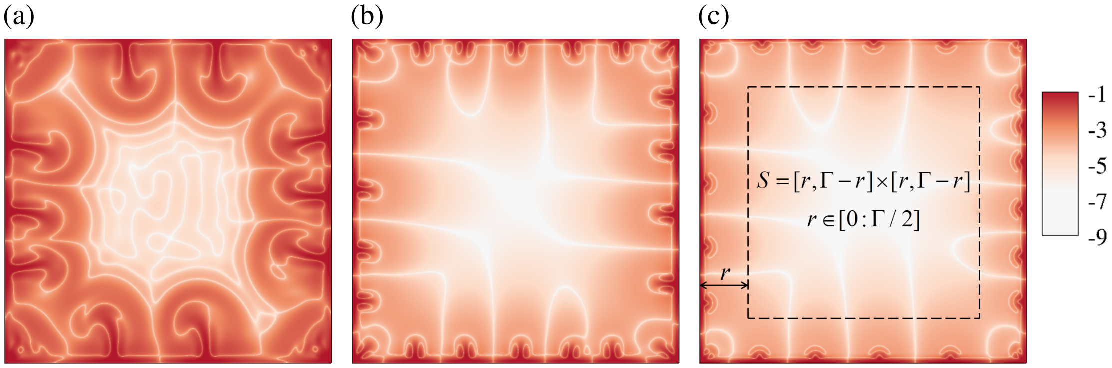

Figure 5.28: Contour plot of the time-averaged vertical velocity component magnitude (in units of decadic logarithm) for $Ha = 1000, 1500, 2000$, i.e., $\langle \log_{10} |u_z(x, y, 0)| \rangle_t$. Data are taken in the horizontal midplane.

region for the turbulent cases at $Ha < 1000$ changes to an almost linear diffusion-dominated profile for $Ha \geq 1000$. Here figure 5.29(a) displays the profiles of the convective heat fluxes $j_\mathrm{c}(z)$ and the diffusive heat fluxes $j_\mathrm{d}(z)$ for the three runs with $Ha \geq 1000$ as well as their sum (which has to be constant and equal to Nu). Definition refers to equation 5.2. It is seen that $j_\mathrm{d}(z) > j_\mathrm{c}(z)$ for all $z \in [-0.5, 0.5]$, showing

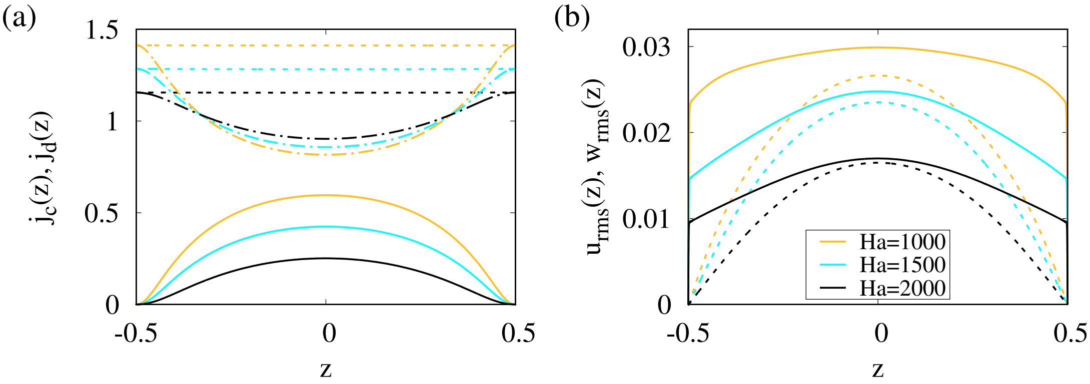

Figure 5.29: (Published in Liu *et al.* [2018]) Results for $Pr = 0.025$, $Ra = 10^7$, $\Gamma = 4:4:1$ and $1000 \leq Ha \leq 2000$. (a) Mean profiles of convective heat current, $j_c(z)$ (solid lines), and diffusive heat current, $j_d(z)$ (dash-dotted lines) for various Hartmann numbers. Both currents are defined in equation (5.2). The dotted lines in (a) correspond to $Nu(z) = j_c(z) + j_d(z) = const$. (b) Mean profile of the root-mean-square (rms) for the full velocity field (solid line) and the vertical velocity component (dashed line).

that diffusive term dominates throughout the whole layer. The increasing suppression of fluid turbulence is also demonstrated in figure 5.29(b) by the *r.m.s* velocity profiles which are given for the *quasisteady* cases for $Ha \geq 1000$ by $u_{\mathrm{rms}}(z) = \langle u_x^2 + u_y^2 + u_z^2 \rangle_A^{1/2}$ and $w_{\mathrm{rms}}(z) = \langle u_z^2 \rangle_A^{1/2}$. It is not only that total fluctuation level decreases then as a whole, but also that the vertical velocity fluctuations provide an increasing fraction to the total fluctuation magnitude for $Ha \geq Ha_c$. The ratio of the root mean square values taken in the full cell volume, $w_{\mathrm{rms}}/u_{\mathrm{rms}} = 0.71, 0.82$, and 0.83 for $Ha = 1000, 1500$ and 2000.

The importance of the wall modes for the transport of heat and momentum beyond the Chandrasekhar limit is highlighted in figure 5.30 where we determine Nusselt number and root mean square velocities over successively smaller concentric cross section areas $S = [r,\ \Gamma - r] \times [r,\ \Gamma - r]$ with r being the sidewall-normal distance. The definition of S is presented in figure 5.28(c). These averages are indicated by $\langle \cdot \rangle_S$. As visible in figure 5.30, the transport decreases significantly within a few Shercliff layer thicknesses $\delta_{\mathrm{Sh}} = 1/\sqrt{Ha}$ thus further supports the hypothesis that the transport for $Ha > Ha_c$ is connected to the wall modes. It is also seen that the heat transfer drops to the diffusive lower bound of $Nu = 1$ for $r \gtrsim 2\delta_{\mathrm{Sh}}$ for the highest Hartmann number. All velocity profiles drop significantly towards the center of the cell.

5.3.2.3 Wall-mode structure together with thermal and Shercliff boundary layers

We proceed with an analysis of the viscous and thermal boundary layers in conjunction with the wall-modes. In table 5.2, we list all important boundary layer thicknesses.

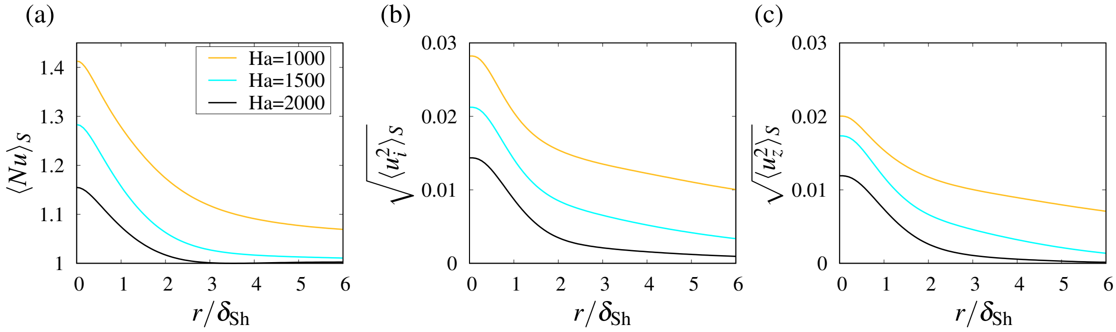

Figure 5.30: (Published in Liu *et al.* [2018]) Near-sidewall transport of heat and momentum beyond the Chandrasekhar stability limit. Nusselt number and root mean square velocities are determined over successively smaller horizontal cross section S. Profiles are plotted versus a sidewall-normal distance r in units of the Shercliff layer thickness δ_{Sh}. (a) Nusselt number $\langle Nu\rangle_S$. (b) Root mean square velocity $\langle u_i^2\rangle_S^{1/2}$=$\langle u_x^2+u_y^2+u_z^2\rangle_S^{1/2}$. (c) Root mean square vertical velocity component $\langle u_z^2\rangle_S^{1/2}$. Data are $Ha = 1000, 1500$ and 2000 as indicated in (a).

The thermal boundary layer thickness $\delta_T = 1/(2Nu)$ at the top and bottom approaches 0.5 in agreement with $Nu \to 1$ as Ha grows. The mean thermal boundary layer thickness at the sidewall, $\delta_T^{(\mathrm{sw})}$ is obtained from profiles of the temperature fluctuations, $\theta(\boldsymbol{x},t) = T(\boldsymbol{x},t) - \langle T(z)\rangle_{A,t}$, with respect to the sidewall-normal coordinate r. These profiles are calculated for $Ha \geq 1000$ only, i.e., when the dominantly vertical up- and down-flows are attached to the sidewalls. They are always obtained as an average over all four sidewalls. The value of $\delta_T^{(\mathrm{sw})}$ is determined by a standard slope method, i.e., as the intersection point of the horizontal line drawn through the mean value of $\langle\theta(r)\rangle_{\mathrm{sw}}$ in the bulk and a tangent which is fitted to the same profile very close to the sidewall. The corresponding values decrease as Ha grows and are given in table 5.2.

In the presence of a strong B_0, the standard viscous boundary layer thickness δ_ν has to be substituted by the Hartmann layer thickness $\delta_{\mathrm{Ha}} = 1/Ha$ at the top and bottom. As seen in table 5.2, the Hartmann layers become extremely thin and their appropriate resolution makes these DNS very demanding. The viscous sidewall layers are also affected by the external magnetic field. Here the fluid motion in horizontal (x,y)-directions, i.e. transverse to the sidewall-parallel magnetic field, is affected and Shercliff layers with thickness δ_{Sh} are formed. The Shercliff thickness will be chosen as the length-scale in which the wall modes are measured. The latter ones establish a complex flow structure at the sidewalls which is quantified in figure 5.31 for the highest external field at $Ha = 2000$. We observe the alternating up- and down-flows of warmer and colder fluid, respectively (see figure 5.31(a,b)). The tongue-like structure consists of three thin counter-flowing jets (up-down-upwelling or down-up-downwelling) which arise due to the incompressibility condition (see figures 5.31(b) and 5.27). The velocity amplitude inside the modes is still remarkably large with a maximum of $u_z \sim 0.1$ as seen in figure 5.31(d).

Run	Ha	δ_T	$\delta_T^{(\mathrm{sw})}$	δ_{Ha}	δ_{Sh}	$\delta_T^{(\mathrm{sw})}/\delta_{\mathrm{Sh}}$	$r_{\mathrm{cr}}/\delta_{\mathrm{Sh}}$	β/N
1	0	0.051	–	∞	∞	–	–	–
2	200	0.065	–	0.005	0.071	–	–	–
3	500	0.122	–	0.002	0.045	–	–	–
4	1000	0.355	0.338	0.0010	0.032	10.69	3.46	0.30
5	1500	0.391	0.260	0.0007	0.026	10.07	3.46	0.30
6	2000	0.435	0.227	0.0005	0.022	10.15	3.47	0.30

Table 5.2: (Published in Liu *et al.* [2018]) Summarizing list of different boundary layer thicknesses which can be obtained in the magnetoconvection flow in a closed cell. We list thermal boundary layer thicknesses at top/bottom and sidewalls as well as Hartmann and Shercliff layer thicknesses. For the runs with wall modes we also list the ratios $r_{\mathrm{cr}}/\delta_{\mathrm{Sh}}$ and β/N to quantify a two-layer structure. Here, r_{cr} is the crossover width of the two spatial decays laws of convective heat flux of the wall modes. The exponential decay of the inner layer is measured by exponent β which is found in a fixed ratio to the corresponding interaction parameter (or Stuart number) $N = Ha^2/\sqrt{Ra/Pr}$.

Figures 5.31(b,c) shows a two-layer structure of the wall modes on the basis of the vertical velocity component and heat transport. Figure 5.32 supports this observation further by an analysis of the convective heat transfer $\langle Nu\rangle_S - 1 = \sqrt{RaPr}\langle u_z T\rangle_S$ (see also figure 5.30(a)). For all runs at $Ha \geq 1000$, two exponential decays laws can be observed. These decays separate two different layers: the bulk region dominated by diffusive heat transport and the inner near-wall region with residual convective flow motion, particularly well observable at the highest $Ha = 2000$. We have verified that the pronounced minimum at this largest Hartmann number persists for finer computational grids by shorter test reruns at higher resolutions. The crossover distance r_{cr}, identified as the intersection point of both exponential fits, is found at a fixed ratio to the Shercliff layer thickness δ_{Sh} for the three runs, as given in the table 5.2. This result implies that the inner section of the sidewall layer is on average of Shercliff-type despite the alternating pattern of horizontal up- and downflows. The distance r_{cr} matches the point where the thin tongue-like vertical flows in figure 5.31(b,c) appear. Interestingly, the exponential fit $Nu - 1 \approx A \times \exp(-\beta r)$ of the inner sublayer for $r \leq r_{\mathrm{cr}}$ results in spatial decay rates β being a fixed ratio to the interaction parameter (or Stuart number) $N = Ha^2/\sqrt{Ra/Pr}$. This parameter relates Lorentz to inertial forces and, in the present DNS series, underlines the dominance of Lorentz forces at $Ha \geq 1000$.

5.3.2.4 Summary and discussion

We have studied three-dimensional magnetoconvection in a closed rectangular cell under the influence of a strong external vertical magnetic field B_0. An increase of

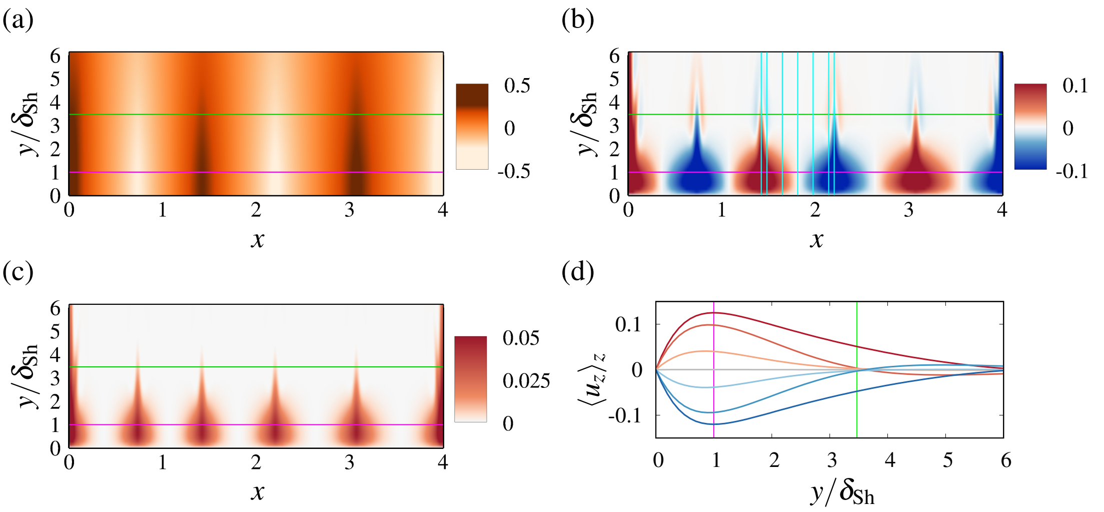

Figure 5.31: (Published in Liu *et al.* [2018]) Detailed structure of the wall modes at $Ha = 2000$. Horizontal cross section of the time-averaged (a) temperature field T, (b) vertical velocity component u_z and (c) heat transport $u_z T$ at the mid-plane ($z = 0$). The violet horizontal line indicates Shercliff boundary layer thickness δ_{Sh}. The green horizontal line indicates $r_{\mathrm{cr}} = 3.47\delta_{\mathrm{Sh}}$. Sidewall distance r_{cr} is determined in figure 5.32. (d) Profiles of vertical velocity component versus the wall y-distance are taken at seven x-positions indicated by the cyan vertical lines in panel (b). Profiles from red to blue via grey correspond to the cyan lines from left to right. The vertical velocity component is averaged over the whole cell height in these profiles.

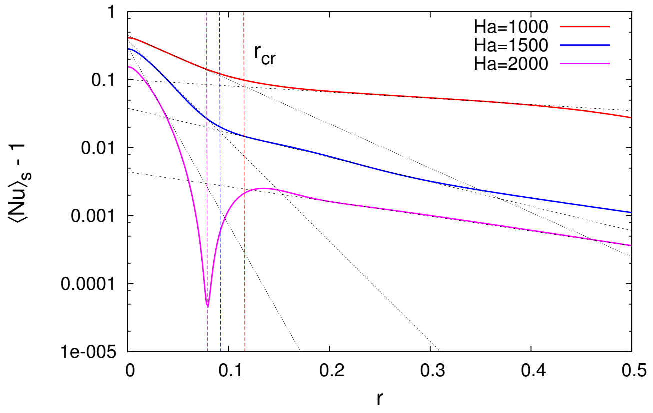

Figure 5.32: (Published in Liu *et al.* [2018]) Two-layer structure of the wall modes. The global convective heat flux $Nu - 1$ taken over cross sections S is plotted with respect to the sidewall-normal coordinate r is plotted for $Ha \geq 1000$. The spatial exponential decay with r is fitted by two separate scaling laws which intersect at $r = r_{\mathrm{cr}}$.

the magnetic field strength, which is measured by an increasing Hartmann number Ha, suppresses the highly turbulent motion of the enclosed liquid metal at $B_0 = 0$ ever stronger. In a close analogy to rotating Rayleigh-Bénard convection, we find (laminar) sidewall modes that continue to exist for magnetic fields with $Ha > Ha_c$. For the present set of simulations, we were able to follow these wall modes up to $Ha = 2Ha_c$. A further increase of the Hartmann number would require even finer mesh resolutions at the sidewalls. It is planned to ramp up these simulations for higher Hartmann numbers in the future.

A splitted jet or sandwich-type structure was seen in the linearly unstable modes of Houchens *et al.* [2002]. Our present simulations revealed this double-layer structure of the wall modes and show that it scales with the Shercliff layer thickness. This again is similar to the boundary thicknesses near the sidewall in the rotating convection case where wall modes were found to be related to Stewartson layers that scale with Ekman number [Kunnen *et al.*, 2013, 2011]. We did not observe a drift of the wall modes which was observed in rotating RBC with different cell geometries [Horn & Schmid, 2017; Knobloch, 1998; Vasil *et al.*, 2008] and can be traced back to a breaking of azimuthal reflection symmetry [Ecke *et al.*, 1992]. It remains open which symmetry-breaking bifurcation could be at work for the convection flow in the presence of a strong magnetic field. The absence of a drift in our DNS might be attributed to the relatively short total integration time of 31 free fall time units which is a small fraction of the momentum diffusion time scale – the slowest time in our flow on the basis of characteristic system parameters. At $Ra = 10^7$ and $Pr = 0.025$ this results to $t_{\mathrm{vis}} = \sqrt{Ra/Pr}\,T_f = 2 \times 10^4 T_f$. Indeed, at Hartmann numbers of $Ha \geq 1000$, magnetoconvection becomes a very slow dynamical process and numerical studies would require extremely long-term runs of this order of magnitude.

Our present numerical findings for the existence of wall modes are consistent with the predictions by Houchens *et al.* [2002] and Busse [2008] for the Hartmann number $\overline{Ha}_c$ at which the convection should be completely ceased in a closed cell. For $Ra = 10^7$, this gives $\overline{Ha}_c = (Ra/68.25)^{2/3} \approx 2777$ if the asymptotic solution of Houchens *et al.* [2002] is taken from their closed cylindrical cell with $\Gamma = 1$. From the asymptotic theory of Busse [2008] that applies free-slip boundary conditions at the top and bottom plates follows $\overline{Ha}_c = (Ra/(3\pi^2\sqrt{3\pi/2}))^{2/3} \approx 2890$. Both theoretical approaches suggest thresholds that are still larger than the Hartmann number which could be obtained here. This should however be possible in a simulations which we plan to conduct in the near future, as already stated.

The observed wall modes resemble also an interesting similarity to isolated turbulent spots in the Shercliff layers in MHD pipe and duct flows at the edge of relaminarization [Krasnov *et al.*, 2013; Zikanov *et al.*, 2014*a*]. Despite one major difference – the present system is linearly unstable in contrast to pipe and square duct flows – both cases lead to the development of residual structures that maintain a transport of heat and momentum. They are formed in thin near-wall zones, whereas the rest of the domain remains essentially unperturbed. Similar to MHD duct and pipe flows, wall modes are rather weak and, thus, difficult to identify in experiments if only integral parameters can be measured as discussed by Krasnov *et al.* [2013]. These modes provide virtually no impact on the vertical temperature distribution and the Nusselt number only slightly differs from the lower diffusive bound. These similarities suggest that the residual sidewall structures are very likely a common feature of MHD wall bounded flows subject to strong external magnetic fields.

5.4 An extension of Grossmann and Lohse theory to magnetoconvection in a vertical magnetic field

Grossmann and Lohse (GL) theory [Grossmann & Lohse, 2000, 2001] is an unifying scaling theory for the heat and momentum transport in turbulent Rayleigh-Bénard convection, which describes $Nu(Ra,\ Pr)$ and $Re(Ra,\ Pr)$. The central idea of the GL theory is a decomposition of the dissipation rates into contributions from the bulk and the boundary layers in the vicinity of the plates. These contributions have to be weighted with the volume fractions that are occupied by the boundary layers of the temperature and velocity fields. An extension of GL theory to the case of quasistatic magnetoconvection in the presence of a (strong) constant vertical magnetic field B_0 was developed by our co-worker Zürner *et al.* [2016]. The extension aimed at predicting the functional dependence $Nu(Ra,\ Pr,\ Ha)$ and $Re(Ra,\ Pr,\ Ha)$ in the limit of low Prandtl number Pr and low magnetic Prandtl number Pr_m.

To make this thesis self-contained, we briefly recapitulate the key approach to extend the GL theory to magnetoconvection. Following the idea of GL theory, the kinetic energy dissipation rate $\varepsilon(\boldsymbol{x},t) = \frac{\nu}{2}(\partial_i u_j + \partial_j u_i)^2$, the magnetic dissipation rate $\varepsilon_B(\boldsymbol{x},t) = \frac{\eta}{2\mu_0\rho_0}(\partial_i b_j + \partial_j b_i)^2$ and the thermal dissipation rate $\varepsilon_T(\boldsymbol{x},t) = \kappa(\partial_i T)^2$ are decomposed into respective bulk contribution and boundary layer (BL) contributions:

$$\varepsilon = \varepsilon_{bulk} + \varepsilon_{BL}\,, \tag{5.6}$$

$$\varepsilon_B = \varepsilon_{B,bulk} + \varepsilon_{B,BL}\,, \tag{5.7}$$

$$\varepsilon_T = \varepsilon_{T,bulk} + \varepsilon_{T,BL}\,. \tag{5.8}$$

The globally averaged dissipation rates (left-hand sides of equations (5.6-5.8)) follow the exact scaling laws:

$$\varepsilon + \varepsilon_B = \frac{\nu^3}{H^4}\frac{(Nu-1)Ra}{Pr^2}\,, \tag{5.9}$$

$$\varepsilon_T = \kappa\frac{(\Delta T)^2}{H^2}Nu \tag{5.10}$$

The six contributions to the dissipation rates (right-hand of equations (5.6-5.8)) can be estimated as follows:

$$\varepsilon_{bulk} \sim \frac{U^3}{H} = \frac{\nu^3}{H^4} Re^3 \,, \tag{5.11}$$

$$\varepsilon_{BL} \sim \nu \frac{U^2}{\delta_\nu^2} \frac{\delta_\nu}{H} = \frac{\nu^3}{H^4} Re^2 Ha \,, \tag{5.12}$$

$$\varepsilon_{B,bulk} \sim \frac{\eta}{\mu \rho_0} \frac{Rm^2 B_0^2}{H^2} = \frac{\nu^3}{H^4} Re^2 Ha^2 \,, \tag{5.13}$$

$$\varepsilon_{B,BL} \sim \frac{\eta}{\mu \rho_0} \frac{Rm^2 B_0^2}{\delta_\nu^2} \frac{\delta_\nu}{H} = \frac{\nu^3}{H^4} Re^2 Ha^3 \,, \tag{5.14}$$

$$\varepsilon_{T,bulk} \sim \frac{(\Delta T)^2 U}{H} = \kappa \frac{(\Delta T)^2}{H^2} Re Pr \,, \tag{5.15}$$

$$\varepsilon_{T,BL} \sim \kappa \frac{(\Delta T)^2}{\delta_T^2} \frac{\delta_T}{H} = \kappa \frac{(\Delta T)^2}{H^2} \sqrt{Re Pr} \,. \tag{5.16}$$

The thickness of thermal BL remains $\delta_T = H/(2Nu)$ and the thickness of kinetic BL is that of the Hartmann layers $\delta_\nu = H/Ha$. Changes in these scaling laws due to different flow regimes are accounted by crossover functions. The regime transitions considered in this model are: (i) the nesting of the thermal BL either inside or outside the kinetic BL, (ii) the transition to a fully turbulent bulk flow near a Reynolds number Re^* and (iii) the onset of convection at Ra_c, where Ra_c is the critical Rayleigh number scales as $Ra_c = \pi^2 Ha^2$ [Chandrasekhar, 1961]. Combination of these scaling laws and crossover functions leads to the following two model equations:

$$\frac{(Nu-1)Ra}{Pr^2 h(Ra/Ra_c)} = c_1 \zeta^3 g\left(\frac{\zeta}{Re^*}\right) + c_2 \zeta^2 Ha + c_3 \zeta^2 Ha^2 + c_4 \zeta^2 Ha^3 \,, \tag{5.17}$$

with

$$\zeta = \frac{\left(\sqrt{c_6^2 + \dfrac{4c_5(Nu-1)}{h(Ra/Ra_c)}} - c_6\right)^2}{4c_5^2 Pr f\left(\dfrac{2Nu}{Ha}\right)} \,.$$

and

$$Re = \frac{\left(\sqrt{c_6^2 + 4c_5(Nu-1)} - c_6\right)^2}{4c_5^2 Pr f\left(\dfrac{2Nu}{Ha}\right)} \,. \tag{5.18}$$

f, g and h are the crossover functions mentioned above which are relatively defined as $f(x_T) = (1 + x_T^n)^{-1/n}$ with the argument $x_T = \delta_\nu/\delta_T = 2Nu/Ha$ and $n = 4$, $g(x^*) =$

$1/f(1/x^*)$ with the argument $x^* = Re/Re^*$ and $h(x_c) = 1 - f(x_c)$, where $x_c = Ra/Ra_c$. c_1 to c_6 are the coefficients that give the absolute magnitude of the local scaling laws. These parameters together with Re^* are *a priori* unknown model parameters which have to be determined from a data record. Once the model parameters are fixed, the model equations (5.17) and (5.18) can be solved to obtain the expressions $Nu = Nu(Ra, Ha, Pr)$ and $Re = Re(Ra, Pr, Ha)$.

In order to fix the model parameters c_1 to c_6 and Re^*, at least one data record (Nu, Re, Ra, Ha, Pr) which includes the Reynolds number is needed. However, to the best of our knowledge, there are no publications that report data sets including Re. Therefore, the DNS of this work are necessary to provide at least one operating point for evaluating the model parameters.

In Zürner *et al.* [2016], the model equations has been fitted based on our DNS with the relatively low Rayleigh number $Ra \leq 10^6$ and existing experimenral data by Cioni *et al.* [2000], which is the only experiment that was operated at a sufficiently high Rayleigh number. The resulting optimal parameters were $c_1 = 0.053$, $c_2 = -2.4$, $c_3 = 0.014$, $c_4 = -3.7 \times 10^{-6}$, $c_5 = 0.0038$, $c_6 = 0.48$ and $Re^* = 56000$. Here we add high-Rayleigh-number DNS dataset and get a new set of optimal model parameters which are $c_1 = 0.024$, $c_2 = -1.4$, $c_3 = 0.0081$, $c_4 = -2.2 \times 10^{-6}$, $c_5 = 0.0029$, $c_6 = 0.42$ and $Re^* = 73000$. The experimental data as well the DNS data have been obtained for convection at a Prandtl number of $Pr = 0.025$ and the fixed Pr leads the scaling expressions to $Nu = Nu(Ra, Ha)$ and $Re = Re(Ra, Ha)$. Figure 5.33 display Nu as a function of Ra for three fixed Ha and for $Pr = 0.025$. The profiles in panel (a) present the results based on the old model parameters [Zürner *et al.*, 2016] and the curves in panel (b) show the results based on the new model parameters. It is shown that, the theory results fits to the experiments much better after adding the high-Rayleigh-number DNS dataset.

Figure 5.34 shows the $Ra - Ha$ phase diagrams for Nu and Re calculated with the new parameter values. Comparing to the one published in [Zürner *et al.*, 2016], the general features remain the same. The diagonal line labeled $Ra = \pi^2 Ha^2$ displays the Chandrasekhar linear stability limit of the onset of convection, above which the fluid is in a purely diffusive state without convective flow, i.e. $Nu = 1$ and $Re = 0$. Furthermore, the line is displayed for which $\delta_v = \delta_T$. Above this line the Hartmann layer thickness will be smaller as the thermal boundary layer thickness. This characteristic line is crossed by a second line that shows $Re = Re^*$. On the left side of this line the convection flow is not fully developed turbulent, but in weakly nonlinear and time-dependent convection state. All data which are to the right of this line can be considered as fully turbulent convection data. The parameter space below the

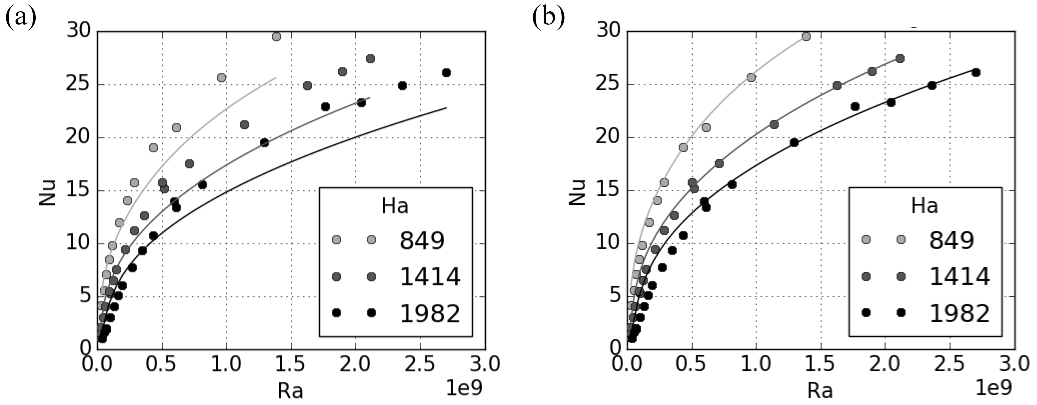

Figure 5.33: Nu vs Ra for three fixed Ha for $Pr = 0.025$. The solid lines show the results based on the extended GL theory with the model parameters (a) fitted with the low-Rayleigh-number DNS dataset and (b) fitted with the high-Rayleigh-number DNS dataset. The points show the data from the experiments by Cioni *et al.* [2000].

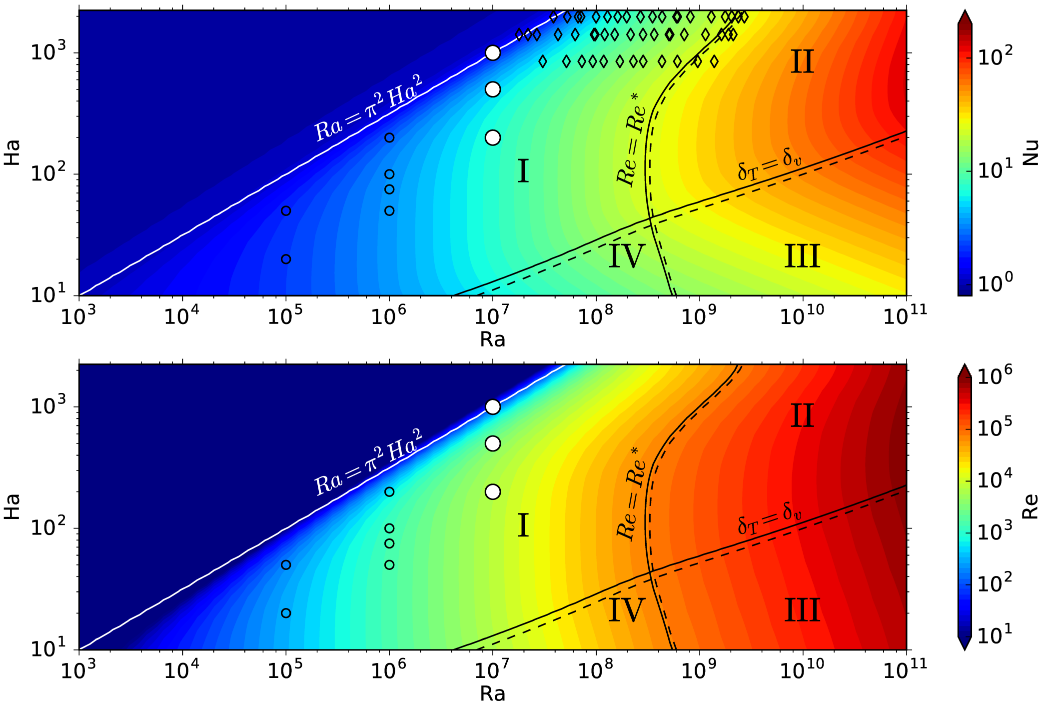

Figure 5.34: Phase diagrams of Nu and Re on the Ra-Ha-plane for $Pr = 0.025$. The symbols represent the data of our numerical simulations (circles) and the experiments by Cioni et. al. Cioni *et al.* [2000] (diamonds) used for fitting the model parameters. The lines in the diagrams mark the position of the crossovers introduced in the model: Below $\delta_T = \delta_v$ the scaling of the thermal BL dissipation changes, $Re = Re^*$ marks the scaling transition from a weakly nonlinear to turbulent bulk flow and $Ra = \pi^2 Ha^2$ indicates the onset of convection. Regimes I to IV are marked as described in the text. Dashed lines denote the results based on the low-Rayleigh-number DNS dataset in a cubic box.

Chandrasekhar limit splits into four subregions by the lines $\delta_v = \delta_T$ and $Re = Re^*$: (I) weakly nonlinear flow and strong magnetic field, (II) fully developed turbulent flow and strong magnetic field, (III) fully developed turbulent flow and weaker magnetic field and (IV) weakly nonlinear flow and weaker magnetic field.

In contrast to standard Rayleigh-Bénard convection, the database used for fitting the model parameters in magnetoconvection is very small. As shown in figure 5.34, most of the data are placed in regime I with a few of the experimental data reaching regime II. Regimes III and IV do not contain any data points. Therefore, more data are required to make more precise predictions of GL theory for magnetoconvection. These efforts are currently under way with new laboratory experiments by our co-worker Zürner et al. Additional numerical simulations are also planned in the near future.

Chapter 6

Conclusion and Outlook

We have conducted series direct numerical simulations to study three-dimensional turbulent Rayleigh-Bénard magnetoconvection in liquid metal at a fixed Prandtl number of $Pr = 0.025$ in closed rectangular cells with different aspect ratios. Our setting is the quasistatic or low-Re_m limit. Two representative systems have been investigated, that of turbulent magnetoconvection in an external constant horizontal magnetic field and in an external constant vertical magnetic field. It was investigated in detail how the turbulent heat and momentum transfer is affected and how the structures are reorganized by the external magnetic field.

For the system with an external horizontal magnetic field, turbulent Rayleigh-Bénard convection at a Rayleigh number of $Ra = 10^6$ in closed cells with two different geometries that a square box with an aspect ratio of $\Gamma = 4:4:1$ and a long rectangular box with $\Gamma = 1:4:1$ are studied. The significant results and outcome are as follows:

In the square box with an aspect ration of $\Gamma = 4:4:1$, different convection pattern regimes which are related to the Hartmann number Ha are identified. At low horizontal magnetic field, the flow regime is large-scale convection without aligned rolls and at sufficiently strong horizontal magnetic field, the flow regime is quasisteady 2D four-roll pattern aligned to the magnetic field. The quasi 2D roll like structure extends the uniform bulk central region of the convection and thins the thermal boundary layers, causing an increase of heat and momentum transfer coefficient. In between, the most remarkable regime that of flow reversals in which four rolls change their circulation direction periodically has been observed. Similar to Yanagisawa *et al.* [2013, 2015] and Tasaka *et al.* [2016], the key regime of the flow reversals is the interaction of between the aligned convection rolls and global horizontal circulation caused by the skewed-varicose instability. The process of flow reversal can be generally described as bending (expanding and shrinking of the rolls), breakdown and reconnection of the convection rolls. However, the detailed procedure may be different for the cases with different strength of magnetic field. Particularly, direction reversals of the driving global horizontal circulation are also detected. The reversal regime also shows an interesting similarity to the large-scale temporal intermittency in the channel flow with spanwise magnetic field which is found at intermediate values of Ha [Boeck *et al.*, 2008].

In the long rectangular box with an aspect ration of $\Gamma = 1 : 4 : 1$ with the external magnetic field parallel to the longest horizontal walls, we also detect different convection patterns dependent on the strengths of the magnetic field. Without magnetic field or with a low magnetic field, the flow pattern shows oscillating rolls with axes normal to the longest side walls. For a sufficiently strong magnetic field, the flow pattern is organized to a quasisteady one-roll structure aligned with the magnetic field, i.e. parallel to the longest side walls. Interestingly, at moderate magnetic field, we observe a long transition period before the aligned one-roll structure established. The flow pattern during the transition period shows a twisted roll structure which consists of two half-vessel-length-scale rolls which have different orientations. The two rolls are aligned with the magnetic field and are quasi 2D except the zone where they connect.

For the system with an external vertical magnetic field, turbulent Rayleigh-Bénard convection at a Rayleigh number of $Ra = 10^6$ in a closed cubic cell with an aspect ratio of $\Gamma = 1 : 1 : 1$ and at a high Rayleigh number of $Ra = 10^7$ in a square box with an aspect ratio of $\Gamma = 4 : 4 : 1$ are mainly reported in this thesis. The significant results and outcome are as follows:

The flow pattern in Rayleigh-Bénard convection that confined in a cube with $Ra = 10^6$ takes the form of a single LSC occupying almost the complete central region with its orientation oscillating in time in the absence of magnetic field. A vertical magnetic field inhibits the oscillation of LSC and thus decreases the heat and momentum transport. As the magnetic field is increasing, the convection tends to be expelled from the interior to the near-wall regions, with the fluid motion almost completely absent in the bulk. We have detected multiple states for equal input parameters due to different initial states, which may influence the heat and momentum transport especially for the runs with moderate vertical magnetic field. For the runs with low magnetic field, we observe an inverse of mean temperature profile in the bulk of the cubic cell which is due to the highly confined small aspect ratio.

The effect of an external vertical magnetic field on heat and momentum transport as well as on the convection structures has been more systemically investigated by the DNS of Rayleigh-Bénard convection at a high Rayleigh number of $Ra = 10^7$ in a square box with an aspect ratio of $\Gamma = 4 : 4 : 1$ with the strength of magnetic field, which is increased from $Ha = 0$ up to a value $Ha = 2000$ such that the confined flow as a whole gets far beyond the Chandrasekhar limit ($Ha_c = 1007$). By a Fourier analysis, we have shown that the convection patterns are reorganized with a decreasing characteristic horizontal wavelength as Ha increases towards the Chandrasekhar limit. The turbulent heat transfer, which is investigated in concentric square shells, is found to become increasingly heterogeneously distributed with flow modes that are attached to the side wall. The sidewall modes, in short wall modes, continue to exist for magnetic fields with $Ha > Ha_\mathrm{c}$ which is in a close analogy to rotating Rayleigh-Bénard convection.

We have conducted a detailed analysis of the wall modes and revealed complex split jet or sandwich-type structures of these wall modes. Their extension into the cell interior results a sidewall boundary layer composition that is found to scale with the Shercliff layer thickness. This again is similar to the boundary thicknesses near the sidewall in the rotating convection case where wall modes were found to be related to Stewartson layers that scale with Ekman number [Kunnen *et al.*, 2013, 2011]. We did not observe a drift of the wall modes which was observed in rotating Rayleigh-Bénard convection with different cell geometries [Horn & Schmid, 2017; Knobloch, 1998; Vasil *et al.*, 2008] and can be traced back to a breaking of azimuthal reflection symmetry [Ecke *et al.*, 1992]. The observed wall modes bear also an interesting similarity to isolated turbulent spots in the Shercliff layers in MHD pipe and duct flows at the edge of relaminarization [Krasnov *et al.*, 2013; Zikanov *et al.*, 2014*a*] suggesting that the residual sidewall structures are very likely a common feature of MHD wall bounded flows subject to strong external magnetic fields.

In the following, we discuss some possible projects which may be investigated in the future upon the present work.

First, concerning the flow reversals in liquid metal convection under influence of a moderate horizontal magnetic field, it would be interesting to perform DNS in larger square boxes to understand better the transition regimes between the patterns, which are difficult to access by experiments. It would be also instructive to check if flow reversals can be detected in a square geometry with periodic side wall boundaries.

Secondly, concerning the observed twisted roll structure in liquid metal convection within a long rectangular geometry with a horizontal magnetic field parallel to the longest sidewalls, it would be helpful to perform DNS in an even longer geometry to better understand the regime behind the twisted structure. It would be also interesting to study the hysteresis behavior of the transition regime between the convection patterns.

Thirdly, concerning the subcritical wall modes in liquid metal convection under effects of a vertical magnetic field, a further increase of the Hartmann number approaching threshold at which the convection should completely cease in a closed cell is necessary to better understand wall modes in magnetoconvection. This requires big simulations that resolve the thin Hartmann and Shercliff layers.

Finally, we have conducted the DNS by considering a constant temperature boundary conditions at top and bottom walls. It would be beneficial to consider a constant heat flux boundary at top and bottom walls especially for the case of magnetoconvection with a vertical magnetic field, where the vertical energy component is expected increasing monotonously as the strength of vertical magnetic field increasing.

Author Publications

LIU, W., KRASNOV, D. & SCHUMACHER, J. 2018 Wall modes in magnetoconvection at high Hartmann numbers. *J. Fluid Mech.* **849**, R2.

LIU, W., KRASNOV, D., SCHUMACHER, J., KARCHER, C. & THESS, A. 2015 DNS of natural convection in liquid metal with strong magnetic fields in rectangular geometry. *Proceedings of the 8th International Conference on Electromagnetic Processing of Materials, Cannes, France* .

LIU, W., KRASNOV, D., SCHUMACHER, J., KARCHER, C. & THESS, A. 2016 DNS of natural convection in liquid metal with strong magnetic fields in rectangular enclosures. *Proceedings of the 10th PAMIR International Conference Fundamental and Applied MHD, Cagliari, Italy* .

ZÜRNER, T., LIU, W., KRASNOV, D. & SCHUMACHER, J. 2016 Heat and momentum transfer for magnetoconvection in a vertical external magnetic field. *Phys. Rev. E* **94** (4), 043108.

References

AHLERS, G., GROSSMANN, S. & LOHSE, D. 2009 Heat transfer and large scale dynamics in turbulent Rayleigh-Bénard convection. *Rev. Mod. Phys.* **81** (2), 503.

ALEMANY, A., MOREAU, R., SULEM, P. L. & FRISCH, U. 1979 Influence of an external magnetic field on homogeneous mhd turbulence. *Journal de Mécanique* **18** (2), 277–313.

AURNOU, J. M. & OLSON, P. L. 2001 Experiments on Rayleigh-Bénard convection, magnetoconvection and rotating magnetoconvection in liquid gallium. *J. Fluid Mech* **430**, 283–307.

BANDARU, V., KOLCHINSKAYA, A., PADBERG-GEHLE, K. & SCHUMACHER, J. 2015 Role of critical points of the skin friction field in formation of plumes in thermal convection. *Phys. Rev. E* **92**, 043006.

BOECK, T., KRASNOV, D., THESS, A. & ZIKANOV, O. 2008 Large-scale intermittency of liquid-metal channel flow in a magnetic field. *Phys. Rev. Lett.* **101** (24), 244501.

BRANOVER, H. 1978 *Magnetohydrodynamic flow in ducts*. John Wiley, New York.

BÜHLER, L., ARLT, T., BOECK, T., BRAIDEN, L., CHOWDHURY, V., KRASNOV, D .AND MISTRANGELO, C., MOLOKOV, S. & PRIEDE, J. 2017 Magnetically induced instabilities in duct flows. *IOP Conference Series: Materials Science and Engineering* **228** (1), 012003.

BURR, U. & MÜLLER, U. 2001 Rayleigh-Bénard convection in liquid metal layers under the influence of a vertical magnetic field. *Phys. Fluids* **13** (11), 3247–3257.

BURR, U. & MÜLLER, U. 2002 Rayleigh–Bénard convection in liquid metal layers under the influence of a horizontal magnetic field. *J. Fluid Mech.* **453**, 345–369.

BUSSE, F. H. 2008 Asymptotic theory of wall-attached convection in a horizontal fluid layer with a vertical magnetic field. *Phys. Fluids* **20** (2), 024102.

REFERENCES

BUSSE, F. H. & CLEVER, R. M. 1982 Stability of convection rolls in the presence of a vertical magnetic field. *Phys. Fluids* **25** (6), 931–935.

BUSSE, F. H. & CLEVER, R. M. 1983 Stability of convection rolls in the presence of a horizontal magnetic field. *Journal de mécanique théorique et appliquée* **2** (4), 495–502.

BUSSE, F. H. & CLEVER, R. M. 1989 Traveling-wave convection in the presence of a horizontal magnetic field. *Phys. Rev. A* **40** (4), 1954.

CHANDRASEKHAR, S. 1952 XLVI. on the inhibition of convection by a magnetic field. *The London, Edinburgh, and Dublin Philosophical Magazine and Journal of Science* **43** (340), 501–532.

CHANDRASEKHAR, S. 1961 *Hydrodynamic and Hydromagnetic Stability*. Dover.

CHILLÀ, F. & SCHUMACHER, J. 2012 New perspectives in turbulent Rayleigh-Bénard convection. *Eur. Phys. J. E* **35** (7), 58.

CIONI, S., CHAUMAT, S. & SOMMERIA, J. 2000 Effect of a vertical magnetic field on turbulent Rayleigh-Bénard convection. *Phys. Rev. E* **62** (4), R4520.

CIONI, S., CILIBERTO, S. & SOMMERIA, J. 1997 Strongly turbulent Rayleigh–Bénard convection in mercury: comparison with results at moderate prandtl number. *J. Fluid Mech.* **335**, 111–140.

CLEVER, R. M. & BUSSE, F. H. 1989 Nonlinear oscillatory convection in the presence of a vertical magnetic field. *J. Fluid Mech.* **201**, 507–523.

DAVIDSON, P. A. 2016 *Introduction to Magnetohydrodynamics*. Cambridge University Press.

DAYA, Z.A. & ECKE, R.E. 2001 Does turbulent convection feel the shape of the container? *Phys. Rev. Lett.* **87** (18), 184501.

ECKE, R. E., ZHONG, F. & KNOBLOCH, E. 1992 Hopf bifurcation with broken reflection symmetry in rotating Rayleigh-Bénard convection. *Europhys. Lett.* **19** (3), 177–182.

FAUVE, S., LAROCHE, C. & LIBCHABER, A. 1981 Effect of a horizontal magnetic field on convective instabilities in mercury. *J. de Phys. Lettres* **42** (21), 455–457.

FAUVE, S., LAROCHE, C. & LIBCHABER, A. 1984*a* Horizontal magnetic field and the oscillatory instability onset. *J. de Phys. Lettres* **45** (3), 101–105.

FAUVE, S., LAROCHE, C., LIBCHABER, A. & PERRIN, B 1984*b* Chaotic phases and magnetic order in a convective fluid. *Phys. Rev. Lett.* **52** (20), 1774.

FOROOZANI, N., NIEMELA, J. J., ARMENIO, V. & SREENIVASAN, K. R. 2017 Reorientations of the large-scale flow in turbulent convection in a cube. *Phys. Rev. E* **95** (3), 033107.

GOLDSTEIN, H. F., KNOBLOCH, E., MERCADER, I. & NET, M. 1993 Convection in a rotating cylinder. Part 1. Linear theory for moderate Prandtl numbers. *J. Fluid Mech.* **248**, 583–604.

GOLDSTEIN, H. F., KNOBLOCH, E., MERCADER, I. & NET, M. 1994 Convection in a rotating cylinder. Part 2. Linear theory for low Prandtl numbers. *J. Fluid Mech.* **262**, 293–324.

GROSSMANN, S. & LOHSE, D. 2000 Scaling in thermal convection: a unifying theory. *J. Fluid Mech.* **407**, 27–56.

GROSSMANN, S. & LOHSE, D. 2001 Thermal convection for large Prandtl numbers. *Phys. Rev. Lett.* **86** (15), 3316.

GRÖTZBACH, GÜNTHER 1983 Spatial resolution requirements for direct numerical simulation of the Rayleigh-Bénard convection. *J. Comput. Phys.* **49** (2), 241–264.

HANJALIĆ, K. & KENJEREŠ, S. 2000 Reorganization of turbulence structure in magnetic Rayleigh-Bénard convection: a T-RANS study. *J. Turbul.* **1** (1), 008.

HOATHER, W. H. 1936 The density and coefficient of expansion of liquid gallium over a wide range of temperature. *Proc. Phys. Soc.* **48** (5), 699.

HORN, S. & SCHMID, P. J. 2017 Prograde, retrograde, and oscillatory modes in rotating Rayleigh–Bénard convection. *J. Fluid Mech.* **831**, 182–211.

HOUCHENS, B. C., WITKOWSKI, L. M. & WALKER, J. S. 2002 Rayleigh-Bénard instability in a vertical cylinder with a vertical magnetic field. *J. Fluid Mech.* **469**, 189–207.

KENJEREŠ, S. & HANJALIĆ, K. 2004 Numerical simulation of magnetic control of heat transfer in thermal convection. *Int. J. Heat Fluid Flow* **25** (3), 559–568.

KING, E. M., STELLMACH, S. & AURNOU, J. M. 2012 Heat transfer by rapidly rotating Rayleigh-Bénard convection. *J. Fluid Mech.* **691**, 568–582.

KNAEPEN, B. & MOREAU, R. 2008 Magnetohydrodynamic turbulence at low magnetic Reynolds number. *Annu. Rev. Fluid Mech.* **40**, 25–45.

KNOBLOCH, E. 1998 Rotating convection: recent developments. *Int. J. Eng. Sci.* **36** (12), 1421–1450.

KRASNOV, D., BOECK, T. & BÜHLER, L. 2017 Turbulent and transitional sidewall jets in magnetohydrodynamic channels with a homogeneous magnetic field. *PAMM* **17** (1), 111–114.

KRASNOV, D., THESS, A., BOECK, T., ZHAO, Y. & ZIKANOV, O. 2013 Patterned turbulence in liquid metal flow: Computational reconstruction of the Hartmann experiment. *Phys. Rev. Lett.* **110**, 084501.

KRASNOV, D., ZIKANOV, O. & BOECK, T. 2011 Comparative study of finite difference approaches in simulation of magnetohydrodynamic turbulence at low magnetic Reynolds number. *Comput. Fluids* **50** (1), 46–59.

KRASNOV, D., ZIKANOV, O. & BOECK, T. 2012 Numerical study of magnetohydrodynamic duct flow at high reynolds and hartmann numbers. *J. Fluid Mech.* **704**, 421–446.

KUNNEN, R. P. J., CLERCX, H. J. H. & VAN HEIJST, G. J. F. 2013 The structure of sidewall boundary layers in confined rotating Rayleigh-Bénard convection. *J. Fluid Mech.* **727**, 509–532.

KUNNEN, R. P. J., STEVENS, R. J.A.M., OVERKAMP, J., SUN, C., VAN HEIJST, G. J. F. & CLERCX, H. J. H. 2011 The role of Stewartson and Ekman layers in turbulent rotating Rayleigh-Bénard convection. *J. Fluid Mech.* **688**, 422–442.

LIU, Y. & ECKE, R. E. 1999 Nonlinear travelling waves in rotating Rayleigh-Bénard convection: stability boundaries and phase diffusion. *Phys. Rev. E* **59**, 4091–4105.

LV, X. & ZIKANOV, O. 2014 Mixed convection in horizontal duct flow with transverse magnetic field and heating of side wall. *Phys. Fluids* **26** (9), 097106.

MOLOKOV, S., MOREAU, R. & MOFFATT, H. K. 2007 *Magnetohydrodynamics: Historical evolution and trends*. Springer.

MOREAU, RENÉ 1990 *Magnetohydrodynamics: Fluid Mechanics and Its Applications*. Kluwer Academic Publishers, Dordrecht.

NAKAGAWA, Y. 1955 An experiment on the inhibition of thermal convection by a magnetic field. *Nature* **175**, 417–419.

NAKAGAWA, Y 1957 Experiments on the inhibition of thermal convection by a magnetic field. *Proc. R. Soc. Lond. A* **240** (1220), 108–113.

POTHÉRAT, A. & KLEIN, R. 2017 Do magnetic fields enhance turbulence at low magnetic reynolds number? *Phys. Rev. Fluids* **2** (6), 063702.

QIU, X-L. & XIA, K-Q. 1998 Viscous boundary layers at the sidewall of a convection cell. *Phys. Rev. E* **58** (1), 486.

ROSSBY, H. T. 1969 A study of Bénard convection with and without rotation. *J. Fluid Mech.* **36** (02), 309–335.

RÜDIGER, G., KITCHATINOV, L. L. & HOLLERBACH, R. 2013 *Magnetic Processes in Astrophysics: Theory, Simulations, Experiments*. John Wiley.

SCHEEL, J. D., EMRAN, M. S. & SCHUMACHER, J. 2013 Resolving the fine-scale structure in turbulent Rayleigh–Bénard convection. *New J. Phys.* **15** (11), 113063.

SCHEEL, J. D. & SCHUMACHER, J. 2016 Global and local statistics in turbulent convection at low Prandtl numbers. *J. Fluid Mech.* **802**, 147–173.

SHERCLIFF, J. A. 1965 *A textbook of Magnetohydrodynamics*. Pergamon Press.

TAKESHITA, T., SEGAWA, T., GLAZIER, J. A. & SANO, M. 1996 Thermal turbulence in mercury. *Phys. Rev. Lett.* **76** (9), 1465.

TASAKA, Y., IGAKI, K., YANAGISAWA, T., VOGT, T., ZÜRNER, T. & ECKERT, S. 2016 Regular flow reversals in Rayleigh-Bénard convection in a horizontal magnetic field. *Phys. Rev. E* **93** (4), 043109.

THESS, A. & ZIKANOV, O. 2007 Transition from two-dimensional to three-dimensional magnetohydrodynamic turbulence. *J. Fluid Mech.* **579**, 383–412.

VASIL, G. M., BRUMMELL, N. H. & JULIEN, K. 2008 A new method for fast transforms in parity-mixed PDEs: Part II. Application to confined rotating convection. *J. Comput. Phys.* **227** (17), 8017–8034.

VOGT, T., ISHIMI, W., YANAGISAWA, T., TASAKA, Y., SAKURABA, A. & ECKERT, S. 2018 Transition between quasi-two-dimensional and three-dimensional Rayleigh-Bénard convection in a horizontal magnetic field. *Phys. Rev. Fluids* **3**, 013503.

WAGNER, S., SHISHKINA, O. & WAGNER, C. 2014 Influence of the geometry on Rayleigh-Bénard convection. *New Results in Numerical and Experimental Fluid Mechanics IX, Springer* pp. 313–321.

WEISS, N. O. & PROCTOR, M. R. E. 2014 *Magnetoconvection*. Cambridge University Press.

YANAGISAWA, T., HAMANO, Y., MIYAGOSHI, T., YAMAGISHI, Y., TASAKA, Y. & TAKEDA, Y. 2013 Convection patterns in a liquid metal under an imposed horizontal magnetic field. *Phys. Rev. E* **88** (6), 063020.

YANAGISAWA, T., HAMANO, Y. & SAKURABA, A. 2015 Flow reversals in low-Prandtl-number Rayleigh-Bénard convection controlled by horizontal circulations. *Phys. Rev. E* **92** (2), 023018.

YANAGISAWA, T., YAMAGISHI, Y., HAMANO, Y., TASAKA, Y. & TAKEDA, Y. 2011 Spontaneous flow reversals in Rayleigh-Bénard convection of a liquid metal. *Phys. Rev. E* **83** (3), 036307.

YANAGISAWA, T., YAMAGISHI, Y., HAMANO, Y., TASAKA, Y., YANO, K., TAKAHASHI, J. & TAKEDA, Y. 2010*a* Detailed investigation of thermal convection in a liquid metal under a horizontal magnetic field: Suppression of oscillatory flow observed by velocity profiles. *Phys. Rev. E* **82** (5), 056306.

YANAGISAWA, T., YAMAGISHI, Y., HAMANO, Y., TASAKA, Y., YOSHIDA, M., YANO, K. & TAKEDA, Y. 2010*b* Structure of large-scale flows and their oscillation in the thermal convection of liquid gallium. *Phys. Rev. E* **82** (1), 016320.

ZHANG, X. & ZIKANOV, O. 2014 Mixed convection in a horizontal duct with bottom heating and strong transverse magnetic field. *J. Fluid Mech.* **757**, 33–56.

ZHONG, F., ECKE, R. E. & STEINBERG, V. 1991 Asymmetric modes and transition to vortex structures in rotating Rayleigh-Bénard convection. *Phys. Rev. Lett.* **67**, 2473–2476.

ZIKANOV, O., KRASNOV, D., BOECK, T., THESS, A. & ROSSI, M. 2014*a* Laminar-turbulent transition in magnetohydrodynamic duct, pipe, and channel flows. *Appl. Mech. Rev.* **66** (3), 030802.

ZIKANOV, O., KRASNOV, D., LI, Y., BOECK, T. & THESS, A. 2014*b* Patterned turbulence in spatially evolving magnetohydrodynamic duct and pipe flows. *Theor. Comput. Fluid Dyn.* **28** (3), 319–334.

ZIKANOV, O., LISTRATOV, Y. I. & SVIRIDOV, V. G. 2013 Natural convection in horizontal pipe flow with a strong transverse magnetic field. *J. Fluid Mech.* **720**, 486–516.

ZIKANOV, O. & THESS, A. 1998 Direct numerical simulation of forced mhd turbulence at low magnetic Reynolds number. *J. Fluid Mech.* **358**, 299–333.

ZÜRNER, T., LIU, W., KRASNOV, D. & SCHUMACHER, J. 2016 Heat and momentum transfer for magnetoconvection in a vertical external magnetic field. *Phys. Rev. E* **94** (4), 043108.

Erklärung

Ich versichere, dass ich die vorliegende Arbeit ohne unzulässige Hilfe Dritter und ohne Benutzung anderer als der angegebenen Hilfsmittel angefertigt habe. Die aus anderen Quellen direkt oder indirekt übernommenen Daten und Konzepte sind unter Angabe der Quelle gekennzeichnet. Bei der Auswahl und Auswertung folgenden Materials haben mir die nachstehend aufgeführten Personen in der jeweils beschriebenen Weise unentgeltlich geholfen:

1. Die fachliche Betreuung der Arbeit erfolgte durch apl. Prof. Dr. Christian Karcher, Prof. Dr. Jörg Schumacher, Dr. Dmitry Krasnov, und Prof. Dr. André Thess.

2. Die Abbildungen 5.27, 5.29-5.32 und die Tabelle 5.2 habe ich mit Dr. Dmitry Krasnov und Prof. Jörg Schumacher bereits im Journal of Fluid Mechanics veröffentlicht. Ich führte die Berechnung durch und analysierte die Daten. Dr. Dmitry Krasnov stellte den DNS-Solver zur Verfügung und trug zur Interpretation der Ergebnisse bei. Prof. Jörg Schumacher entwarf und leitete die Arbeit und schrieb das Manuskript. Die Ergebnisse werden in dieser Dissertation mit Genehmigung des Cambridge University Press wiederverwendet.

3. Die analytischen Betrachtungen von Section 5.4 wurden von M. Sc. Till Zürner (TU Ilmenau) durchgeführt.

Weitere Personen waren an der inhaltlich-materiellen Erstellung der vorliegenden Arbeit nicht beteiligt. Insbesondere habe ich hierfür nicht die entgeltliche Hilfe von Vermittlungs bzw. Beratungsdiensten (Promotionsberater oder anderer Personen) in Anspruch genommen. Niemand hat von mir unmittelbar oder mittelbar geldwerte Leistungen für Arbeiten erhalten, die im Zusammenhang mit dem Inhalt der vorgelegten Dissertation stehen. Die Arbeit wurde bisher weder im In- noch im Ausland in gleicher oder ähnlicher Form einer Prüfungsbehörde vorgelegt. Ich bin darauf hingewiesen worden, dass die Unrichtigkeit der vorstehenden Erklärung als Täuschungsversuch bewertet wird und gemäß §7 Abs.10 der Promotionsordnung den Abbruch des Promotionsverfahrens zur Folge hat.

Ilmenau, den 06.11.2018 Wenjun Liu

Acknowledgements

This work was funded by the a Fellowship of the China Scholarship Council (CSC No. 201306080019) and by the Deutsche Forschungsgemeinschaft (DFG) within the Research Training Group Lorentz Force Velocimetry and Lorentz Force Eddy Current Testing (GRK 1567). Computer resources were provided by the computing center of TU Ilmenau and by Large Scale Project pr62se of the Gauss Centre for Supercomputing at the SuperMUC cluster at the Leibniz Rechenzentrum Garching.

I would like to thank my supervisors Prof. André Thess and Prof. Christian Karcher. Prof. Thess has initiated and then supervised my work by giving valuable advice and setting the important research directions. Prof. Karcher has taken care of me after Prof. Thess moved to DLR Stuttgart and has always been supportive. I would also like to express my deep appreciation to Prof. Jörg Schumacher who has helped, supported, and guided me to have scientific publications and to finish this thesis. I am very grateful to Dr. Dmitry Krasnov for his continued support on the numerical simulations and various interesting discussions and suggestions on MHD. I would also like to thank all colleagues from the Institute of Thermo- and Magnetohydrodymaics and the RTG Lorentz force and Lorentz force eddy current testing for their help and support throughout my work here and for the friendly working atmosphere.

Finally, I would like to thank my family and friends for their unconditional support and love. A special thanks goes to my husband, Zhenghe Luo, who supported me patiently and never complained about my moods.